# Characterization of EUV induced contamination on multilayer optics

**Juequan Chen**

**Ph.D. committee**

**Chairman:**
Prof. dr. G. van der Steenhoven       University of Twente / TNW

**Secretary:**
Prof. dr. G. van der Steenhoven       University of Twente / TNW

**Promoter:**
Prof. dr. F. Bijkerk                  University of Twente / TNW
                                      FOM Institute for Plasma Physics Rijnhuizen

**Members:**
Prof. dr. K. J. Boller               University of Twente / TNW
Prof. dr. ing. A.J.H.M. Rijnders     University of Twente / TNW
prof. dr. A. W. Kleyn                University of Amsterdam
                                     FOM Institute for Plasma Physics Rijnhuizen
Dr. ir. H. Wormeester                University of Twente / TNW

# CHARACTERIZATION OF EUV INDUCED CONTAMINATION ON MULTILAYER OPTICS

## PROEFSCHRIFT

ter verkrijging van de graad van doctor
aan de Universiteit Twente, op gezag van
de rector magnificus, prof. dr. H. Brinksma,
volgens besluit van het College voor Promoties
in het openbaar te verdedigen op
vrijdag 01 juli 2011 om 12:45 uur

door

Juequan Chen
geboren op 17 oktober 1979
te Zhejiang, China

Dit proefschrift is goedgekeurd door de promotor:

Prof. dr. F. Bijkerk

**This thesis is based on the following publications:**

**Chapter 2:** J. Chen, C. J. Lee, E. Louis, F. Bijkerk, R. Kunze, H. Schmidt, D. Schneider, and R. Moors, Characterization of EUV induced carbon films using laser-generated surface acoustic waves, Diamond and Related Materials 18 (2009) 768-771.

**Chapter 3:** J. Chen, E. Louis, C. J. Lee, H. Wormeester, R. Kunze, H. Schmidt, D. Schneider, R. Moors, W. van Schaik, M. Lubomska, and F. Bijkerk, Detection and characterization of carbon contamination on EUV multilayer mirrors, Optics Express 17 (2009) 16969-16979.

J. Chen, E. Louis, F. Bijkerk, C. J. Lee, H. Wormeester, R. Kunze, H. Schmidt, D. Schneider, R. Moors, W. van Schaik and M. Lubomska, Ellipsometric and surface acoustic wave sensing of carbon contamination on EUV optics, Proc. of SPIE Vol. 7271 (2009), 727140 1-6

**Chapter 4:** J. Chen, E. Louis, J. Verhoeven, R. Harmsen, C. J. Lee, M. Lubomska, M. van Kampen, W. van Schaik, and F. Bijkerk, Secondary electron yield measurements of carbon covered multilayer optics, Applied Surface Science 257 (2010) 354-361.

**Chapter 5:** J. Chen, E. Louis, H. Wormeester, R. Harmsen, R. van de Kruijs, C. J. Lee, W. van Schaik, F. Bijkerk, Carbon induced EUV reflectance loss characterized using visible-light ellipsometry, submitted.

**Chapter 6:** J. Chen, E. Louis, R. Harmsen, T. Tsarfati, H. Wormeester, M. van Kampen, W. van Schaik, R. van de Kruijs, F. Bijkerk, *In situ* ellipsometry study of atomic hydrogen etching of EUV-induced carbon layers, submitted.

# Contents

# 1    Introduction

## 1.1    EUV Lithography

In our daily life we live with computers, telephones and various other electronic devices. The basic blocks of modern electronic devices and computers are microchips or integrated circuits (ICs). The essential, performance-determining step in the IC manufacturing process is photolithography. Photolithography is the printing process that is applied to repetitively copy highly detailed spatial patterns (less than one micron) to a photosensitive layer (resist) on a silicon wafer [1]. After processing, the layer will form a stack of interconnected multilevel structures.

Photolithography involves a radiation source, an illumination optical system, a mask pattern that is to be replicated, a demagnifying optical system and a photoresist coated wafer to record the image of the mask pattern. The minimum line width ($L_w$) achievable with photolithography is described as [2]

$$L_w = k_1 \frac{\lambda}{NA} \tag{1}$$

where $\lambda$ is the radiation wavelength, $NA$ is the numerical aperture seen at the wafer, and $k_1$ is a constant that is largely determined by the optical system and the photo resist. Equation (1) implies that a practical solution to increase resolution is to use radiation with a shorter wavelength.

Currently the manufacturing of chips is accomplished by photolithography using deep ultraviolet (DUV) radiation at wavelengths of 248 nm and 193 nm [2-4]. One candidate technology for high volume manufacturing beyond the use of 193 nm is EUV lithography (EUVL) [1,3,5,6]. EUVL is based on the 13.5 nm wavelength in order to decrease the feature sizes, but there is a fundamental difference with 193 nm lithography: Transmittive optics, as used in DUV lithography, is not applicable for EUVL since EUV light is strongly absorbed in any material. This means that all reflective optics will have to be used. Another consequence of the high absorption of EUV radiation is that the process has to take place in vacuum and the lithography machines will be very large vacuum systems.

To achieve sufficient normal incidence reflectance of the reflective optics, multilayer mirrors (MLMs) using the principle of Bragg reflection [5] have to be used. Since the maximum reflectance of each MLM is limited to about 70% in this spectral region, the number of mirrors used in a wafer stepper is limited by overall throughput considerations. Fig. 1 shows an example of a schematic diagram of an EUVL optical system.
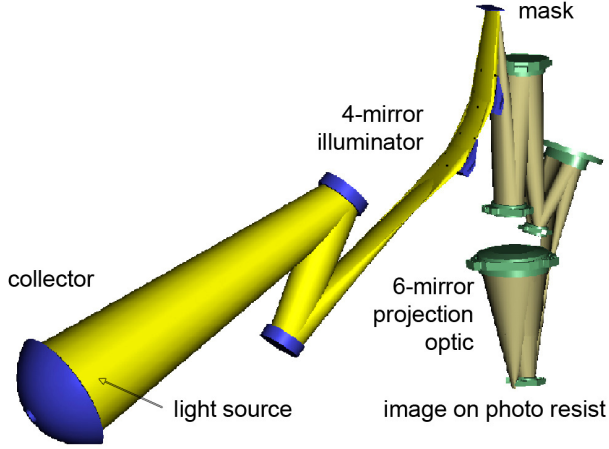
*Fig. 1. Schematic diagram of EUVL optical system*

## 1.2    Reflective multilayer mirror

The normal incidence EUV reflectance at the interface of vacuum to any material is generally less than one percent, while the transmitted radiation can still penetrate to a depth of hundreds of nanometers. Adding more interfaces such that the reflected radiation from all interfaces adds in phase (i.e. constructive interference) will increase the overall reflectance. Thus, a multilayer structure, as shown schematically in Fig. 2, is applied in order to increase the EUV reflectance. It is formed by depositing alternating layers of two materials with different refractive index. Typically the two materials are of alternating high and low atomic number in order to maximize the difference in electron density and the resulting optical contrast.

In order to achieve constructive interference for a certain wavelength $\lambda$ with a certain incidence angle to the surface $\theta$, the period thickness $d$ (one layer pair) has to be designed to meet the Bragg's law [5]

$$m\lambda = 2d \sin\theta \sqrt{1 - \frac{2\overline{\delta}}{\sin^2\theta}}, \overline{\delta} << 1, \overline{\beta} << \overline{\delta} \tag{2}$$

where $m$ is the order of the Bragg maximum, $\overline{\delta}$ is the weighted average over one period of the deviation of the real part of the refractive index from unity. The complex refractive index is defined as

$$n = 1 - \delta + i\beta \tag{3}$$

where $\beta$ is the imaginary part of the refractive index, also called extinction coefficient.

A reflectance at normal incidence of approximately 70% has been achieved in the EUV wavelength range using the material combination of Mo and Si, for a photon energy just below the $L_{2-3}$ absorption edges of silicon (99 eV) [2,7-10]. Fig. 2 shows a

Mo/Si multilayer system, designed for 13.5 nm (92 eV) EUV radiation. Si acts as a 'spacer' since both $\delta$ and $\beta$ are very small ($5.4 \times 10^{-4}$ and $1.8 \times 10^{-3}$ at $\lambda = 13.5$ nm, respectively). On the other hand, Mo acts as a 'reflector' with a rather low $\beta$ ($6.4 \times 10^{-3}$ at $\lambda = 13.5$ nm), but with a relatively high $\delta$ ($7.8 \times 10^{-2}$ at $\lambda = 13.5$ nm). Thus, the combination of Mo/Si provides high optical contrast and minimum absorption.

Fig. 3 shows a measured reflectance versus wavelength for a Mo/Si multilayer mirror consisting of 50 periods with $\Gamma = 0.4$ [9]. $\Gamma$ is the ratio of high $Z$ material thickness to the period thickness ($d$) defined as

$$\Gamma = \frac{t_{Mo}}{d} \tag{4}$$

where $t_{Mo}$ is the thickness of Mo. The maximum reflectance in the figure is about 69.5% centered at a wavelength of 13.5 nm.



Fig. 2. Alternating layers of silicon and molybdenum in a multilayer structure



Fig. 3. Measured reflectance versus wavelength for a Mo/Si multilayer mirror consisting of 50 periods [9]

## 1.3    Contamination and cleaning of EUV optics

EUV optics are used in vacuum conditions to minimize absorption of EUV light by air. The main chamber is filled with optics, sensors, reticles, electric wiring and numerous other components [11]. All these components not only produce outgassing but also make 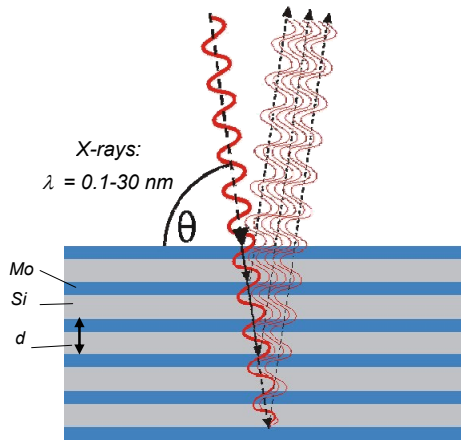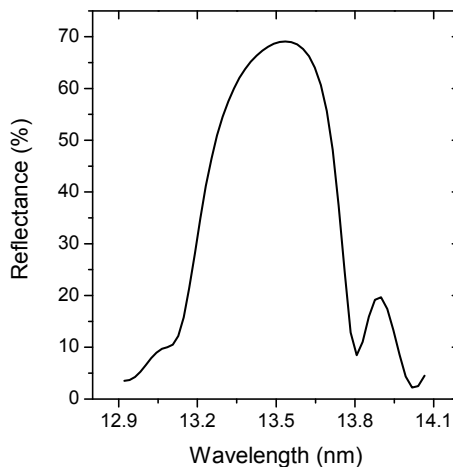baking of the vacuum system impossible. Therefore, the lithography process is conducted under conditions far from ultrahigh vacuum (UHV). The residual gas mixture consists of many different components including hydrogen, oxygen, water and hydrocarbons. Moreover, the contribution of hydrocarbons produced during the exposure process itself can not be ignored. The photochemistry of the relevant processes at the surface of the multilayer optics is found to be largely dependent on the type and pressure of background gas constituents and the incident flux of the EUV photons. Under illumination of EUV radiation, photoelectrons of less than 10 eV are typically created [12]. Cracking of adsorbed molecules at the optical surface by those photoelectrons or by EUV photo dissociation directly results in contamination of the surface with molecules and radicals [13-15].

        Water and oxygen act as oxidizers, which will etch away surfaces such as silicon. This effect can be prevented or mitigated by using an oxidation resistant protective capping layer. Hydrocarbons lead to carbon growth as illustrated in Fig. 4. There are three steps leading to carbon growth: adsorption, diffusion and photon or secondary electron induced dissociation [12,13]. Unfortunately, the capping layer does not prevent the build up of carbon contamination, leaving this as the main surface contamination process [12]. Even under relatively good vacuum conditions, carbon contamination has been observed, as evidenced by examination of synchrotron beam line optics [13,14].

        The high absorption of EUV radiation by carbon makes the contamination layer a serious loss source for optical throughput. For instance, IMD modeling [16] shows that a layer of only 2 nanometer of pure graphite (density 2.25 $g/cm^3$) leads to a 5% reduction in relative reflectivity from a single multilayer optical surface. If such a layer were to form on every reflecting surface, it would consume the full lifetime budget of EUVL optics: The end of life of the optical system is reached if each optic has an irreversible relative reflection loss of 1% and this should not happen within 30000 hours [15]. This implies that strategies have to be developed to clean the optics in the lithography machines which requires an easy to implement and use technique to monitor the contamination state of the optics on the one hand and follow the cleaning process on the other hand. Therefore, the focus of this thesis is on monitoring the build up as well as the removal of carbon contamination.

        Long maintenance shutdowns of the lithography equipment are undesirable, making it necessary to detect and characterize contaminants before significant loss of throughput of the optical system is observed, enabling timely cleaning of the mirror surfaces without opening the vacuum chamber. Therefore, a successful monitoring of the contamination process should have a low detection limit, a high sensitivity, a high

accuracy and it should be rapid. Furthermore it should have the potential to disclose the nature of the contamination, it should be vacuum compatible, easy to handle, affordable and it should require little space in the lithography equipment. Several candidate techniques that have been considered for contamination monitoring will be reviewed in the next section.

Various methods have been suggested for removal of the carbon contamination including atomic hydrogen (H[0]) cleaning [17-20], molecular oxygen with EUV radiation [21,22], ozone cleaning [23], and radio frequency discharge cleaning using oxygen or hydrogen plasma [24]. Among these methods, atomic hydrogen cleaning is considered to be most attractive since it can volatilize carbon as illustrated in Fig. 5. The mechanism of chemical erosion due to thermal hydrogen atoms has been reviewed in literature [25]. In addition, this approach reduces or eliminates the risks of oxidation of the optics compared to cleaning with ions.
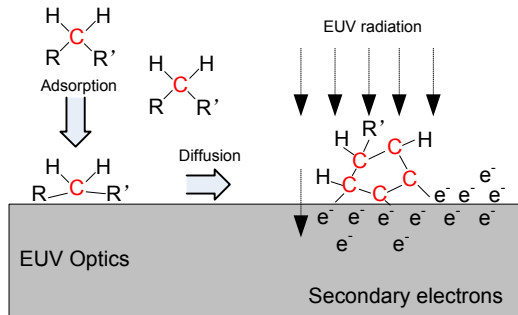


*Fig. 4. Physical mechanism of carbon contamination on EUV optics under EUV radiation*
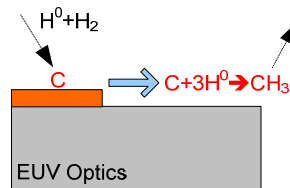


*Fig. 5. Atomic hydrogen cleaning upon multilayer optics*

## 1.4    *Surface analysis techniques for contamination monitoring*

Worldwide, several techniques have been used to *ex situ* investigate EUV optics or reticle contamination. X-ray photoelectron spectroscopy (XPS) and Auger electron spectroscopy (AES) [21,26-29], Auger depth profiling analysis [12,22,30], and extreme

ultraviolet photoelectron spectroscopy (EUPS) [31] have been employed to measure the thickness or concentration of EUV induced carbon contamination films. However, most of these techniques lack sub-nanometer limits of detection, but the most important restriction is that all these techniques require a considerably better vacuum than is available in the lithography equipment. In addition, all of these techniques require substantial amounts of space within the vacuum chamber, making them less- or even un-suitable for *in situ* monitoring because of the very compact design of the EUVL equipment.

At the start of this PhD research, we have made an inventory of candidate techniques that have been suggested for *in situ* optics contamination monitoring [32]. The most important ones are listed here. These techniques are introduced in the following sections.

1) EUV induced photocurrent
2) Spectroscopic Ellipsometry
3) Disappearance potential spectroscopy (DAPS)
4) X-ray fluorescence (XRF)
5) Laser-generated surface acoustic waves (LG-SAWs)
6) Secondary electron yield (SEY)


## 1.4.1   EUV induced photocurrent

Photoelectrons are generated under EUV photon radiation in any material, with a photo-conversion efficiency (*k*) that depends on material and strength of the electric field. The EUV induced photocurrent *(I)* can be described as

$$I_{photocurrent} = \int_0^\infty k(Z, E(\lambda, x)) f(x) dx \qquad (5)$$

where $Z$ is the atomic number, $E$ is the electric field which is a function of the wavelength $\lambda$ and depth $x$. The function $f(x)$ is the probability that a photoelectron, produced at depth $x$, arrives at and escapes from the surface. This is influenced by the typical energy of these electrons and the top surface material work function. The photocurrent can be measured by applying electrical contacts to the surface.

When EUV radiation is incident on a multilayer, the combination of incident and reflected radiation fields generate a sinusoidal standing wave electric field both inside and outside the multilayer structure [23,33]. Fig. 6 shows the electric field intensity as a function of depth for a multilayer structure for normal incidence. The period of the standing wave is approximately half of the wavelength of the incident EUV light. Nodes and anti-nodes in the electric field result in minima and maxima for the efficiency of creating photoelectrons. For incident photon energies of 92 eV, characteristic for EUV lithography applications, photoelectrons of less than 10 eV are typically created [34], resulting in electron mean free paths of the order of 3-5 nm in

metals [35]. Thus, only photoelectrons created close to the surface can escape from the multilayer and contribute to the photocurrent. The X-ray standing wave is determined by the multilayer structure and the phase at the surface strongly depends on the position of the surface. A change of the position of the surface of the multilayer structure (e.g. by carbon contamination or oxidation) therefore changes the amplitude of the X-ray standing wave induced electric field and thus the yield of the photo electrons. This, together with the change of the conversion efficiency due to the change in top surface composition results in a change in the photocurrent [33].

Photocurrent measurement has been considered as a technique for contamination monitoring. Main advantage of photocurrent measurement is a high sensitivity to changes in contamination level. Also, the technique is implemented "for free", i.e. no extra probe beams are necessary. A major disadvantage however is that the wavelength dependence of the photocurrent is required to confirm the displacement of the surface due to carbon or other contamination. Since the light in EUVL equipments is not sufficiently monochromatic and since it is impossible to scan, the photocurrent wavelength dependence cannot be determined. Additional disadvantages are the absence of lateral resolution, uncertainty in modeling the standing wave and conversion efficiencies near the surface, as shown in equation (5). In addition, the photocurrent measurement lacks direct chemical information and only indicates an average signal for a non-uniform contamination layer. Therefore this technique was not selected for further investigation within the scope of this thesis.
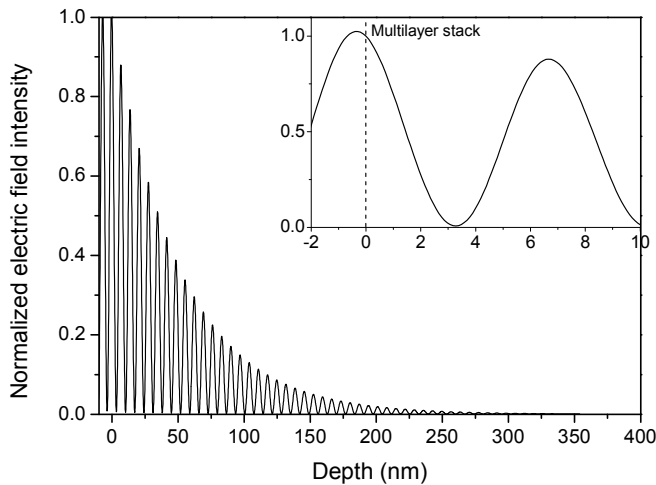


*Fig. 6. Electric field intensity as a function of depth in a multilayer structure*

## 1.4.2    Ellipsometry

Ellipsometry is a non-contact, non-destructive and very sensitive technique that uses polarized light to characterize thin films, surfaces, and material microstructure [36]. It measures the polarization status change of linearly polarized light after reflection from a surface. The measured values are expressed as $\psi$ and $\Delta$. These values are related to the ratio $\rho$ of Fresnel reflection coefficients $R_p$ and $R_s$ for $p$ and $s$ components, respectively.

$$\rho \equiv \frac{R_p}{R_s} = \frac{E_{rp}/E_{ip}}{E_{rs}/E_{is}} = \frac{\left|E_{rp}\right|\exp(i\Delta_p)\left|E_{is}\right|\exp(i\Delta_l)}{\left|E_{rs}\right|\exp(i\Delta_s)\left|E_{ip}\right|\exp(i\Delta_l)}$$

$$= \frac{\left|E_{rp}\right|\left|E_{is}\right|\exp(i\Delta_p)}{\left|E_{rs}\right|\left|E_{ip}\right|\exp(i\Delta_s)} = \tan\Psi\exp(i\Delta) \tag{6}$$

where $\tan\Psi \equiv \dfrac{\left|E_{rp}\right|\left|E_{is}\right|}{\left|E_{rs}\right|\left|E_{ip}\right|}$ which is related to the ratio of the electric field amplitudes,

and $\Delta = \Delta_p - \Delta_s$ which is the phase difference between the $p$ and $s$ component after reflection from the sample. $\Delta_l$ is the phase for both the $p$ and $s$ component of the incident linearly polarized light.

A number of different configurations exist for ellipsometry. We will explain the ellipsometry measurement based on the Rotating Analyzer Ellipsometer (RAE) configuration since RAE is the basis of rotating element ellipsometers. The typical configuration of the RAE is shown in Fig. 7 which contains a source, polarizer, sample, continuously rotating analyzer and detector. The polarizer is to linearly polarize the beam incident on the sample. The combination of rotating analyzer and detector provides the information of the polarization state of the reflected beam.

The measured ellipsometric angles, $\psi$ and $\Delta$, do not directly yield the quantities of interest, such as optical constants and film thickness. Rather, they are functions of these parameters that can be obtained by fitting an optical model to the measured $\psi$ and $\Delta$. As discussed in chapter 3, this can even be done in very complex multilayer stacks that have a period of several nanometers [37]. Ellipsometry also has the advantage that, by measuring changes of the polarization, the instrument is largely immune to the intensity noise of the light source, in contrast to reflectivity measurements. In addition, *in situ* SE has already been developed and applied in some areas of deposition monitoring and active process control [38,39]. The light source, analyzer and other components can remain outside of the vacuum, meaning that only line-of-sight optical access to the surface under study is required. Furthermore, *in situ*

ellipsometry has been shown to possess monolayer resolution during deposition processes [40].

Ellipsometry requires a well defined parallel incident and reflected beam. Due to a mirror substrate curvature the reflected beam will not be the parallel beam anymore which complicates ellipsometry measurements. This can be compensated with lenses, but that will increase the calibration complexity.
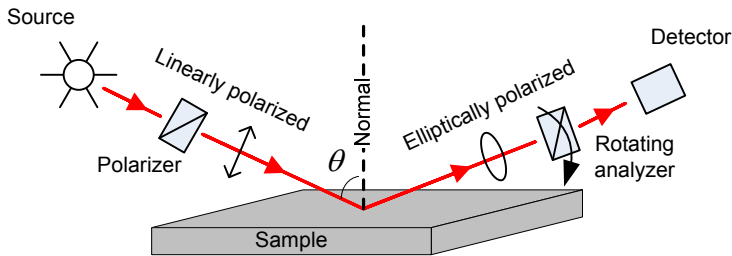


Fig. 7. Typical configuration of rotating analyzer ellipsometer

As illustrated in Fig. 7, *in situ* ellipsometry needs line-of-sight access to the sample surface. This might not be available for every mirror in the EUVL equipment. However, we could use polarization preserving (PM) fibers to deliver light to and from the sample. Fig. 8 shows an example of the fiber-based ellipsometry setup. Monitoring the polarization exiting the fiber is important since the polarization variation due to the fiber varies with temperature or stress in the fiber. We determined the polarization state of the light exiting the PM fiber by measuring the polarization state of the light reflected from the end facet of the fiber.

Besides the inherent sensitivity of ellipsometry, the extra advantage of fiber-based ellipsometry is the flexibility of using guided optics. The concept illustrated in Fig. 8 has been verified experimentally for carbon deposited EUV optics. Further investigations, especially data analysis, will have to be carried out. The work on fiber based ellipsometry is carried out by master student Feng Liu under guidance of Dr. Chris Lee at the University of Twente.
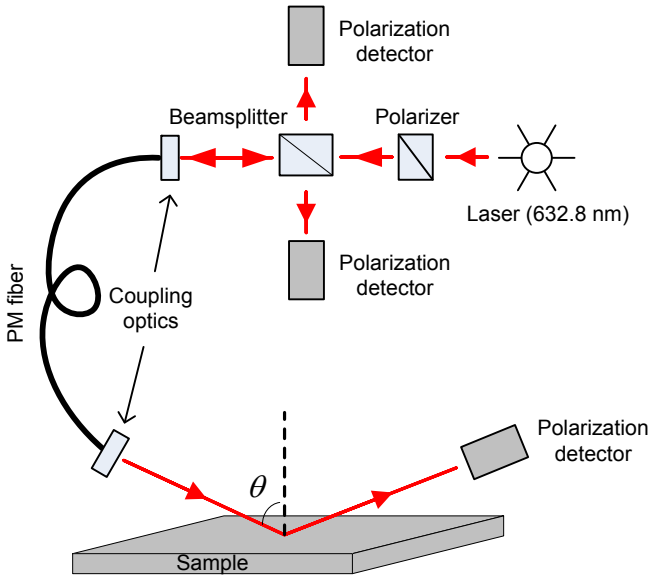
*Fig. 8. Fiber-based ellipsometry setup*

### 1.4.3    **Disappearance potential spectroscopy (DAPS)**

When a surface is bombarded by electrons, core holes are created when the electron energy is above an absorption edge of the target. This results in a reduction of elastically reflected electrons, often referred to as disappearance of those electrons. Therefore the analysis technique based on this phenomenon is named disappearance potential spectroscopy (DAPS) [41,42].

A typical DAPS system consists of an electron gun and/or a potential grid for accelerating incident electrons, a sample holder and a retarding field analyzer (RFA) as illustrated in Fig. 9. The incident electron energy is scanned within a chosen energy window. The retarding field is simultaneously scanned with a potential some eV lower than the primary energy, so that only elastically reflected electrons can pass. The electron current at the collector of the RFA versus the primary electron energy is measured and analyzed. An example of detecting vanadium by DAPS can be found in reference [42].

In X-ray photoelectron spectroscopy (XPS), electrons characteristic for an inner shell excitation only have to travel out of the solid without energy loss. However, elastically reflected electrons not only penetrate to a certain depth without energy loss, but also maintain their energy on their way back. Thus, these electrons cover twice the distance ($2x$) of an 'XPS-electron' and could have undergone energy loss with a probability that is $\exp(x/\lambda)$ times larger. This reveals that DAPS basically has higher

surface sensitivity compared to other types of electron spectroscopy if a similar geometry is applied. It can be expected that the first three atomic layers dominate the DAPS signal. Besides high surface sensitivity, another advantage of DAPS is that it is element specific. However, the high surface sensitivity is also a principle disadvantage since it prohibits detecting information about the thickness of the contamination layer. A technical disadvantage is the large volume a RFA occupies which is not always available in an EUVL equipment. Nevertheless, it should be possible to monitor the DAPS process from determining small changes of the sample current since the 'disappeared' elastically reflected electron will appear in the sample. However, the pilot experiments that we carried out show that the detected signal is very noisy and sensitive to charging of components in the vacuum. Therefore this technique was not selected for further investigation.
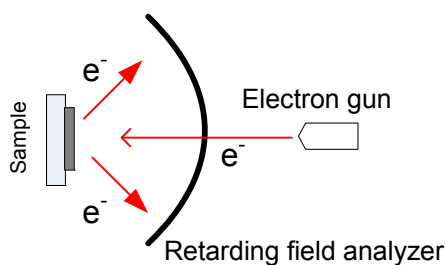


*Fig. 9. Schematic configuration of disappearance potential spectroscopy*

### 1.4.4    X-ray Fluorescence

X-ray fluorescence (XRF) is the emission of characteristic X-rays from a material that has been excited by high energy X-ray photons. The phenomenon is widely used for elemental as well as chemical analysis. However, for low $Z$ elements, such as C and O which are important for optics contamination, XRF is a challenging task. It should be emphasized that the energy of the emitted fluorescence radiation is very low so that any absorption effects have to be taken into consideration and the entire system should be in vacuum.

To reduce the background caused by scattering, total reflection X-ray fluorescence (TXRF) has been used for low $Z$ element analysis [43-47] since TXRF yields a higher signal than XRF because the reflected beam also contributes to sample excitation. Fig. 10 shows a schematic diagram of the TXRF measurement setup. The total reflection geometry also has the possibility to place the detector very close to the sample to maximize the collection of the fluorescent radiation.

An energy filter is inserted to suppress the high energy photons which can reduce the low energy background on the fluorescence spectra. This energy filter can be a high energy cut off filter or a multilayer monochromator [45].

The intensity of the fluorescence radiation (e.g. $K_\alpha$) is determined by the following factors [46]: the intensity of the probe beam, the geometric factor, the photoelectric mass absorption coefficient of the $K$ shell, the fluorescence yield, the efficiency of the detector, the concentration of the element in the sample and the absorption of the fluorescent radiation in the material

In our case, we are interested in detecting carbon which means that the fluorescence yield is fixed as tabulated in reference [48]. To improve the detection limit, we should increase the probe beam intensity. In addition, the photoelectric mass absorption coefficient of the $K$ shell is larger if the energy difference between the exciting radiation and the absorption edge is small [47]. Thus, a BN-anode X-ray tube emitting N-$K_\alpha$ radiation with a photon energy of 392 eV would be a suitable option to generate C-$K_\alpha$ radiation (277 eV) for carbon detection. To increase the detector efficiency, a solid state detector, e.g. Si (Li) detector or silicon drift detector was used for low $Z$ elements analysis in the literature [49].

The main advantage of TXRF is that the technique is element specific and quantitative, but we estimated the intensity of the TXRF response of a thin carbon layer and concluded that it will be very difficult, if not impossible to achieve sub-nanometer sensitivity. Another principle disadvantage is the lack of the thickness information of the contamination layer if it is thicker than the escape depth of the fluorescence radiation. Furthermore, the system is very complex, requires a substantial volume in the vacuum and the detector has to be mounted as close as possible to the sample surface, which is very difficult to fulfill because of the optical train used in an EUVL equipment. For all these reasons this technique was not selected for further investigation.
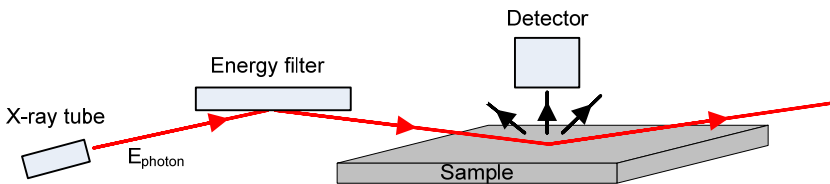


*Fig. 10. Schematic diagram of total reflection X-ray fluorescence measurement*

## 1.4.5   Laser-generated surface acoustic waves (LG-SAWs)

A thin film deposited on a bulk material influences the wave velocity of a surface acoustic wave, which can therefore be used to determine the existence of such a layer on bulk material. For homogeneous isotropic materials the propagation velocity $C$ of the surface waves is determined by Young's modulus $E$, Poisson's ratio $\nu$, and density $\rho$ as follows [50]:

$$C = \frac{0.87 + 1.12\nu}{1+\nu} \sqrt{\frac{E}{2\rho(1+\nu)}} \tag{7}$$

For bulk materials the velocity is not dependent on the frequency.

The amplitude of the surface wave is largest at the surface and decreases exponentially with depth. The penetration depth of the wave is proportional to the wavelength and decreases with increasing frequency. This means that surface waves with higher frequencies are more influenced by the film. Therefore, the surface wave velocity of a thin film does depend on the frequency, a phenomenon known as dispersion. Measuring velocity versus frequency can provide useful information of thin film and substrate.

The surface wave can be generated by a pulsed laser and detected with a piezoelectric transducer. Fourier transformation of the acoustic signal provides the dispersion curve (i.e. velocity versus frequency) with a bandwidth up to 200 MHz.

Fitting the dispersion relation to the measured curve reveals the film properties such as Young's modulus, Poisson's ratio, density and thickness of the film. The amount of parameters that can be determined from the fitting depends on the combination of film and substrate, and the film thickness.

The main advantage of LG-SAW is that it can distinguish different phases of carbon accurately. However, it is currently a contact technique that cannot be used for projection optics since contact can induce figure disturbing stress phenomena in the optic, thus limiting the use to illuminator optics only. Furthermore, the substrate has to be crystalline to have a low absorption of the high frequency SAW. In addition, the limit of detection is more than one nanometer. It should also be noted that the piezoelectric detector used will not work properly at temperatures higher than 100° C. More details of advantages and disadvantages of this candidate can be found in chapter 2 and 3.
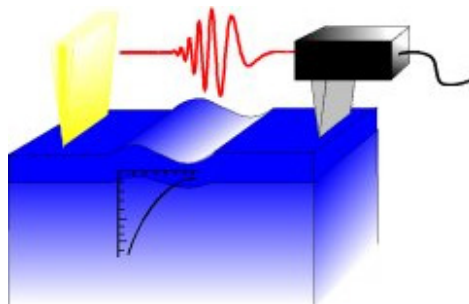


*Fig. 11. Schematic diagram of LG-SAW measurement including a focused laser beam (left side) and a piezoelectric transducer (right side)*

### 1.4.6    Secondary electron yield

Secondary electron (SE) emission is the phenomenon that low energy electrons escape from a solid surface under bombardment with high energy primary electrons, ions, or photons. When a primary electron impinges on a surface, it can either reflect elastically or inelastically. According to the energy loss process, the interactions between the primary electron and the material are mainly ionization, phonon and plasmon excitations, interband transitions, and free electron scattering. The electrons generated by these inelastic scattering processes are referred to as "true" secondary electrons. The yield of these 'true' secondary electrons (SEY) is defined as the number of secondary electrons per incident primary electron.

Most secondary electrons have a very low kinetic energy of less than 50 eV and the peak of the energy distribution spectrum is located between 2 and 5 eV. Due to their low energy, the SE escape depth is typically in the order of 3-5 nm in metals. For a carbon film, the escape depth of SE is estimated to be about 3 nm [51]. This makes SEY a good candidate for detecting the formation of thin films.

The main advantage of the SEY measurement is the low detection limit of less than 0.1 nm which is sufficient for monitoring optics contamination. The disadvantage is the lack of the thickness information of the contamination layer if it is thicker than the escape depth of the secondary electrons. Also, the electron beam can induce outgasing which can cause molecular contamination. More details of SEY and data analysis can be found in chapter 4.

After literature studies and pilot experiments a selection of the three most promising techniques for further investigation was made. These are spectroscopic ellipsometry, laser-generated surface acoustic waves and secondary electron yield. Their results of that investigation will be discussed in this thesis.

### 1.5    *The contribution of this thesis*

Contamination is a critical concern in the field of EUVL because it causes a decrease of the EUV reflectance of Mo/Si multilayer mirrors and therefore a loss of throughput of EUVL optical systems. Before this PhD research, there were already some efforts on-going to monitor the contamination. For example, during the Sematech 'Optics Lifetime & Contamination Workshop' in 2005 [32] the potential requirements of EUVL equipment suppliers were discussed and experts in the field suggested a list of options for *in situ* monitoring including various optical techniques (e.g. spectroscopic ellipsometry, reflectometry, and infrared spectroscopy), fluorescence measurements and scattered EUV light measurements. However, for all these techniques very limited experimental data on either carbon contamination or oxidation of EUV optics is available. In addition, to our knowledge, the EUV induced carbon contamination properties have not been investigated in detail.

The main part of the research in this thesis is exploring these and new approaches for monitoring contamination on EUV optics. We started from an inventory of the possible candidates as listed in section 1.4. Literature investigations and/or pilot experiments were carried out for each candidate to verify their suitability for monitoring optics contamination. After that, the three most promising techniques, laser-generated surface acoustic waves (LG-SAWs), spectroscopic ellipsometry and secondary electron yield (SEY) measurement were investigated in detail. The test results are reported in chapter 3 and 4.

All three methods investigated have the potential to be used as *in situ* contamination monitoring techniques:

- We demonstrated that LG-SAW measurements allow both detecting the layer thickness and investigating the mechanical properties of the contamination layer by analysis of carbon films that were grown on a multilayer under EUV illumination. It was inferred from the low Young's modulus (< 100 GPa) that such an EUV induced carbon layer is mechanically soft and polymeric in nature with a high percentage of hydrogen. This is of high relevance to the question if the contamination layer can be removed by cleaning easily.

- By applying SEY measurements *in situ* on deposited carbon we demonstrated a detection limit of less than 0.1 nm and showed the reversal of the SEY signal when the carbon was removed by cleaning.

- After comparing these two techniques to ellipsometry, our conclusion is that spectroscopic ellipsometry is by far the best technique for contamination monitoring. A functional model was built using spectroscopic ellipsometry, enabling us to show that spectroscopic ellipsometry can not only determine the thickness of the contamination layer, but, maybe even more important, discriminate, based on the optical properties, between the different phases of carbon.

Additionally, we developed a model based on the Bruggeman's effective medium approximation, that enables the prediction of EUV reflectance loss from visible light properties of the contamination layer. The validity of this prediction was experimentally verified. Applying spectroscopic ellipsometry during removal of the carbon layer by atomic hydrogen cleaning enabled not only end point detection, but also determination of the cleaning rate.

Therefore, we recommend the use of spectroscopic ellipsometry for *in situ* monitoring of EUVL optic contamination.

## 1.6   References

[1]   *EUV Lithography*; *Vol. PM178*, edited by V. Bakshi (SPIE, 2008).

[2]   D. Attwood, Soft X-Rays and Extreme Ultraviolet Radiation: Principles and Applications, 1999.

[3]   B. Fay, Advanced optical lithography development, from UV to EUV, Microelectronic Engineering 61-62 (2002) 11-24.

[4]   K. Ronse, Optical lithography--a historical perspective, Comptes Rendus Physique
       7 (2006) 844-857.

[5]   E. Spiller, Soft X-Ray Optics, SPIE, 1994.

[6]   J. Benschop, V. Banine, S. Lok, and E. Loopstra, Extreme ultraviolet lithography:
       Status and prospects, Journal of Vacuum Science & Technology B 26 (2008)
       2204-2207.

[7]   A. E. Yakshin, R. W. E. v. d. Kruijs, I. Nedelcu, E. Zoethout, E. Louis, F. Bijkerk,
       H. Enkisch, and S. Mullender, Enhanced reflectance of interface engineered Mo/Si
       multilayers produced by thermal particle deposition, 2007 (SPIE), 6517, p. 65170I.

[8]   D. G. Stearns, R. S. Rosen, and S. P. Vernon, Fabrication of high-reflectance Mo--
       Si multilayer mirrors by planar-magnetron sputtering, Journal of Vacuum Science
       & Technology A: Vacuum, Surfaces, and Films 9 (1991) 2662-2669.

[9]   E. Zoethout, G. Sipos, R. W. van de Kruijs, A. E. Yakshin, E. Louis, S.
       Muellender, and F. Bijkerk, Stress mitigation in Mo/Si multilayers for EUV
       lithography, 2003 (SPIE), 5037, p. 872-878.

[10]  E. Louis, A. E. Yakshin, P. C. Goerts, S. Oestreich, R. Stuik, E. L. G. Maas, M. J.
       H. Kessels, F. Bijkerk, M. Haidl, S. Muellender, M. Mertin, D. Schmitz, F.
       Scholze, and G. Ulm, Progress in Mo/Si multilayer coating technology for EUVL
       optics, 2000 (SPIE), 3997, p. 406-411.

[11]  H. Meiling, H. Meijer, V. Banine, R. Moors, R. Groeneveld, H.-J. Voorma, U.
       Mickan, B. Wolschrijn, B. Mertens, G. van Baars, P. Kurz, and N. Harned, First
       performance results of the ASML alpha demo tool, 2006 (SPIE), 6151, p. 615108.

[12]  J. Hollenshead and L. Klebanoff, Modeling radiation-induced carbon
       contamination of extreme ultraviolet optics, Journal of Vacuum Science &
       Technology B 24 (2006) 64-82.

[13]  K.-J. Boller, R.-P. Haelbich, H. Hogrefe, W. Jark, and C. Kunz, Investigation of
       carbon contamination of mirror surfaces exposed to synchrotron radiation, Nuclear
       Instruments and Methods in Physics Research 208 (1983) 273-279.

[14]  T. Naito, M. Tadano, N. Terunuma, J. Urakawa, E. Nakamura, M. Hasumoto, H.
       Sakai, T. Shibuya, F. Sakai, H. Ohgaki, and N. Sei, Investigation of carbon
       contamination on SR-irradiated devices, Nuclear Instruments & Methods in
       Physics Research Section a-Accelerators Spectrometers Detectors and Associated
       Equipment 527 (2004) 624-631.

[15]  B. Mertens, M. Weiss, H. Meiling, R. Klein, E. Louis, R. Kurt, M. Wedowski, H.
       Trenkler, B. Wolschrijn, R. Jansen, A. van de Runstraat, R. Moors, K. Spee, S.
       Ploger, and R. van de Kruijs, Progress in EUV optics lifetime expectations,
       Microelectronic Engineering 73-74 (2004) 16-22.

[16]  D. L. Windt, IMD - Software for modeling the optical properties of multilayer
       films, Computers in Physics 12 (1998) 360-370.

[17] K. Motai, H. Oizumi, S. Miyagaki, I. Nishiyama, A. Izumi, T. Ueno, and A. Namiki, Cleaning technology for EUV multilayer mirror using atomic hydrogen generated with hot wire, Thin Solid Films 516 (2008) 839-843.

[18] H. Oizumi, A. Izumi, K. Motai, I. Nishiyama, and A. Namiki, Atomic hydrogen cleaning of surface Ru oxide formed by extreme ultraviolet irradiation of Ru-capped multilayer mirrors in H2O ambience, Japanese Journal of Applied Physics Part 2-Letters & Express Letters 46 (2007) L633-L635.

[19] S. Graham, C. Steinhaus, M. Clift, L. Klebanoff, and S. Bajt, Atomic hydrogen cleaning of EUV multilayer optics, 2003 (SPIE), 5037, p. 460-469.

[20] D. J. W. Klunder, M. M. J. W. v. Herpen, V. Y. Banine, and K. Gielissen, Debris mitigation and cleaning strategies for Sn-based sources for EUV lithography, 2005 (SPIE), 5751, p. 943-951.

[21] B. Mertens, B. Wolschrijn, R. Jansen, N. B. Koster, M. Weiss, M. Wedowski, R. M. Klein, T. Bock, and R. Thornagel, EUV time-resolved studies on carbon growth and cleaning, 2003 (SPIE), 5037, p. 95-102.

[22] M. E. Malinowski, P. A. Grunow, C. Steinhaus, W. M. Clift, and L. E. Klebanoff, Use of molecular oxygen to reduce EUV-induced carbon contamination of optics, 2001 (SPIE), 4343, p. 347-356.

[23] S. Oestreich, R. Klein, F. Scholze, J. Jonkers, E. Louis, A. E. Yakshin, P. C. Goerts, G. Ulm, M. Haidl, and F. Bijkerk, Multilayer reflectance during exposure to EUV radiation, 2000 (SPIE), 4146, p. 64-71.

[24] S. Graham, C. Steinhaus, M. Clift, and L. Klebanoff, Radio-frequency discharge cleaning of silicon-capped Mo/Si multilayer extreme ultraviolet optics, Journal of Vacuum Science & Technology B: Microelectronics and Nanometer Structures 20 (2002) 2393-2400.

[25] U. Samm, Physical processes of the interaction of fusion plasmas with solids, Plasma Physics and Controlled Fusion 38 (1996)

[26] U. Okoroanyanwu, A. Jiang, K. Dittmar, T. Fahr, T. Laursen, O. Wood, K. Cummings, C. Holfeld, J.-H. Peters, E. Gullikson, and B. L. Fontaine, Monitoring reticle molecular contamination in ASML EUV Alpha Demo Tool, 2010 (SPIE), 7636, p. 76360H.

[27] S. Matsunari, T. Aoki, K. Murakami, Y. Gomei, S. Terashima, H. Takase, M. Tanabe, Y. Watanabe, Y. Kakutani, M. Niibe, and Y. Fukuda, Carbon deposition on multi-layer mirrors by extreme ultra violet ray irradiation, SPIE, San Jose, CA, USA, 2007 (SPIE), 6517, p. 65172X-8.

[28] G. Kyriakou, D. J. Davis, R. B. Grant, D. J. Watson, A. Keen, M. S. Tikhov, and R. M. Lambert, Electron impact-assisted carbon film growth on Ru(0001): Implications for next-generation EUV lithography, Journal of Physical Chemistry C 111 (2007) 4491-4494.

[29] U. Okoroanyanwu, K. Dittmar, T. Fahr, T. Wallow, B. L. Fontaine, O. Wood, C. Holfeld, K. Bubke, and J.-H. Peters, Analysis and characterization of contamination in EUV reticles, 2010 (SPIE), 7636, p. 76361Y.

[30] N. Koster, B. Mertens, R. Jansen, A. van de Runstraat, F. Stietz, M. Wedowski, H. Meiling, R. Klein, A. Gottwald, F. Scholze, M. Visser, R. Kurt, P. Zalm, E. Louis, and A. Yakshin, Molecular contamination mitigation in EUVL by environmental control, Microelectronic Engineering 61-2 (2002) 65-76.

[31] D. H. Lee, T. Tomie, D. Jessie, and Y. M. Sung, Detection of Atomic-Level Surface Contamination by Extreme Ultraviolet Photoelectron Spectroscopy Technology, IEEE Transactions on Plasma Science 37 (2009) 1490-1494.

[32] http://www.sematech.org/meetings/archives/litho/7741/index.htm

[33] M. E. Malinowski, C. Steinhaus, W. M. Clift, L. E. Klebanoff, S. Mrowka, and R. Soufli, Controlling contamination in Mo/Si multilayer mirrors by Si surface capping modifications, 2002 (SPIE), 4688, p. 442-453.

[34] T. E. Madey, N. S. Faradzhev, B. V. Yakshinskiy, and N. V. Edwards, Surface phenomena related to mirror degradation in extreme ultraviolet (EUV) lithography, Applied Surface Science 253 (2006) 1691-1708.

[35] N. Hilleret, C. Scheuerlein, and M. Taborelli, The secondary-electron yield of air-exposed metal surfaces, Applied Physics a-Materials Science & Processing 76 (2003) 1085-1091.

[36] *Handbook of ellipsometry*; *Vol.*, edited by H. G. Tompkins and E. A. Irene (William Andrew, 2005).

[37] J. Q. Chen, E. Louis, C. J. Lee, H. Wormeester, R. Kunze, H. Schmidt, D. Schneider, R. Moors, W. van Schaik, M. Lubomska, and F. Bijkerk, Detection and characterization of carbon contamination on EUV multilayer mirrors, Optics Express 17 (2009) 16969-16979.

[38] B. D. Johs, J. Hale, N. J. Ianno, C. M. Herzinger, T. E. Tiwald, and J. A. Woollam, Recent developments in spectroscopic ellipsometry for in-situ applications, SPIE, 2001 (SPIE), 4449, p. 41-57.

[39] S. V. Singh, T. Zaharia, M. Creatore, R. Groenen, K. V. Hege, and M. C. M. v. d. Sanden, Hard graphitelike hydrogenated amorphous carbon grown at high rates by a remote plasma, Journal of Applied Physics 107 (2010) 013305.

[40] R. W. Collins, Insitu Ellipsometry as a Diagnostic of Thin-Film Growth - Studies of Amorphous-Carbon, Journal of Vacuum Science & Technology a-Vacuum Surfaces and Films 7 (1989) 1378-1385.

[41] J. Verhoeven and J. Los, The influence of an electron beam on oxidation of polycrystalline nickel surfaces, monitored by disappearance potential spectroscopy (DAPS), Surface Science 58 (1976) 566-574.

[42] J. Kirschner and P. Staib, Disappearance potential spectroscopy, Applied Physics A: Materials Science &amp; Processing 6 (1975) 99-109.

[43] C. Streli, P. Wobrauschek, V. Bauer, P. Kregsamer, R. Gorgl, P. Pianetta, R. Ryon, S. Pahlke, and L. Fabry, Total reflection X-ray fluorescence analysis of light elements with synchrotron radiation and special X-ray tubes, Spectrochimica Acta Part B-Atomic Spectroscopy 52 (1997) 861-872.

[44] C. Streli, H. Aiginger, and P. Wobrauschek, Light-Element Analysis with a New Spectrometer for Total-Reflection X-Ray-Fluorescence, Spectrochimica Acta Part B-Atomic Spectroscopy 48 (1993) 163-170.

[45] C. Streli, P. Wobrauschek, W. Ladisich, R. Reider, and H. Aiginger, Total-Reflection X-Ray-Fluorescence Analysis of Light-Elements under Various Excitation Conditions, X-Ray Spectrometry 24 (1995) 137-142.

[46] H. Hoefler, C. Streli, P. Wobrauschek, M. Ovari, and G. Zaray, Analysis of low Z elements in various environmental samples with total reflection X-ray fluorescence (TXRF) spectrometry, Spectrochimica Acta Part B-Atomic Spectroscopy 61 (2006) 1135-1140.

[47] C. Streli, P. Wobrauschek, and H. Aiginger, A New X-Ray Tube for Efficient Excitation of Low-Z-Elements with Total Reflection X-Ray-Fluorescence Analysis, Spectrochimica Acta Part B-Atomic Spectroscopy 46 (1991) 1351-1359.

[48] http://epmalab.uoregon.edu/UCB_EPMA/fluoresc.htm

[49] C. Streli, P. Wobrauschek, and I. Schraik, Comparison of SiLi detector and silicon drift detector for the determination of low Z elements in total reflection X-ray fluorescence, Spectrochimica Acta Part B-Atomic Spectroscopy 59 (2004) 1211-1213.

[50] D. Schneider and T. Schwarz, A photoacoustic method for characterising thin films, Surface & Coatings Technology 91 (1997) 136-146.

[51] D. Voreades, Secondary electron emission from thin carbon films, Surface Science 60 (1976) 325-348.

## 2 Characterization of EUV induced carbon films using laser-generated surface acoustic waves

### 2.1 Abstract

The deposition of carbon layers on the surfaces of optics exposed to extreme ultraviolet (EUV) radiation has been observed in EUV lithography. It has become of critical importance to detect the presence of the carbon layer in the order of nanometer thickness due to carbon's extremely strong absorption of EUV radiation. Furthermore, the development of efficient cleaning strategies requires that the nature of these carbon layers is well understood. Here, we present experimental results on the detection and characterization of carbon layers, grown on Mo/Si EUV reflecting optics, by laser-generated surface acoustic waves (LG-SAWs). It was found that SAW pulses with a frequency bandwidth of more than 220 MHz can be generated and detected for multilayer mirrors and LG-SAW is sensitive enough to detect EUV induced carbon layers less than 5 nm thick. It was inferred from the low Young's modulus (<100 GPa) that the carbon layer induced by EUV illumination in these vacuum conditions is mechanically soft and polymeric in nature with a high percentage of hydrogen.

### 2.2 Introduction

Extreme ultraviolet lithography (EUVL) is a next-generation lithography technology using radiation at 13.5 nm. Contamination of optics is a critical concern in the field of EUVL because it can reduce the reflectance of Mo/Si multilayer mirrors (MLMs) for optics [1] and, consequently, the throughput of the total optical system. Thus, it is necessary to be able to either prevent the deposition of contaminating films or to nondestructively clean optics periodically. In both cases, it is necessary to understand how the contamination is deposited and the resulting layer's property. In addition, efficient cleaning requires that the presence of the contamination layer be detected early in its formation, preferably before a single monolayer is complete. Here, we use surface acoustic waves (SAWs) to investigate the mechanical properties of carbon films that were grown under EUV illumination.

In previous work, X-ray photoelectron spectroscopy (XPS) and Auger electron spectroscopy (AES) have been employed to measure the thickness of EUV induced carbon contamination films [2,3]. XPS and AES are very sensitive to the presence of carbon, but are insensitive to hydrogen, which means it can not distinguish between a thin diamond-like film and a thick polymer-like film.

Ellipsometry has also been employed to characterize thin carbon films, though not grown on MLM [4]. The structure of the MLM is a complicating factor in characterizing surface films, however, the optical properties of the various phases of carbon films presents a larger problem. Although graphite-like films can be distinguished by their strong ($sp^2$) absorption in the visible-near IR region, the optical

properties of sp$^3$ dominated polymeric films are very similar to diamond-like films. Since ellipsometry only provides the optical thickness directly, one must already know the density to obtain the phase of the carbon film. This level of a priori knowledge is not usually available for novel films, such as EUV induced carbon.

On the other hand, SAW have been found to be very sensitive to the characteristics of surface films, e.g. film growth even when the thickness of the layer is much smaller than the SAW wavelength [5]. The propagation of SAW depends on the acoustic properties, such as Young's modulus, Poisson ratio, density and thickness of the surface layer and the substrate, respectively. In the case of carbon, Young's modulus varies from <100 GPa for a hydrogenated, amorphous polymeric film to ~1000 GPa for a crystalline diamond film, making it highly sensitive to the phase of the carbon layer [6]. Most importantly, it is highly sensitive to the presence of hydrogen in sp$^3$-dominated films, thus providing a clearly sensitive method for distinguishing diamond-like and hydrogenated amorphous polymeric films.

Laser-generated SAW (LG-SAW) is a convenient and efficient method to characterize the mechanical properties of thin films because it provides a broadband acoustic pulse that, after analysis, reveals much more information than a single frequency SAW [7]. LG-SAW has been broadly used to characterize amorphous carbon films (see, e.g., [5] and references therein). However, to our knowledge, LG-SAW has never been used to investigate carbon layers grown under EUV illumination. In this paper, we present results on the mechanical properties of carbon contamination films, grown under EUV illumination (which we refer to as "EUV induced carbon"). In addition, our results show that LG-SAW measurements are robust even when the substrate has a strongly heterogeneous coating, as is the case for MLMs.

## 2.3   *Experimental setup*

### 2.3.1   Carbon layer deposition

Briefly, the MLMs investigated here consist of a capping layer plus 50 bi-layers of Mo and Si, each about 7 nm thick, deposited on the (001) surface of a Si wafer. The thickness of the full multilayer stack is 357 nm. A complete description of a typical MLM structure and its properties can be found elsewhere [8].

Two MLM samples were exposed to EUV radiation from a xenon-based EUV hollow cathode discharge plasma source [9]. The source emits pulses with a pulse duration of 50-100 ns at a repetition frequency of 270 Hz. The radiation in the 10-18 nm range was selected from the broadband emission by passing the light through a zirconium filter, attached to a stainless steel box. The samples were placed in the box to protect them from direct exposure to the discharge products. In addition, each mirror stack was masked so that only half the surface was illuminated, but no measures were taken to prevent hydrocarbons from diffusing under the mask and adsorbing to the surface. The distance between the source and mirror was about 50 cm. Each mirror was

evenly illuminated by the filtered EUV light at an energy density of 1.9 $\mu J/cm^2$ per pulse, which is sufficiently low to prevent the mirror from heating significantly over the entire exposure time. The mirrors were exposed to 2 million (~2 hour exposure time) and 5 million (~5 hour exposure time) pulses respectively to obtain two different carbon layer thicknesses.

The residual hydrocarbon gases in the chamber act as the source for the carbon layer deposition. The vacuum in the chamber was between $10^{-6}$-$10^{-7}$ mbar, which increased to $10^{-3}$ mbar while the EUV source was operating, however, this increase is entirely due to additional xenon and the partial pressure of the out-gassed hydrocarbons is not expected to vary during deposition. From the residual gas analyzer (RGA) spectrum, a hydrocarbon peak can be easily discriminated from the background. The RGA spectrum showed masses between 62 and 70 mass numbers, which corresponds to hydrocarbons around the size of pentane or larger and $Xe^{2+}$.

For the purposes of comparison, a second pair of MLMs had a graphitic layer deposited on their surfaces by evaporating a graphite filament in close proximity to the MLM surface in a vacuum (which we refer to as "hot filament carbon"). The graphite wire was evaporated using a current pulse. The current pulse and resulting evaporation time was estimated to less than one second. The MLM sample was placed on a copper mount, facing the wire at a distance of 5-10 cm. The short duration of the current pulse and the copper mount ensure the temperature of the mirror does not change significantly over the duration of the exposure.

A variable angle spectroscopic ellipsometer (Woollam, VASE) was used to determine the thickness of the carbon films, assuming various carbon morphologies. The films were investigated in the wavelength range from 280 to 1550 nm, and at incidence angles of 65º, 70º and 75º. The hot filament carbon layer thicknesses were determined to be 11.9 and 24.3 nm, using a Tanguy model [10]. However, the EUV induced carbon fit two models equally well, the Tauc-Lorentz [11] and Cauchy models. This resulted in two thicknesses for each EUV induced carbon sample: 2.7 and 3.5 nm for the sample exposed for 2 million pulses and 12-15.5 nm for the sample exposed to 5 million pulses. The small values correspond to the Cauchy model, while the large values result from the Tauc-Lorentz model. Ellipsometry was also used to determine that the background level of hydrocarbon adsorption for the masked part of the MLM was ~0.6 nm thick. The layer thicknesses that we quote are the difference in carbon layer thickness between the exposed and unexposed sections of the MLM. The masked sections of the MLMs exposed to graphitic carbon were found to be identical to an unexposed MLM, indicating that the carbon did not diffuse under the mask.

## 2.3.2    LG-SAW experimental equipment

Fig. 12 shows a diagram of the LG-SAW experimental setup. A SAW pulse was generated by a nitrogen pulsed laser, with a center wavelength of 337 nm, a pulse energy of 0.4 mJ and a pulse duration of 0.5 ns (FWHM). The laser beam was focused

using a cylindrical lens to a stripe of approximately 8 by 0.012 mm, corresponding to an energy density of 417 mJ/cm$^2$, which is low enough to only excite the thermal expansion that generates a line-shaped broadband SAW pulse. An alignment bar was used to ensure that the SAW always propagated along the [110] direction of the (001) Si substrate. This is necessary due to the fact that the SAW velocity is not isotropic for the underling crystalline silicon substrate. The generated SAW pulses were detected by a piezoelectric transducer that was fixed on the mirror. More details on the experimental apparatus and following signal analysis can be found in reference [5].

The SAW pulses were detected at several different propagation distances, ranging from less than 1 cm to a few cm by translating the MLM sample with a high precision stage. The pulses were acquired by a digitizing oscilloscope, which was then transferred to a computer for computation. Amplitude and phase spectra of the pulse signals are calculated by taking the Fourier transform of a cross correlation between the piezoelectric detector's response at the shortest distance and with the responses at all other distances. The SAW dispersion curve is deduced from the phase spectra. The frequency range of the dispersion curve is determined by requiring that the amplitude of the frequency components be sufficient large.

The experimental dispersion curves were used to determine the mechanical properties of the MLM and the carbon film by fitting a theoretical dispersion curve to the measured curve by varying the related parameters, such as Young's modulus, density, Poisson ratio, and thickness. The number of parameters that can be independently determined depends on the film thickness and the difference between the mechanical properties of the film and the substrate. Note that the degree of nonlinearity of the SAW dispersion curve is crucial for determining the number of parameters that can be independently resolved.
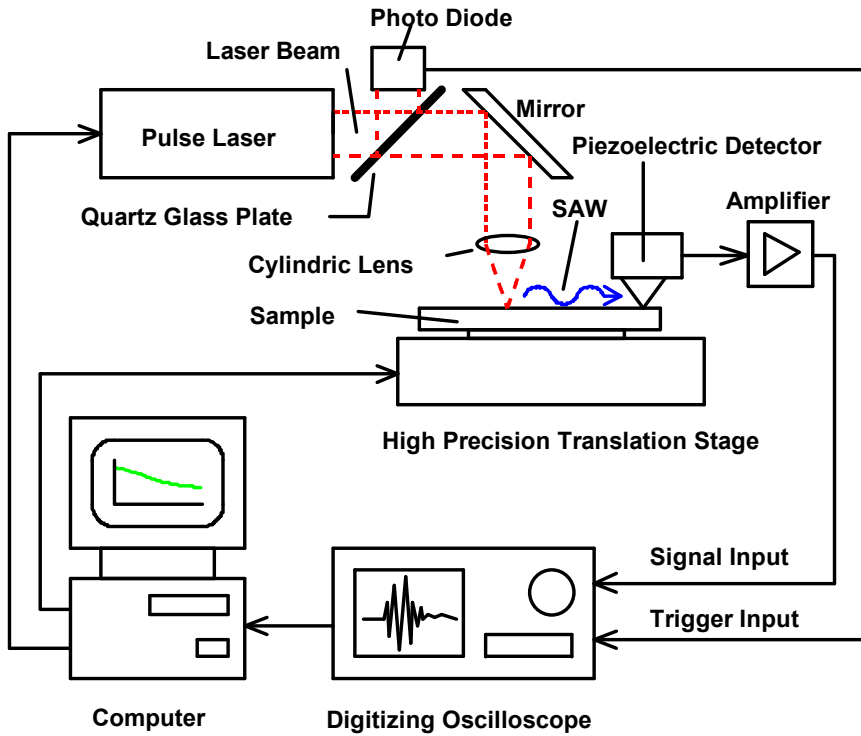
*Fig. 12. The system diagram of LG-SAW experimental setup*

## 2.4 Results

LG-SAW measurements were performed on both the exposed and unexposed sections of the MLM samples. The dispersion curves obtained from the MLMs with EUV induced carbon and hot filament carbon are shown in Fig. 13(a) and Fig. 14(a). In general, SAW pulses with wide frequency bandwidth up to 220 MHz were generated and detected. All the dispersion curves are nearly linear and exhibit normal dispersion (i.e. velocity decrease for increasing frequency), thus we can only determine a single parameter—Young's modulus—with a priori knowledge of the film density, thickness, and Poisson's ratio. Extrapolating all the dispersion curves to zero frequency reveals the SAW velocity for the substrate to be about 5081 m/s, which agrees with the propagation velocity in the [110] direction on a clean (001) silicon wafer. This is expected since the thickness of the whole multilayer (357 nm) and carbon film is small compared to the penetration depth of the SAW spectrum which is roughly comparable to the respective SAW wavelength (ca. 20-60 μm). Taking into account the well defined layer thicknesses for the MLM, and using the average value of Poisson's ratios of Mo and Si, and average densities that are 85% of the bulk value [12], we find that the effective Young's modulus for the MLM is 168 GPa, which is smaller than the average value of the Young's modulus for the bi-layer system.

We obtain the contribution of the EUV induced carbon layer by substracting the dispersion due to the MLM from the total dispersion curve (see Fig. 13 (b)). For each MLM, the dispersion from the unexposed section served as a reference. Subtraction implicitly assumes linearity, which is only valid when the layer thicknesses of the whole multilayer (357 nm) and the carbon layer (<25 nm) is small compared to the wavelength of the SAW (ca. 20-60 μm) and the corresponding SAW dispersion can be considered to be a small perturbation of the substrate dispersion [13]. The corrected curve, since it removes the dispersion of the MLM, is assumed to be the dispersion of the carbon layer as if it were directly deposited on the silicon wafer. The oscillation features at both limits of the frequency range are caused by the frequency characteristic and are not relevant to our analysis.

As can be seen in Fig. 13 (b), the slope of the corrected dispersion curve is quite close to zero for both films, though still negative, indicating that the Young's modulus of EUV induced carbon is smaller than that of the Si wafer (169 GPa). Since the dispersion curve is linear, a value for Young's modulus can only be obtained if the density, Poisson's ratio, and layer thickness are known. Normal dispersion indicates that the film cannot be diamond-like because Young's modulus must be less than 169 GPa, thus, the layer thicknesses obtained from the Tauc-Lorentz model were used (3.5 and 15.5 nm). Hydrogenated amorphous carbon films have been observed to have a density in the range of 1.0-1.6 g/cm$^3$ [14]. However, we restrict the range of values to 1.0-1.4 g/cm$^3$ based on the density range obtained by grazing incidence x-ray reflectivity. Poisson's ratio is relatively constant between different polymeric films with a value of 0.5.

Using these parameter ranges, Young's modulus was found to be 5±4 and 16±8 GPa for the 3.5 and the 15.5 nm thick films, respectively. The uncertainty in range for Young's modulus is obtained from the average and standard deviation for Young's moduli derived from multiple data sets obtained from the same location. This accurately reflects the contribution of the 0.1 m/s uncertainty in the velocity data in the original dispersion curve and also includes the influence of possible changes in the film density.

Young's modulus clearly increased with increasing thickness. It is typical to find that for films of a few nanometers thickness, the density increases as the film thickness increases until the bulk value is obtained. Thus, it is reasonable to expect that the density and Young's modulus of the thinner EUV induced carbon film is less than that of the thick layer. Alternatively, both layers may not yet be fully polymerized from the background, short chain hydrocarbons, resulting in a much more fluid-like surface with a very small Young's modulus but similar density.
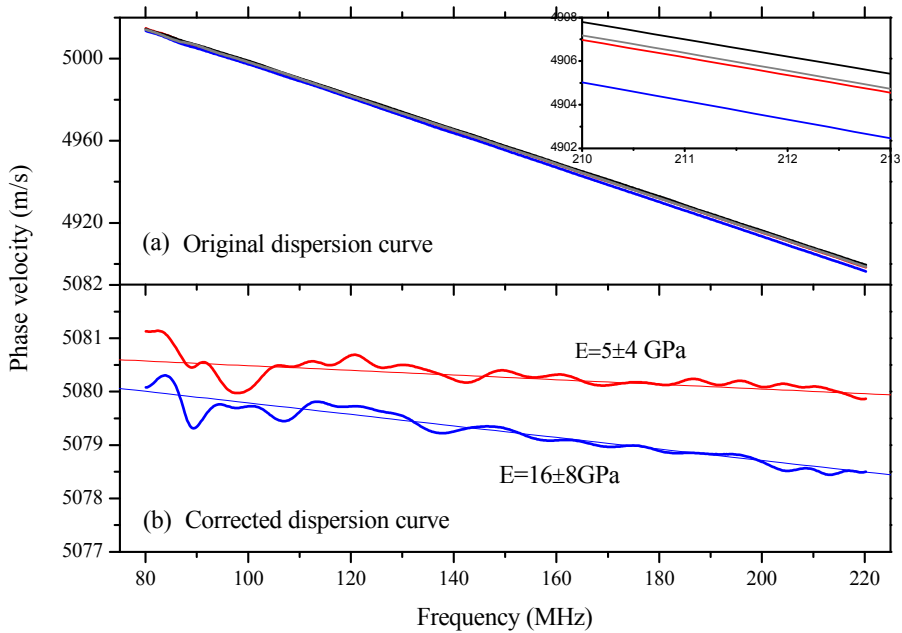
*Fig. 13. Dispersion curves measured for MLM with EUV induced carbon deposited on them. The original dispersion curves obtained from the raw data (a) with an expanded section shown in the inset figure. The black and grey lines are the dispersion curves of the unexposed MLM, while the red line and blue lines correspond to a 3.5 and a 15.5 nm thick carbon layer respectively. Subfigure (b) shows the dispersion curves with the influence of the MLM removed (see text for details). The red and blue curves correspond to the measured (thick lines) and calculated (thin lines) dispersion of the 3.5 and 15.5 nm thick carbon layers respectively.*

A similar analysis was performed on MLMs that had hot filament carbon layers deposited on them. Fig. 14(a) shows the dispersion curves of the MLM and carbon layers. The corrected dispersion in Fig. 14(b) is also linear, but with a positive slope, clearly showing the anomalous dispersion of the carbon layer. This indicates that it has a Young's modulus larger than that of the underlying silicon substrate. Since deposition took place using a pure carbon source in background conditions with no detectable hydrogen, the layers are expected to be hydrogen free amorphous carbon. Consequently, we assume that Poisson's ratio is 0.19, as is typical for hydrogen free, amorphous carbon. The density and Young's modulus for carbon deposited in this manner have been observed to be related by an empirical relationship, which we use to eliminate the density as a free parameter in the fitting procedure [15].

By fitting the corrected dispersion curve it was obtained that the Young's modulus for hot filament carbon was 371±9 GPa and 373±1 GPa for the 11.9 nm for 24.3 nm thick films, respectively. These two values are in the general range of amorphous carbon films.

In contrast to the EUV induced carbon, the values for Young's modulus are consistent between the two film thicknesses, indicating that the carbon layer's density and morphology do not change much over the course of the deposition by this method. This is not unexpected since the deposition time is very short and the MLM surface temperature was kept at room temperature, leaving little chance for annealing. On the other hand, EUV induced carbon is subject to constant bombardment by ~90 eV photons and lower energy photoelectrons during a deposition process that lasts for 2-5 hours.
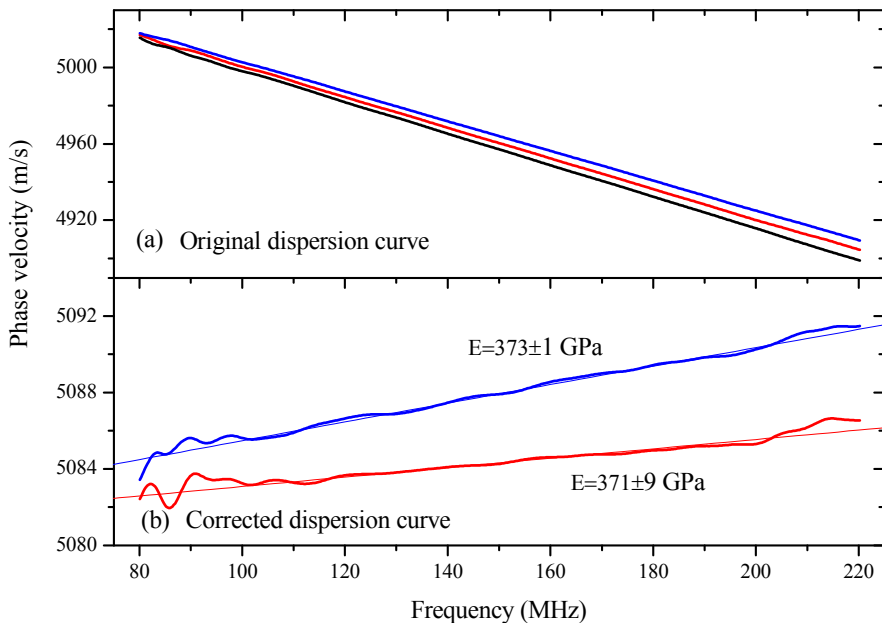


*Fig. 14. Dispersion curves measured for MLM with hot filament carbon deposited on them. The original dispersion curves obtained from the raw data are shown in (a). The black line is the dispersion of an unexposed MLM, while the red line and blue lines correspond to an 11.9 and a 24.3 nm thick carbon layers respectively. Subfigure (b) shows the dispersion curves with the influence of the MLM removed (see text for details). The red and blue curves correspond to the measured (thick lines) and calculated (thin lines) dispersion of the 11.9 and 24.3 nm thick carbon layers respectively.*

## *2.5    Conclusions*

We have presented the first LG-SAW experiments on MLM structures with a further layer of carbon deposited on top of that using two different deposition methods: hot filament deposited carbon and EUV photo-induced hydrocarbons. The mechanical properties of two different carbon films have been analyzed and compared. The Young's modulus of the hot filament carbon was about 370 GPa, which is in the general range of amorphous carbon films. Furthermore, the consistency of the measurements indicates that the carbon layer's mechanical properties do not change significantly as the layer thickness increases. However, carbon layers deposited from ambient hydrocarbons under illumination of EUV radiation had a Young's modulus that increased significantly with layer thickness. The small Young's modulus (<100 GPa) leads us to conclude that EUV induced carbon is mechanically soft, and polymer-like. In addition, it was also found that LG-SAW is sensitive enough to detect EUV induced carbon growth less than 5 nm, which is within an order of magnitude of the sensitivity required for EUVL contamination monitoring.

## *2.6    Acknowledgements*

## *2.7    References*

[1]  S. Oestreich, R. Klein, F. Scholze, J. Jonkers, E. Louis, A. E. Yakshin, P. C. Goerts, G. Ulm, M. Haidl, and F. Bijkerk, Multilayer reflectance during exposure to EUV radiation, Soft X-Ray and EUV Imaging Systems, San Diego, CA, USA, 2000 (SPIE), 4146, p. 64-71.

[2]  G. Kyriakou, D. J. Davis, R. B. Grant, D. J. Watson, A. Keen, M. S. Tikhov, and R. M. Lambert, Electron impact-assisted carbon film growth on Ru(0001): Implications for next-generation EUV lithography, Journal of Physical Chemistry C 111 (2007) 4491-4494.

[3]  S. Matsunari, T. Aoki, K. Murakami, Y. Gomei, S. Terashima, H. Takase, M. Tanabe, Y. Watanabe, Y. Kakutani, M. Niibe, and Y. Fukuda, Carbon deposition on multi-layer mirrors by extreme ultra violet ray irradiation, Emerging

Lithographic Technologies XI, San Jose, CA, USA, 2007 (SPIE), 6517, p. 65172X-8.

[4]  B. Johs, J. A. Woollam, C. M. Herzinger, J. Hilfiker, R. Synowicki, and C. L. Bungay, Overview of Variable Angle Spectroscopic Ellipsometry (VASE), Part II: Advanced Applications, SPIE, Denver, Colorado, 1999 (SPIE), CR72, p. 29-58.

[5]  D. Schneider and T. Schwarz, A photoacoustic method for characterising thin films, Surface & Coatings Technology 91 (1997) 136-146.

[6]  D. Schneider and B. Schultrich, Elastic modulus: a suitable quantity for characterization of thin films, Surface & Coatings Technology 98 (1998) 962-970.

[7]  M. Weihnacht, K. Franke, K. Kammer, R. Kunze, and H. Schmidt, High precision characterization of SAW materials and devices, IEEE Ultrasonics Symposium, 1997, 1, p. 217-220 vol.1.

[8]  E. Louis, H. J. Voorma, N. B. Koster, L. Shmaenok, F. Bijkerk, R. Schlatmann, J. Verhoeven, Y. Y. Platonov, G. E. Vandorssen, and H. A. Padmore, Enhancement of Reflectivity of Multilayer Mirrors for Soft-X-Ray Projection Lithography by Temperature Optimization and Ion-Bombardment, Microelectronic Engineering 23 (1994) 215-218.

[9]  K. Bergmann, O. Rosier, R. Lebert, W. Neff, and R. Poprawe, A multi-kilohertz pinch plasma radiation source for extreme ultraviolet lithography, Microelectronic Engineering 57-8 (2001) 71-77.

[10] C. Tanguy, Analytical expression of the complex dielectric function for the Hulthen potential, Physical Review B 60 (1999) 10660-10663.

[11] G. E. Jellison and F. A. Modine, Parameterization of the optical functions of amorphous materials in the interband region, Applied Physics Letters 69 (1996) 2137-2137.

[12] H. J. Voorma, E. Louis, N. B. Koster, F. Bijkerk, and E. Spiller, Characterization of multilayers by Fourier analysis of x-ray reflectivity, Journal of Applied Physics 81 (1997) 6112-6119.

[13] D. Schneider, T. Witke, T. Schwarz, B. Schoneich, and B. Schultrich, Testing ultra-thin films by laser-acoustics, Surface & Coatings Technology 126 (2000) 136-141.

[14] J. Robertson, Diamond-like amorphous carbon, Materials Science & Engineering R-Reports 37 (2002) 129-281.

[15] D. Schneider, T. Schwarz, H. J. Scheibe, and M. Panzner, Non-destructive evaluation of diamond and diamond-like carbon films by laser induced surface acoustic waves, Thin Solid Films 295 (1997) 107-116.

## 3 Detection and characterization of carbon contamination on EUV multilayer mirrors

### 3.1 Abstract

In this paper, we detect and characterize the carbon contamination layers that are formed during the illumination of extreme ultraviolet (EUV) multilayer mirrors. The EUV induced carbon layers were characterized *ex situ* using spectroscopic ellipsometry (SE) and laser-generated surface acoustic waves (LG-SAWs). We show that both LG-SAW and SE are very sensitive for measuring carbon layers, even in the presence of the highly heterogeneous structure of the multilayer. SE has better overall sensitivity, with a detection limit of 0.1 nm, while LG-SAW has an estimated detection limit of 1.2 nm. In addition, SE reveals that the optical properties of the EUV induced carbon contamination layer are consistent with the presence of a hydrogenated, polymeric like carbon. On the other hand, LG-SAW reveals that the EUV induced carbon contamination layer has a low Young's modulus (<100 GPa), which means that the layer is mechanically soft. We compare the limits of detection and quantification of the two techniques and discuss their prospective for monitoring carbon contamination build up on EUV optics.

### 3.2 Introduction

The semiconductor industry's desire to create smaller integrated circuit features on semiconductors has been a major driver for the development of lithographic techniques and quality optics for short wavelengths. As a part of this trend, the development of EUV lithography, aimed to operate at 13.5 nm, and its component optics has been a major focus over the last ten years. Bragg reflecting optics, i.e. multilayer mirrors (MLMs) must be used because materials are highly absorbing at short wavelengths. MLMs, constructed from alternating layers of silicon and molybdenum, can reach a 69.5% reflectivity [1]. However, there are about ten such optics in the light collection and imaging train, meaning that the throughput of the system is just a few percent. Under these circumstances it is very important to maximize throughput by eliminating or removing surface contaminants that are deposited within the wafer scanner itself.

Wafer scanners may operate under non-UHV conditions. In case of a background pressure on the order of $10^{-3}$ mbar, and a residual gas mixture consisting of many different components including water, oxygen and hydrocarbons, the two main sources of contamination are oxidation and the build up of carbon contamination layers. Water acts as an oxidizer, which will etch away soft surfaces, such as silicon. This is usually prevented by using a heavy metal capping layer that forms a stable oxide layer and prolongs the life of the mirror, albeit with a small reflectivity loss.

Unfortunately, the capping layer does not prevent the build up of carbon contamination, leaving it as the main surface contamination process [2]. Even under relatively good vacuum conditions, carbon contamination has been observed, as evidenced by the examination of synchrotron beam line optics [3]. The extremely high absorption of EUV radiation by carbon makes the contamination layer a serious source of loss of optical throughput. For instance, IMD modeling [4] shows that a 1 nanometer thick layer of pure graphite leads to a 2.1% reduction in relative reflectivity ($\Delta R/R_0$) from a single multilayer optic surface. If such a layer were to form on every reflecting surface, it would consume the full lifetime budget of EUVL scanner optics (typically consisting of ten reflecting surfaces). Clearly, such maintenance shutdowns are undesirable, making it necessary to detect, and characterize contaminants before significant optical absorption is observed so that mirror surfaces may be cleaned *in situ* without opening the vacuum chamber. Therefore, a successful monitoring of the contamination process should have a low detection limit, a high sensitivity, a high accuracy and it should be rapid.

This makes it critical to explore and develop techniques that can, during the integrated circuit fabrication processes, accurately detect and track the development of carbon contamination. Critical to achieving accurate carbon contamination monitoring is understanding what form of carbon is deposited on the multilayer structure. Subsequently, a detection technique that has an optimal response to the carbon layer's characteristics can be chosen.

Several techniques have been shown to be sensitive to surface contamination. X-ray photoelectron spectroscopy (XPS) and Auger electron spectroscopy (AES) [5,6], Auger depth profiling analysis [2,7] have been employed to measure the thickness or concentration of EUV induced carbon contamination films. However, these techniques lack sub-nanometer limits of detection and sensitivities. For XPS, there is an additional difficulty due to the potential binding energy overlap between the contamination and capping layer of mirror. Finally, all of these techniques require substantial amounts of space within the vacuum chamber for the electron detector. It makes them undesirable because of the very compact design of the EUVL equipment.

On the other hand, ellipsometry is a non-contact, non-destructive and very sensitive technique that uses polarized light to characterize thin films, surfaces, and material microstructure [8-10]. Spectroscopic ellipsometry (SE) can be used to determine optical constants and layer thickness in multilayer stacks. SE also has the advantage that, in measuring changes in polarization, the instrument is largely immune to the intensity noise of the light source. In contrast, reflectivity measurements must be referenced to the input light intensity, adding an additional source of noise. In addition, *in situ* SE has already been developed and applied in some areas of deposition monitoring and active process control [11,12]. The light source, analyzer and other components can remain outside of the vacuum, meaning that only line-of-sight optical

access is required. Furthermore, *in situ* SE has been shown to possess sub-monolayer resolution during deposition processes [13].

The surface mechanical properties are also sensitive to changes to the composition of the surface. Surface acoustic waves (SAWs), and in particular, laser-generated SAW (LG-SAW) can be used to characterize the mechanical properties of thin films, even when the thickness of the layer is much smaller than the SAW wavelength [14]. The propagation of SAW depends on the acoustic properties, such as Young's modulus, Poisson's ratio, density, and thickness of the surface and substrate layers. The remote excitation of the acoustic pulse, via a laser pulse, requires only that optical access to the MLM surface is possible, while detection can be achieved using piezoelectric foils or laser interferometry [15].

In this paper, the EUV induced carbon contamination on MLMs has been characterized *ex situ* by SE and LG-SAW. We investigated the sensitivity of both SE and LG-SAW for two carbon layer morphologies. Although SE has a lower limit of detection, we find that LG-SAW is able to distinguish different phases of carbon more accurately.

### 3.3    Methodology

#### 3.3.1    Carbon layer deposition

Briefly, the MLMs investigated here consist of a capping layer plus 50 bi-layers of Mo and Si, each about 7 nm thick, deposited on the (001) surface of a Si wafer. The thickness of the full multilayer stack is 357 nm. A complete description of a typical MLM structure and its properties can be found elsewhere [16].

The MLMs were exposed to EUV radiation from a xenon-based EUV hollow cathode discharge plasma source [17]. The source emits pulses with a duration of 50-100 ns at a repetition frequency of 270 Hz. The radiation in the 10-18 nm range was selected from the broadband emission by passing the light through a zirconium filter attached to a stainless steel box. The samples were placed in the box to protect them from direct exposure to the discharge products. In addition, each mirror was masked so that only half the surface was illuminated, but no measures were taken to prevent hydrocarbons from diffusing under the mask and adsorbing to the surface. The distance between the source and mirror was about 50 cm. Each mirror was evenly illuminated by the filtered EUV light at an energy density of 1.9 $\mu J/cm^2$ per pulse, which is sufficiently low to prevent the mirror from heating significantly over the entire exposure time. Four mirrors were exposed to 0.6 million (~0.6 hour exposure time), 2 million (~2 hour exposure time), 4 million (~4 hour exposure time), and 5 million (~5 hour exposure time) pulses, respectively to obtain four different carbon layer thicknesses.

The residual hydrocarbon gases in the chamber act as the source for the carbon layer deposition. The vacuum in the chamber was between $10^{-6}$ and $10^{-7}$ mbar, which increased to $10^{-3}$ mbar while the EUV source was operating, however, this increase is

mainly due to additional xenon. From the residual gas analyzer (RGA) spectrum, a hydrocarbon peak can be easily discriminated from the background. The RGA spectrum showed masses between 62 and 70 mass numbers, which corresponds to $Xe^{2+}$ and background hydrocarbons around the size of pentane or larger.

For the purposes of comparison, additional pairs of MLMs had an amorphous carbon layer deposited on their surfaces by evaporating a graphite filament in close proximity to the MLM surface in a vacuum (which we refer to as "hot filament carbon"). The graphite wire was evaporated using a current pulse. The current pulse and resulting evaporation time was estimated as less than one second. The MLM sample was placed on a copper mount, facing the wire at a distance of 5-10 cm. The short duration of the current pulse and the copper mount ensure the temperature of the mirror does not change significantly over the duration of the exposure.

### 3.3.2   Spectroscopy ellipsometry

Ellipsometry measures the change in polarization state of light beam reflected from the surface of a sample. Generally, the change in polarization is expressed by two ellipsometric angles, i.e. psi ($\Psi$) and delta ($\Delta$), which is related to the ratio of two Fresnel reflection coefficients $r_p$ and $r_s$ for $p$- and $s$- polarized light, respectively.

$$\frac{r_p}{r_s} = \tan(\Psi)e^{i\Delta} \tag{8}$$

A variable angle spectroscopic ellipsometer (Woollam, VASE) was used to determine the thickness and optical constants of the carbon films, assuming different carbon morphologies. The films were investigated in the photon energy range 0.8-4.5 eV (280-1550 nm), and at incidence angles of 65°, 70° and 75° with respect to the surface normal. A single scan takes about 10 minutes, but this can be substantially reduced by using more sophisticated detectors.

The directly measured parameters, $\Psi$ and $\Delta$, do not directly yield the quantities of interest, such as the film thickness and optical constants. Rather, they are functions of the parameters of interest, which are obtained by fitting the measured $\Psi$ and $\Delta$ to an optical model. The parameters of interest can then be obtained from a regression analysis.

### 3.3.3   Laser-generated surface acoustic waves

The LG-SAW experimental setup (see Fig. 15) and operating parameters are described elsewhere [18]. In short, the surface acoustic wave dispersion was determined by the propagation characteristics of a short acoustic pulse. The experimental dispersion curves were used to determine the mechanical properties of the MLM and the carbon film by fitting a theoretical dispersion curve to the measured curve by varying the related parameters, such as Young's modulus, density, Poisson's ratio, and thickness. The number of parameters that can be independently determined depends on the film

thickness and the difference between the mechanical properties of the film and the substrate. Note that the degree of nonlinearity of the SAW dispersion curve is crucial for determining the number of parameters that can be independently resolved [14].
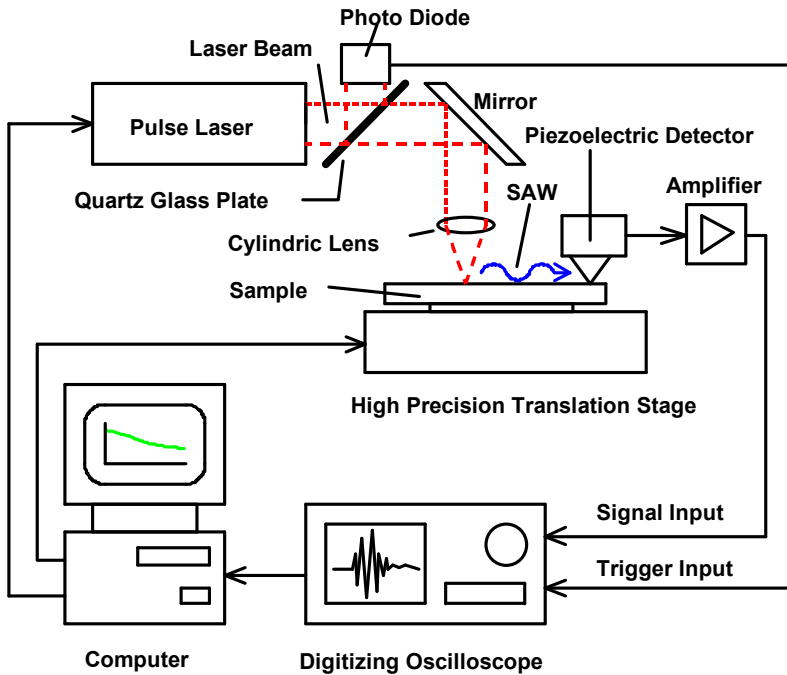


*Fig. 15. The system diagram of LG-SAW experimental setup*

## 3.4 Results of SE

### 3.4.1 MLM

The multilayer structure of a mirror is quite complex as it contains more than 100 layers, each several nanometers thick. In addition, the optical properties of the multilayer itself and interfacial layers are still not very well known in the 0.8-4.5 eV photon energy range. In order to extract the thickness and optical constants of the carbon film, the uncontaminated MLM was first characterized. We used an effective dielectric function to describe the optical properties of the MLM. The effective dielectric function simplifies the optical model of the MLM, including a storage related contamination layer, by modeling it as a single "pseudo substrate". The optical constants of the pseudo substrate were obtained from a direct inversion (i.e. it is assumed to be a bulk substrate) of the ellipsometric parameters. Fig. 16 shows the resulting effective dielectric function of the MLM. It was assumed that the optical constants of the pseudo substrate, including the storage related contamination layer, do not vary significantly during EUV illumination. It is also observed that all mirrors with

the same deposition conditions, even mirrors that are manufactured at different times, have the same optical properties, based on the Ψ and Δ data.
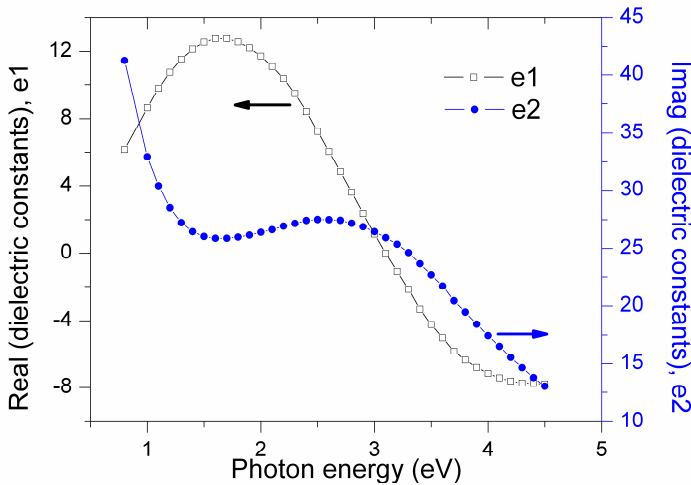


*Fig. 16. The effective optical constants of a MLM*

The analysis of the carbon contamination layer is done via a standard three-phase model. In this model, the optical properties of two of the phases: the pseudo substrate, and ambient air are set to pre-determined values. The thickness and optical properties of the third phase, which is the contamination layer, are varied to obtain a good fit to the measured Ψ and Δ data.

### 3.4.2 Dielectric model of the carbon layers

To interpret the experiment results presented in Fig. 17, a suitable optical model must be chosen. X-ray Photoelectron Spectroscopy (XPS) measurements (data not shown) revealed that the contamination due to EUV illumination is dominated by carbon. But since XPS cannot detect hydrogen and it is very difficult to determine the nature of the carbon layer. On the other hand, LG-SAW results, presented in section 3.5.2, indicate that the layer is mechanically soft (Young's modulus < 100 GPa) and polymer-like. These results lead us to conclude that the layer is probably a partially hydrogenated amorphous carbon layer. This is supported by the findings of Hollenshead *et al.* who found that surface contamination during EUV illumination consists of a partially hydrogenated amorphous carbon layer [2].

Jellison and Modine have developed a Tauc-Lorentz (TL) model to describe the optical properties of amorphous semiconductors and insulators in the interband region [19,20]. This model has been broadly applied to characterize a-C and a-C:H films [21-24]. We will also use this model to describe the properties of the EUV induced

contamination layer. In the TL model, the combination of the Tauc joint density of states [25] and the quantum mechanical Lorentz oscillator have been used to describe the imaginary part of the dielectric function $e2$ as:

$$e2(E) = \left[ \frac{AE_0C(E - E_g)^2}{\left(E^2 - E_0{}^2\right)^2 + C^2E^2} \cdot \frac{1}{E} \right] \quad \text{for } E > E_g \tag{9}$$

$$e2(E) = 0 \quad \text{for } E <= E_g \tag{10}$$

where $A$ (the amplitude), $E_0$ (the peak transition energy), $E_g$ (the optical band gap) and $C$ (the broadening term) are four fitting parameters with units of energy, while $E$ is the photon energy. The corresponding real part of the dielectric function can be found from the Kramers-Kronig relationship. The band gap is used as a cutoff energy so that photons with energy less than $E_g$ suffer no absorption.

The films obtained by hot filament carbon evaporation are not expected to have significant hydrogen content. Additionally, the deposition conditions are inconsistent with those that deposit diamond-like carbon films. Furthermore, the LG-SAW results, presented in section 3.5.2, show that the Young's modulus is about 370 GPa, which is in the general range of amorphous carbon films. The Tanguy model [26-28] was recently developed to provide an analytical expression of dielectric constants of Wannier excitons, including bound and unbound states. It has been introduced to describe the optical properties of gallium arsenide [29]. Here, we also use Tanguy model for the hot filament carbon films.
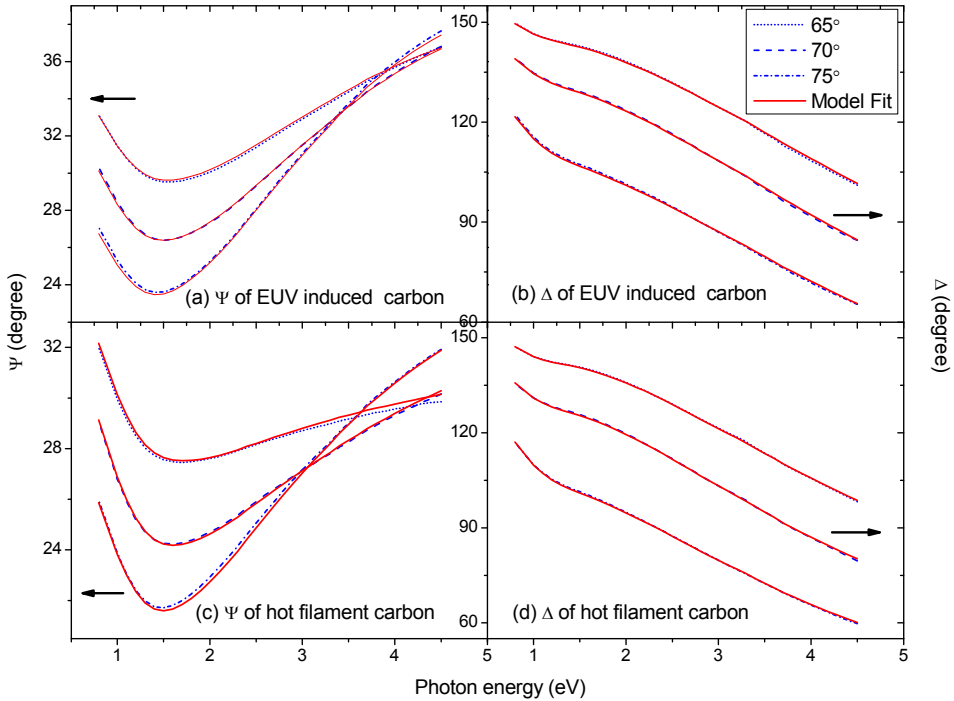
*Fig. 17. The fitting of ellipsometric angles Ψ and Δ for the MLM deposited by 16.1 nm EUV induced carbon and 11.9 nm hot filament carbon.*

### 3.4.3    Fitting results

The fitting results are shown in Fig. 17. A good fit, with a mean-squared error (MSE) < 1 is obtained for both EUV induced carbon and hot filament carbon films. The optical properties of EUV induced carbon were determined from the MLM exposed to the most EUV illumination (5 Mega pulses). These parameters were then held fixed for all other EUV induced carbon films, leaving only the layer thickness as a free parameter. All of the fitting resulted in MSE < 1, indicating that the optical properties of the thinner layers are quite similar to the thickest layer. A simultaneous fit of thickness and optical properties for the very thin layers would show too large a dependence between fit parameters and therefore large inaccuracies of the fit results. The dielectric function of EUV induced carbon films are shown in Fig. 18 (a). The film is almost transparent throughout the visible and near infrared region, as expected for polymer-like hydrocarbon and diamond-like carbon. However, the real part of dielectric function is less than the value generally reported for diamond-like carbon and is similar to polymer-like hydrocarbon (e.g. polypropylene) [23].

A similar procedure was used for the hot filament carbon films. As can be seen in Fig. 17 (c) and (d), a good fit is obtained for the film of 11.9 nm. But the error

margins of a few parameters in Tanguy model are relatively high. We do not yet fully understand why these parameters are less tightly constrained by the fitting process, or if these errors mean that a more suitable model could be found. However, the resulting thicknesses are comparable to results obtained using X-ray diffraction analysis. The dielectric function of the hot filament carbon film is also shown in Fig. 18 (b). The strong broad absorption in the visible region is clearly visible, confirming the general amorphous carbon nature of the film.

SE can clearly distinguish between these two carbon films, indicating that it should be possible to determine the hydrogen content of the films from their optical properties. However, this requires a hydrogen sensitive technique to provide independent calibration, which is beyond the scope of this work.
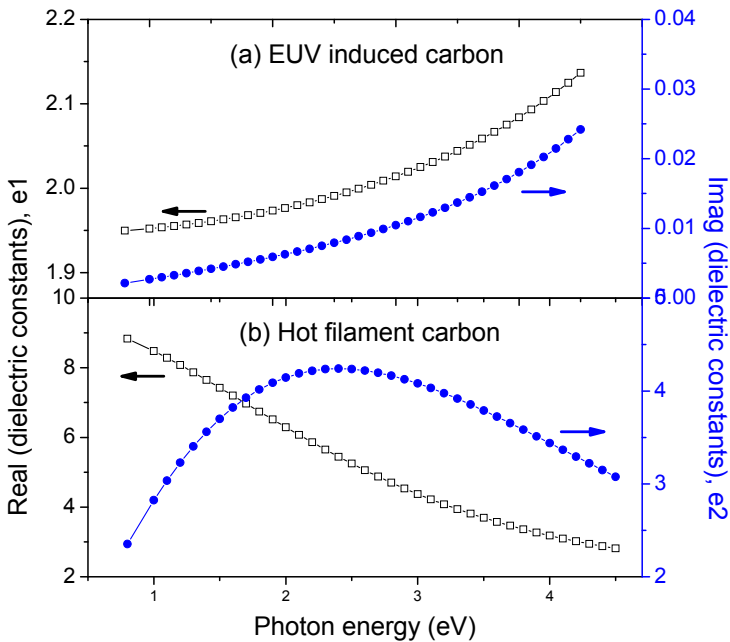


*Fig. 18. The dielectric constants of EUV induced carbon contamination film (a) and hot filament carbon film (b).*

### 3.4.4    The limit of detection

The limit of detection has been investigated for EUV induced carbon films in order to check the feasibility for sub-nanometer *in situ* carbon contamination monitoring for EUV optics. Fig. 19 plots ellipsometric angles $\Psi$ and $\Delta$ as a function of thickness at 4 eV and 75°. The sensitivity of $\Psi$ and $\Delta$ for thicknesses up to 1.0 nm is 0.5 and 2.4

degree per nanometer, respectively. The uncertainty of individual $\Psi$ and $\Delta$ measurements are about 0.3 and 0.7 degrees, respectively.

The uncertainty in the thickness of the EUV induced carbon layer has two sources: the uncertainty of its optical constants, and the measurement uncertainty of $\Psi$ and $\Delta$. The uncertainty due to the optical constants is a systematic uncertainty because they are not independently measured. However, these uncertainties are unlikely to be significant because the measured thicknesses for different EUV induced carbon samples are consistent with the changes in illumination time.

In our case, the uncertainty of an individual thickness measurement is less than 0.1 nm (with the optical constants held fixed). The limit of detection, calculated as three times of the standard deviation (with the optical constants held fixed), is about 0.1 nm. Note that a state-of-the-art ellipsometer has an order of magnitude less uncertainty in $\Psi$ and $\Delta$, so we can expect that the detection limit can be reduced to sub-monolayer thicknesses.
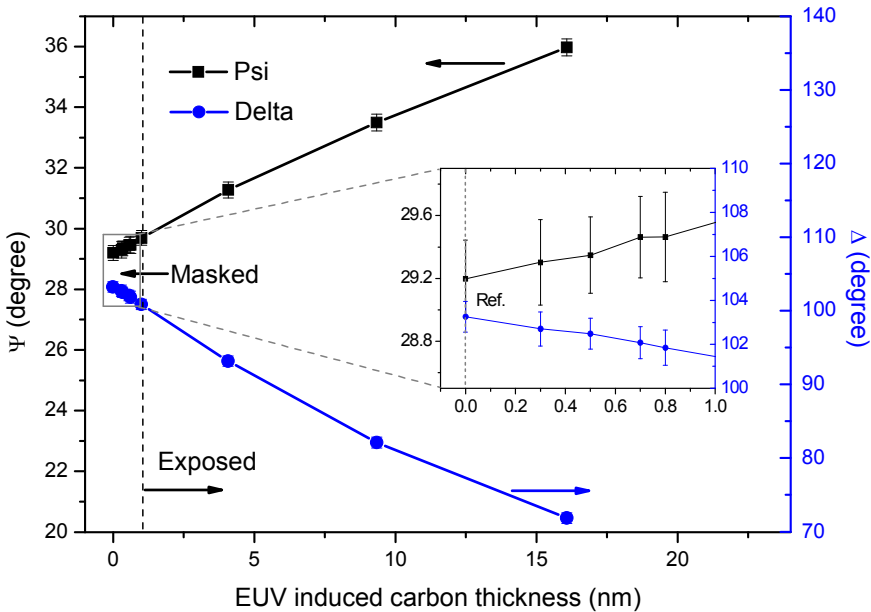


*Fig. 19. Ellipsometric angles psi and delta as a function of EUV induced carbon thickness at 4 eV and 75° with an expanded section shown in the inset figure.*

### 3.5    Results of LG-SAW

#### 3.5.1    MLM

LG-SAW measurements were performed on both the exposed and masked sections of the MLM samples under EUV illumination. In general, SAW pulses with a frequency bandwidth up to 220 MHz were generated and detected. Taking into account the well defined layer thicknesses for the MLM, and using the average value of Possion's ratios of Mo and Si, and average densities that are 85% of the bulk value [30], we find that the effective Young's modulus for the MLM is 168 GPa.

#### 3.5.2    Dispersion curves fitting

To characterize the properties of the carbon layer on the MLM, the carbon layer's contribution to the SAW dispersion must be separated from the dispersion of the underlying MLM. An approach to achieving this separation is to subtract the dispersion curve due to the unexposed section of the MLM from the dispersion curve obtained from the exposed section. This corrected dispersion curve is then used to characterized the properties of the carbon layer. The dispersion curves obtained from the MLMs with EUV induced carbon and hot filament carbon are shown and analyzed in reference [18] in detail. For EUV induced carbon layers with thicknesses of 3.5 and 15.5 nm (corrected by the masked part of the MLM), the slope of corrected dispersion curve is quite close to zero, though still negative, indicating that the Young's modulus of EUV induced carbon is smaller than that of the Si wafer (169 GPa). Young's modulus was found to increase with thickness from 5±4 GPa for a 3.5 nm thick carbon layer to 16±8 GPa for a 15.5 nm thick films. It is typical to find that Young's modulus increases with film thickness for layers only a few nanometers thick.

A similar analysis was performed on MLMs that had hot filament carbon layers deposited on them. The corrected dispersion curve is also linear, but with a positive slope, clearly showing anomalous dispersion. This indicates that it has a Young's modulus larger than that of the underlying silicon substrate. By fitting the corrected dispersion curve, Young's modulus was found to be 371±9 GPa and 373±1 GPa for the 11.9 nm for 24.3 nm thick films, respectively. This small difference is expected since the deposition time is very short and the MLM surface temperature was kept at nearly room temperature, leaving little chance for annealing. In contrast, EUV induced carbon is subject to constant bombardment by ~90 eV photons and lower energy photoelectrons during an illumination that lasts for 2-5 hours.

#### 3.5.3    The limit of detection

Based on the measurements on EUV induced carbon films on top of MLMs [18], the uncertainty of SAW dispersion curve is about 0.1 m/s. Since the dispersion curve is linear, a value for the layer thickness can only be obtained if the density, Young's

modulus and Poisson's ratio are known. In general, these parameters are not well known for EUV induced carbon films, and consequently, contribute greatly to the uncertainty of the measurement.

Aside from these considerations, it should be noted that detection is not the same as characterization, where, for detection, we require that the dispersion curve is detectably different from a reference curve. LG-SAW was found to be sensitive enough to characterize a EUV induced carbon layer with a thickness of 3.5 nm on top of a MLM. So the detection limit is somewhat less than 3.5 nm. The calculation of the limit of detection is complicated by the fitting procedure, however, it can be estimated from the uncertainty of dispersion curve slope. The standard deviation of slope fitting of 10 measurements on the same location is $5.1 \times 10^{-4}$ ms$^{-1}$MHz$^{-1}$. In contrast, the slope observed for the 3.5 nm thick layer is $4.4 \times 10^{-3}$ ms$^{-1}$MHz$^{-1}$. This leads to an estimate of 1.2 nm for the limit of detection for EUV induced carbon layers on a MLM.

On the other hand, LG-SAW can discriminate these two different carbon films based on their acoustic properties, i.e. the absolute speed of SAW. The SAW phase velocity of EUV induced carbon is less than the propagation velocity of about 5081 m/s in the [110] direction on a clean (001) silicon wafer. But for hot filament carbon, the phase velocity is larger than that of the silicon wafer.

## 3.6    *Discussion and conclusion*

To place our results in a wider context, we measured the EUV reflectance for these carbon contaminated MLMs with a reflectometer at the radiometry laboratory of the Physikalisch-Technische Bundesanstalt (PTB) at the BESSY II electron storage ring [31]. This enabled us to measure the absolute reflectance with a relative uncertainty of 0.2%. Fig. 20 shows the loss of the maximum reflectance as a function of carbon growth for both hot filament and EUV induced carbon. It shows that the reflectance loss of hot filament carbon is larger than the EUV induced carbon with the same thickness. The relative reflectance loss is 1.1% (i.e. absolute loss 0.7%, ~ three times the measurement uncertainty) when a MLM has a 1.0 nm thick layer of EUV induced carbon on top of it. In contrast, Hollenshead and Klebanoff [2] claimed that the projection optics of an EUVL equipment should not lose more than 1.6% reflectance per optic. Thus, ellipsometry would be sensitive enough for contamination monitoring. In addition, sub-monolayer detection is achievable with a state-of-the-art ellipsometer. As noted in the introduction, SE is non-contact, non-destructive and fast if advanced CCD detection applied, making it a good candidate for contamination monitoring. On the other hand, as our results show, it can be difficult to choose the best model from which physical parameters are derived. This makes it critical to understand contamination mechanisms and what form of carbon is likely to form over a range of EUVL operating.

LG-SAW is relatively simpler to set up and the data interpretation is easier than for SE. However, it is not as sensitive or as fast as SE. It is also, currently, a contact

technique, in which a piezoelectric detector has to be fixed on top of the sample. In addition, the LG-SAW measurement methodology makes contamination mapping not straightforward. More importantly, according to the specifications of the piezoelectric detector we used, it will not work properly at temperatures higher than 100 °C, which could be a limitation for some optics.

One limitation of using LG-SAW is the substrate requirement. In order to generate and detect SAW at high frequencies (about 200 MHz), the substrate must be crystalline to have a sufficiently low absorption. This requirement may not be met for some optics. In addition, the difference between dispersion curves from different MLM references is about 1.6 m/s at 200 MHz, due to differences between different MLM and substrates. This velocity difference is larger than the velocity change due to 3.5 nm of EUV induced carbon, meaning that reference dispersion curves for individual MLMs must be obtained.
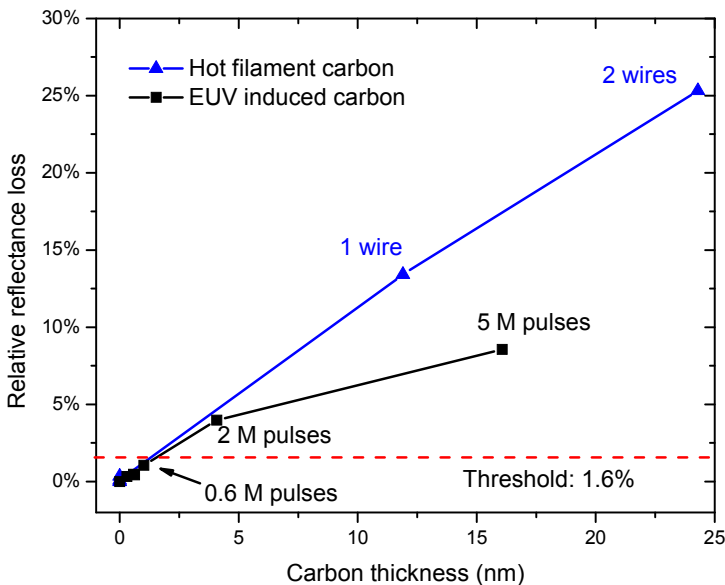


*Fig. 20. Relative EUV reflectance loss as a function of carbon thickness. The triangles are hot filament carbon with two different thicknesses by evaporating 1 and 2 wires of graphite. The squares are EUV induced carbon growth with three different amounts of EUV pulses, 0.6, 2 and 5 mega pulses.*

### 3.7   Acknowledgements

### *3.8    References*

[1]  E. Louis, A. E. Yakshin, P. C. Goerts, S. Oestreich, R. Stuik, L. G. M. Edward, M. J. H. Kessels, B. Fred, H. Markus, M. Stefan, M. Michael, S. Detlef, S. Frank, and U. Gerhard, Progress in Mo/Si multilayer coating technology for EUVL optics, SPIE, 2000 (SPIE), 3997, p. 406-411.

[2]  J. Hollenshead and L. Klebanoff, Modeling radiation-induced carbon contamination of extreme ultraviolet optics, Journal of Vacuum Science & Technology B 24 (2006) 64-82.

[3]  K.-J. Boller, R.-P. Haelbich, H. Hogrefe, W. Jark, and C. Kunz, Investigation of carbon contamination of mirror surfaces exposed to synchrotron radiation, Nuclear Instruments and Methods in Physics Research 208 (1983) 273-279.

[4]  D. L. Windt, IMD - Software for modeling the optical properties of multilayer films, Computers in Physics 12 (1998) 360-370.

[5]  S. Matsunari, T. Aoki, K. Murakami, Y. Gomei, S. Terashima, H. Takase, M. Tanabe, Y. Watanabe, Y. Kakutani, M. Niibe, and Y. Fukuda, Carbon deposition on multi-layer mirrors by extreme ultra violet ray irradiation, SPIE, San Jose, CA, USA, 2007 (SPIE), 6517, p. 65172X-8.

[6]  G. Kyriakou, D. J. Davis, R. B. Grant, D. J. Watson, A. Keen, M. S. Tikhov, and R. M. Lambert, Electron impact-assisted carbon film growth on Ru(0001): Implications for next-generation EUV lithography, Journal of Physical Chemistry C 111 (2007) 4491-4494.

[7]  N. Koster, B. Mertens, R. Jansen, A. van de Runstraat, F. Stietz, M. Wedowski, H. Meiling, R. Klein, A. Gottwald, F. Scholze, M. Visser, R. Kurt, P. Zalm, E. Louis, and A. Yakshin, Molecular contamination mitigation in EUVL by environmental control, Microelectronic Engineering 61-2 (2002) 65-76.

[8]  R. W. Collins, D. E. Aspnes, and E. A. Irene, Spectroscopic ellipsometry, Elsevier Science S.A., Lausanne, Switzerland, 1998.

[9]  J. A. Woollam, C. L. Bungay, L. Yan, D. W. Thompson, and J. N. Hilfiker, Application of spectroscopic ellipsometry to characterization of optical thin films, SPIE, 2003 (SPIE), 4932, p. 393-404.

[10] J. A. Woollam, Overview of Variable Angle Spectroscopic Ellipsometry (VASE), Part I: Basic Theory and Typical Applications, the 44th SPIE meeting, 1999.

[11] D. J. Blaine, H. Jeff, J. I. Natale, M. H. Craig, E. T. Thomas, and A. W. John, Recent developments in spectroscopic ellipsometry for in-situ applications, SPIE, 2001 (SPIE), 4449, p. 41-57.

[12] B. Johs, General virtual interface algorithm for in situ spectroscopic ellipsometric data analysis, Thin Solid Films 455-56 (2004) 632-638.

[13] J. A. Roth, W. S. Williamson, D. H. Chow, G. L. Olson, and B. Johs, Closed-loop control of resonant tunneling diode barrier thickness using in situ spectroscopic ellipsometry, Journal of Vacuum Science & Technology B 18 (2000) 1439-1442.

[14] D. Schneider and T. Schwarz, A photoacoustic method for characterising thin films, Surface & Coatings Technology 91 (1997) 136-146.

[15] D. Schneider, T. Schwarz, A. S. Bradford, Q. Shan, and R. J. Dewhurst, Controlling the quality of thin films by surface acoustic waves, Ultrasonics 35 (1997) 345-356.

[16] E. Louis, H. J. Voorma, N. B. Koster, L. Shmaenok, F. Bijkerk, R. Schlatmann, J. Verhoeven, Y. Y. Platonov, G. E. Vandorssen, and H. A. Padmore, Enhancement of Reflectivity of Multilayer Mirrors for Soft-X-Ray Projection Lithography by Temperature Optimization and Ion-Bombardment, Microelectronic Engineering 23 (1994) 215-218.

[17] K. Bergmann, O. Rosier, R. Lebert, W. Neff, and R. Poprawe, A multi-kilohertz pinch plasma radiation source for extreme ultraviolet lithography, Microelectronic Engineering 57-8 (2001) 71-77.

[18] J. Chen, C. J. Lee, E. Louis, F. Bijkerk, R. Kunze, H. Schmidt, D. Schneider, and R. Moors, Characterization of EUV induced carbon films using laser-generated surface acoustic waves, Diamond and Related Materials 18 (2009) 768-771.

[19] G. E. Jellison and F. A. Modine, Parameterization of the optical functions of amorphous materials in the interband region, Applied Physics Letters 69 (1996) 371-373.

[20] G. E. Jellison and F. A. Modine, Erratum: Parameterization of the optical functions of amorphous materials in the interband region, Applied Physics Letters 69 (1996) 2137-2137.

[21] J. Hong, A. Goullet, and G. Turban, Ellipsometry and Raman study on hydrogenated amorphous carbon (a-C : H) films deposited in a dual ECR-r.f. plasma, Thin Solid Films 352 (1999) 41-48.

[22] S. Logothetidis, M. Gioti, S. Lousinian, and S. Fotiadou, Haemocompatibility studies on carbon-based thin films by ellipsometry, Thin Solid Films 482 (2005) 126-132.

[23] J. Budai and Z. Toth, Optical phase diagram of amorphous carbon films determined by spectroscopic ellipsometry, phys. stat. sol. (c) 5 (2008) 1223-1226.

[24] M. Gioti and S. Logothetidis, Dielectric function, electronic properties and optical constants of amorphous carbon and carbon nitride films, Diamond and Related Materials 12 (2003) 957-962.

[25] J. Tauc, R. Grigorovici, and A. Vancu, Optical properties and electronic structure of amorphous germanium, Phys. Status Solidi 15 (1966) 627-637.

[26] C. Tanguy, Optical Dispersion by Wannier Excitons, Physical Review Letters 75 (1995) 4090-4093.

[27] C. Tanguy, Erratum: Optical dispersion by Wannier excitons (vol 75, pg 4090, 1995), Physical Review Letters 76 (1996) 716-716.

[28] C. Tanguy, Analytical expression of the complex dielectric function for the Hulthen potential, Physical Review B 60 (1999) 10660-10663.

[29] C. Tanguy, Refractive index of direct bandgap semiconductors near the absorption threshold: Influence of excitonic effects, Ieee Journal of Quantum Electronics 32 (1996) 1746-1751.

[30] H. J. Voorma, E. Louis, N. B. Koster, F. Bijkerk, and E. Spiller, Characterization of multilayers by Fourier analysis of x-ray reflectivity, Journal of Applied Physics 81 (1997) 6112-6119.

[31] S. Frank, B. Burkhard, G. Brandt, R. Fliegauf, K. Roman, M. Bernd, D. Rost, S. Detlef, M. Veldkamp, J. Weser, U. Gerhard, L. Eric, E. Y. Andrey, O. Sebastian, and B. Fred, New PTB beamlines for high-accuracy EUV reflectometry at BESSY II, SPIE, 2000 (SPIE), 4146, p. 72-82.

## 4    Secondary electron yield measurements of carbon covered multilayer optics

### 4.1    Abstract

Carbon contamination on extreme ultraviolet (EUV) optics has been observed in EUV lithography. In this paper, we performed *in situ* monitoring of the build-up and removal of carbon contamination on Mo/Si EUV multilayers by measuring the secondary electron yield as a function of primary electron energy. An electron beam with an energy of 2 keV was used to simulate the EUV radiation induced carbon contamination. For a clean EUV multilayer, the maximum secondary electron yield is about 1.5 electrons per primary electron at a primary electron energy of 467 eV. The maximum yield reduced to about 1.05 at a primary electron energy of 322 eV when the surface was covered by a non-uniform carbon layer with a maximum thickness of 7.7 nm. By analyzing the change in the maximum secondary electron yield with the final carbon layer thickness, the limit of detection was estimated to be less than 0.1 nm.

### 4.2    Introduction

Extreme ultraviolet lithography (EUVL) is a next generation lithography technique that uses 13.5 nm Extreme UV radiation. One critical aspect of EUV optics is carbon contamination because it can reduce the reflectance of Mo/Si multilayer mirrors (MLMs) [1-4]. Contamination monitoring and, later, cleaning is needed to maintain a high reflectance, requiring an *in situ* technique for monitoring the degree of contamination.

Several techniques have been shown to be sensitive to surface contamination. X-ray photoelectron spectroscopy (XPS) and Auger electron spectroscopy (AES) [1,5], as well as Auger depth profiling analysis [2,3] have been employed to measure the thickness or concentration of EUV induced carbon contamination films. However, these techniques lack sub-nanometer limits of detection and sensitivities, and require ultrahigh vacuum to operate. Finally, all of these techniques require substantial amounts of space within the vacuum chamber for the electron detector, which might be impractical in the final lithography application.

We investigated monitoring carbon contamination by laser-generated surface acoustic wave (LG-SAW) and spectroscopic ellipsometry [6,7]. It was found that ellipsometry has a better overall sensitivity, with a detection limit of 0.1 nm, while LG-SAW has an estimated detection limit of 1.2 nm. However, LG-SAW is difficult to implement on non-crystalline substrates, while spectroscopic ellipsometry instrumentation is relatively complex and expensive.

In this paper, we present an investigation of the feasibility of monitoring the carbon contamination by measuring the secondary electron yield (SEY), defined as the number of secondary electrons per incident primary electron. The experimental setup is

very simple compared to other surface sensitive techniques (e.g. various kinds of electron and photon spectroscopy).

Secondary electron (SE) emission is a phenomenon in which low energy electrons escape from a solid surface under bombardment with high energy primary electrons, ions, or photons [8]. We limit ourselves here to the influence of electron bombardment. When a primary electron impinges on a surface, it can either reflect elastically or inelastically. According to the energy loss process, the interactions between the primary electron and the material are mainly ionization, phonon and plasmon excitations, interband transitions, and free electron scattering. The electrons generated by these inelastic scattering processes are referred to as "true" secondary electrons.

Most secondary electrons have a very low kinetic energy of less than 50 eV and the peak of the energy distribution spectrum is located between 2 and 5 eV [8,9]. Due to their low energy, the SE escape depth is typically in the order of 3-5 nm in metals [10]. For a carbon film, the escape depth of SE was estimated to be about 3 nm [11]. This makes SEY a good candidate for detecting the formation of thin films.

The SE emission of different metals and its variation under surface treatments have been widely investigated (see e.g.,[9,10,12-14]). In addition, the SE emission of a capped Mo/Si multilayer during EUV radiation was also investigated [4]. However, to our knowledge, the SEY spectrum under electron radiation has not been measured, nor has its variation with carbon contamination and cleaning. We study the SE emission behavior of a MLM and use it as a parameter to monitor the carbon contamination and, later, atomic hydrogen cleaning.

### 4.3    Semi-empirical theory

The emission of secondary electron results from kinetic energy transfer of the primary electron to an electron in the lattice structure of a material. Therefore, the SEY is a function of the primary electron energy. The secondary electron emission process can be described in terms of two mechanisms: the production of SEs by inelastic scattering of the primary electrons, and their subsequent migration to the surface and escape into vacuum. Combining these two mechanisms, the SEY is given by:

$$\delta = \int_0^\infty nu(x, E_0) f(x) dx \tag{11}$$

where $nu(x, E_0) dx$ is the number of SE produced per incident primary electron of initial energy $E_0$ in a layer of thickness $dx$ at a depth $x$ below the surface. $f(x)$ is the probability that a secondary electron, produced at depth $x$, arrives at and escapes from the surface.

There are three main semi-empirical theories. Two of them, with an emphasis on metals, were developed by Lye and Dekker [15] and Dionne [16,17], respectively. Both theories are based on similar assumptions. However, one particular assumption: 'the constant-loss of the primary electron energy per unit depth' requires that the value for

the exponent '$n$' in equation (12) is changed in order to get the best fit. The third theory, which was developed by Cazaux, uses a more realistic account of the in-depth generation of the secondary electron [18]. Importantly, it has also been used for describing the SEY from graphite [19], which is very close to the phase of the carbon contamination found in our case. So we choose to use this theory for later analysis.

Cazaux's theory assumes uniform SE generation inside an irradiated spherical or ellipsoidal volume that is truncated by the surface of the sample. The center of this irradiated volume is located at the depth at which inelastic scattering is most probable, called the most probable energy dissipation depth, $z_C$. Its relative position is given by $k=z_C/R$, where $R$ (in nm) is the range (maximum penetration depth) of the primary electron:

$$R = CE_0^n \tag{12}$$

where $n$ is set to be 1.35, based on Young's electron transmission experiments on alumina films for the energy range of 0.3-7 keV [20]. $C = 115/\rho$ ($\rho$ is the mass density in g cm$^{-3}$) and $E_0$ is the primary electron energy in keV.

The migration of a SE towards the surface is described by an exponential attenuation function $exp(-z/s)$, where $s$ is the attenuation length of a SE and $z$ is the depth. Another parameter, $A$, describes the escape probability of SEs that reach the surface. The SEY, $\delta$, as a function of primary electron energy, $E_0$, is given by [18]:

$$\delta = \left[\frac{AE_0}{E_{se}}\right]\left[\frac{3}{2-3k}\right]\alpha^{-1}[D+F] \tag{13}$$

$$\alpha = R/s \tag{14}$$

$$D = 1 - 2k + 2k\alpha^{-1} - 2\alpha^{-2} \tag{15}$$

$$F = 2\alpha^{-1}(1-k+\alpha^{-1})e^{-\alpha} \tag{16}$$

where $E_{se}$ is the mean energy required to excite one SE inside the solid.

The 'universal' shape of the SEY spectra is determined by the SE escape depth and the average penetration depth of the primary electron in the material. As the primary electron energy increases, more SEs are generated and the average depth at which the SEs are generated also increases. As a result, the maximum yield in the SEY spectra is obtained when the primary electrons transfer the maximum amount of energy within the depth from which SEs have a high probability of escaping to the vacuum.

## 4.4　Methodology

### 4.4.1　SEY measurements

To measure the SEY, we use a technique similar to that originally proposed by Victor [21]. As shown in Fig. 21, there are three critical current parameters: the primary current, $I_P$, incident on the sample; the total scattered current, $I_S$, which is emitted from

the sample; and the target current, $I_T$, which exits the sample via a grounding wire. Thus, the SEY can be derived from the following equation:

$$\delta = \frac{I_S}{I_P} = 1 - \frac{I_T}{I_P} \tag{17}$$

From equation (17) it can be seen that it is only necessary to measure the primary current and either the target current or the total scattered current as a function of primary electron energy. Experimentally it is much more convenient to measure the target current. Here, we consider the primary current to be negative, therefore, if the SEY is larger than unity the target current is positive. Equation (17) indicates that the target current spectrum has the same shape with the SEY spectrum, provided that the primary electron current is constant as a function of primary electron energy.

The SEY, as described by equation (17), includes the contribution from backscattered electrons, including elastically and inelastically backscattered electrons. This is different from some definitions in the literature, where $I_S$ only refers to the current of "true" secondary electrons. "True" secondary electrons are often limited to those electrons that escape with an energy less than 50 eV. In addition, backscattered electrons also generate secondary electrons, thus, our measurements are the sum of the secondary electrons due to the primary electrons, secondary electrons due to backscattered electrons and backscattered electrons. To compare our results to those of others (see below), it is necessary to estimate the contribution of backscattered electrons to the total SEY.

The basic principle of electron backscattering from atoms and solids in the energy range 10 to 100 keV has been reviewed by H. Niedrig [22]. The backscattering coefficient is conventionally defined as the ratio of the number of the electrons that backscatter out of the sample surface with an energy greater than 50 eV, to the total number of the incident electrons. This has been measured for C, Al, Cu, Ag and Au in the electron energy range 0.6-6 keV [23]. The backscattering coefficient varies with primary electron energy and atomic number. Depending on the material, the contribution of backscattered electrons to the total SEY varies greatly. We estimate, based on the results presented in reference [23], that this contribution is approximately 0.3 and 0.1 of the total SEY for the MLM and the carbon contamination layer, respectively, at primary electron energy 1 keV.

A commercial electron gun (EFG-7/EGPS-2017 by Kimball Physics Inc.) was used as the electron source for both carbon deposition and SEY measurements. For both cases, the electron beam was at near normal incidence to the sample surface. To measure the SEY as function of the primary electron energy, the primary electron energy was swept between 110 and 1800 eV with the emission current fixed at 2 μA. During a sweep, the ratio of focus voltage and electron energy was fixed to 0.67 in order to have the smallest spot size (3 mm diameter) throughout the whole energy range. This ratio also provided the least variation in spot size over the whole energy range (~0.3

mm). Furthermore, the SEY measurement spot is about 0.5 mm larger in diameter than the focus of the electron beam during carbon deposition. Therefore, in every measurement, a part of the clean MLM contributed to the signal. However, if we assume the electron flux profile to have the same shape during deposition and measurement and we assume that this shape is represented by the profile of the deposited carbon (see Fig. 25), we calculated that 80 % of the observed SEY originates from the carbon contaminated area. This means that the uncontaminated part of the multilayer contributes only 20 % and it contributes an unchanging baseline signal that is naturally neglected when analyzing changes to the SEY spectrum.

A Faraday cup was used to determine the primary current as a function of primary electron energy. It was biased at +24 V in order to retrieve most of the emitted secondary electrons. The target current was measured by an electrometer (Keithley 2700). Fig. 21 shows the experimental configuration of the SEY measurements on a multilayer. Due to the good electrical conductivity of the MLMs with a metallic capping layer, charging effects can be neglected when determining the SEY.

## 4.4.2   Carbon contamination and cleaning

Electron irradiation in the presence of hydrocarbons was used to mimic the EUV induced chemistry [5,24] that results in the formation of a carbon film.

The main chamber for carbon deposition and the SEY measurements had a base pressure of $10^{-9}$ mbar. The residual gas analyzer (RGA) shows that the main residual gases were water, hydrogen and the hydrocarbons left over during carbon deposition. For carbon contamination deposition, the primary electron energy and an emission current were fixed at 2 keV [24] and 100 μA. The electron gun was set to focus the beam to approximately 2.5 mm in diameter. Fig. 22 shows a schematic view of the carbon deposition mechanism. Dodecane was admitted to the vacuum chamber as a precursor for the carbon deposition during electron bombardment. The electron-induced dissociation of a dodecane molecule resulted in carbon deposition [5,24]. The partial pressure of hydrocarbons during the deposition was controlled to be $1\times10^{-5}$ mbar. It took about 20 minutes for each carbon deposition.

In order to investigate the removal of the deposited carbon, the MLM was cleaned using atomic hydrogen. A load lock connected to the main chamber was equipped with an atomic hydrogen cleaning facility. Given the fact that the measurement spot is 0.5 mm larger than the carbon spot, the possible error in repositioning can be ignored. Atomic hydrogen was obtained from a thermal cracker whose mechanism has been investigated in the literature [25,26]. Briefly, the thermal cracker uses a tungsten wire, heated to about 2000 °C to thermally dissociate the hydrogen molecule, producing hydrogen radicals. These react with the carbon film, forming volatile hydrocarbons, the main product of which is a $CH_3$ radical [27]. During cleaning, a hydrogen gas flow of 3 sccm was used. The distance between the filament and sample was about 4 cm.

A typical MLM, consisting of 50 bi-layers of Mo and Si, each about 7 nm thick, with a protective metallic capping layer on top, was used as a substrate. The thickness of the full multilayer stack is 357 nm. A detailed description of the MLM fabrication and performance can be found elsewhere [28]. As a reference for the carbon contamination layer, the SEY spectrum of a graphite sample was also measured.
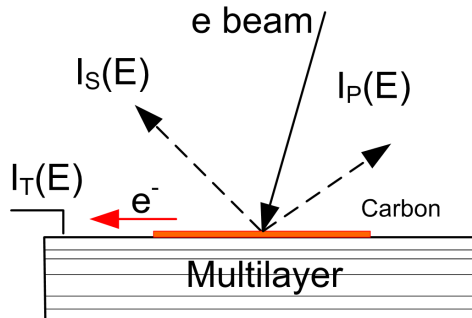


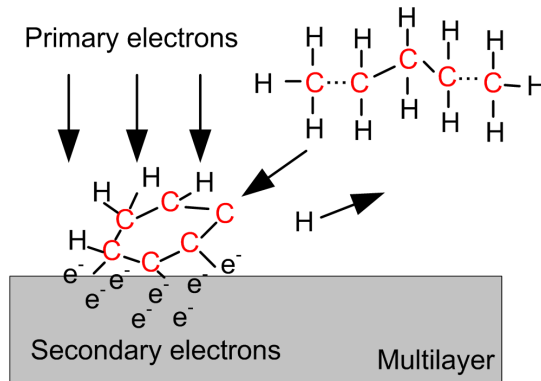*Fig. 21. Schematic view of the SEY measurements*



*Fig. 22. Schematic view of carbon deposition by electron bombardment in a hydrocarbon background*

## 4.5    Results

### 4.5.1    SEY of a MLM and graphite

To ensure that SEY measurements were accurate, we measured the primary electron current as a function of primary electron energy with an unbiased Faraday cup and with the Faraday cup biased at +24 V. The results are shown in Fig. 23. The emission current of the gun was kept constant at 2 μA over the whole energy range. The measured primary current increases by 70 nA when the Faraday cup is biased because the emitted

SEs are recaptured. When biased at +24 V, the primary current amplitude increases slowly with increasing energy till 200 eV and then remains constant at $589 \pm 5$ nA.

To investigate the influence on the SEY by a carbon layer on top of a MLM, the SEY of both a clean MLM and a graphite sample were measured as a start and end point of our carbon contamination experiments. To check that our SEY measurements were reliable, the spectra were also fit to the theory, as shown in Fig. 24, and, where possible, compared to literature results. As shown in Table 1, the maximum SEY of a MLM is 1.5 at a primary electron energy of 467 eV. This is in the range of the SEY of metallic materials, which are reported to vary from 0.6 to 1.7 [9,29]. There are also two primary energies for which $\delta = 1$, which occur for $I_T = 0$, denoted as the first (low energy) and second (high energy) crossover energies $E_1$ and $E_2$. The first and second cross-over energies are 152 and 1984 eV, respectively, for a MLM.

For graphite the maximum SEY is only about 0.8 at a primary electron energy of 290 eV and, notably, there are no crossover energies, because the SEY is less than 1 over the whole range.

From a fit of our SEY results by Cazaux's equations (12)-(16), we retrieved the parameters $k$, $s$ and $A/E_{se}$. We considered our MLM to be a single material system with a density which is the average of Mo and Si layers, each of them taken to be 85% of the bulk values [30]. This effective medium assumption is justified by the good agreement between the experimental data and the theoretical fit, which also includes the fact that the top layer is the main contributor to the SEY signal. Table 1 shows the values of $k$, $s$ and $A/E_{se}$ that fit the experimental spectrum measured for a MLM and graphite. For these samples, $\delta_{max}$ and its corresponding energy, $E_{0max}$, were also calculated. In addition, literature values for graphite are shown for comparison [13,19,31]. Our results, e.g. $\delta_{max}$, are comparable to the literature values, but an exact comparison can not be made because of the spread of the literature values.

Table 1 shows that the SE attenuation length of graphite, $s$, is about twice as long as that of the MLM. Similarly, the relative position, $k$, of the most probable energy dissipation is approximately twice that of the MLM. The difference in the values of $A/E_{se}$, between the MLM and graphite sample is about 20% and has only a minor effect on the SEY. However, the most important parameter influencing the SEY is the range of the primary electron, which is determined by the density through equation (12). The density of the MLM is about 2.5 times greater than that of graphite. The combination of the effects of the density, $k$, and $A/E_{se}$, give MLMs a higher SEY than graphite, despite the longer attenuation length of graphite acting to increase the SEY of graphite. As a result, the SEY of a MLM is about twice that of graphite over the entire primary electron energy range. In addition, the three parameters, $k$, $s$ and $A/E_{se}$ of our graphite sample are comparable with that published in the literature [19].

As stated above, the SEY spectrum of a MLM can be described by an effective bulk material, despite its heterogeneous nature. However, as shown below, we have

found that the shape of the SEY spectrum changes dramatically when carbon is deposited on the MLM surface. In this case we were unable to fit the spectrum assuming a single effective bulk medium. Note, from Table 1, that the density, the SE attenuation length, and other parameters, differ for a MLM and graphite. This contrast, along with the non-uniformity of the carbon layer, precludes fitting the data with a single set of material parameters. However, developing a SEY theory for heterogeneous materials was beyond the scope of this paper.
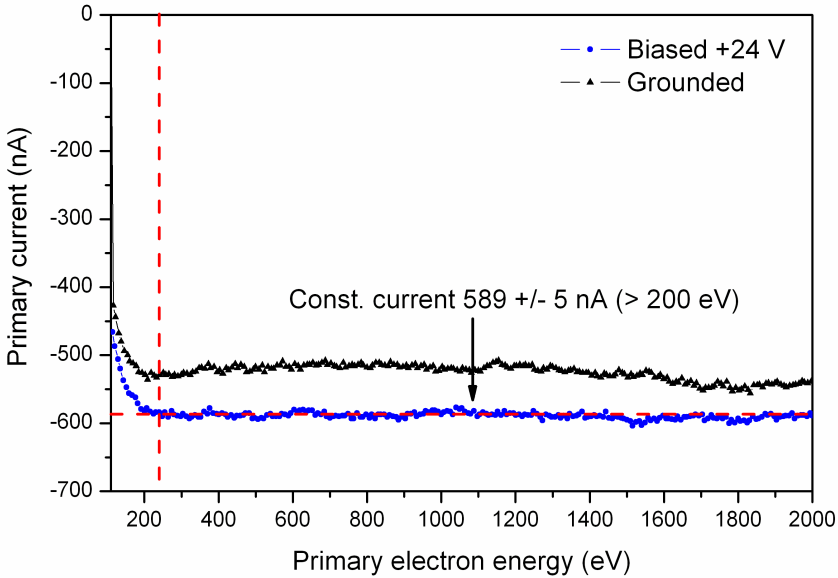


Fig. 23. Primary current versus primary electron energy measured by a Faraday cup, biased at +24 V (circles) and unbiased (triangles). The primary current is constant at 589±5 nA for primary electron energies larger than 200 eV.
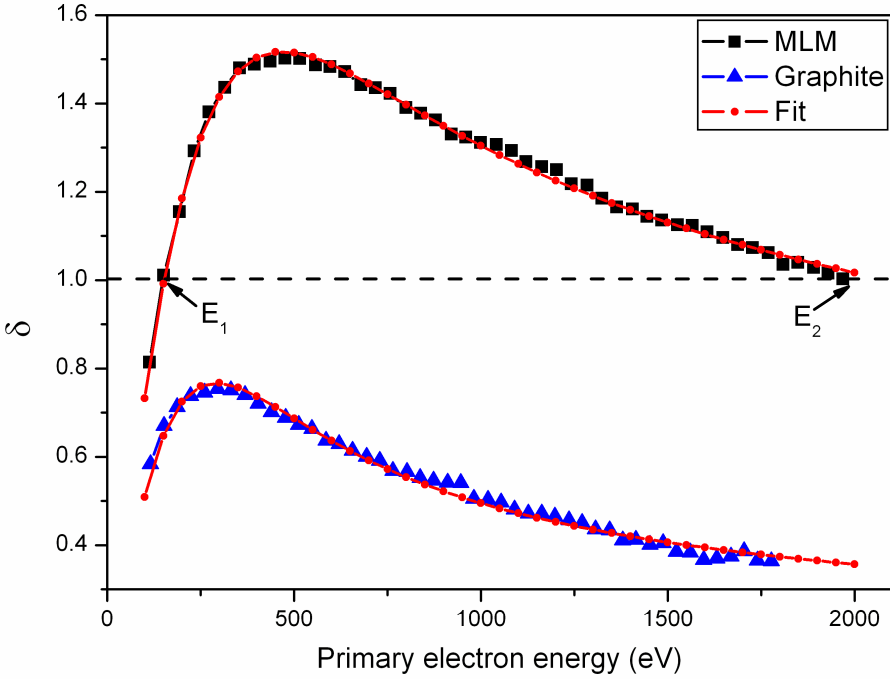
*Fig. 24. The experimental SEY spectrum of a MLM (squares) and graphite (triangles). Both are fitted with Cazaux's theory (dot line).*

*Table 1. Values of parameters ρ, k, $E_{0max}$, $\delta_{max}$, s and $A/E_{se}$ for a MLM and graphite. The parameter values of graphite from the literature are also listed as a comparison.*

| | $\rho$ (g cm$^{-3}$) | $k$ | $E_{0max}$ (eV) | $\delta_{max}$ | $s$ (nm) | $A/E_{se}$ (keV$^{-1}$) |
|---|---|---|---|---|---|---|
| MLM | 5.4 | 0.19 | 467 | 1.5 | 2.45 | 8.49 |
| Graphite | ~2.2[a] | 0.37 | 290 | 0.8 | 3.91 | 6.50 |
| Graphite[b] | 2.3 | ~0.4 | 325 | 1.2 | 4.6 | 9 |
| Graphite[c] | - | - | 300-350 | 0.85-1.2 | - | - |

[a] from [32]
[b] from [19]
[c] from [13]

### 4.5.2    **Carbon contamination and cleaning monitoring**

Carbon contamination and atomic hydrogen cleaning were monitored by measuring the SEY as a function of primary electron energy. We performed two cycles of carbon deposition. The first consisted of 8 deposition steps, each lasting 10 or 20 minutes, while the second consisted of 5 deposition steps, lasting 20 minutes each. Between the two deposition cycles, the MLM was cleaned with atomic hydrogen in 9 steps of several minutes each.

According to the optical constants *n* and *k*, measured over the range of 245 to 1000 nm, using spectroscopic ellipsometry, the carbon contamination layer (see Fig. 25) deposited by electron bombardment is graphite-like. Therefore, we expect that as the layer thickness increases, the SEY spectrum should tend towards that of the graphite sample.

Fig. 25 shows the carbon layer thickness profile after the second carbon deposition cycle was completed. It is a non-uniform carbon layer with a diameter of about 2.5 mm. The maximum thickness is 7.7 nm and located in the center, while the average thickness within the measurement spot is 1.2 nm.

Fig. 26 shows an overview of target current versus primary electron energy curves for both carbon deposition and hydrogen cleaning cycles. It can be seen that deposition of a carbon layer causes a reduction of the target current for the entire primary electron energy range, while the removal of the carbon layer results in an increasing target current. After depositing a carbon spot with maximum thickness of 7.7 nm the maximum yield is reduced to about 1.05 and its corresponding primary energy shifted to 322 eV. This is shown in Fig. 27 (a)-(c). We also estimated from Fig. 26 that $E_1$ would be relatively insensitive to carbon deposition and it was therefore not included in the analysis. From Fig. 26, the variation of the maximum SEY, $\delta_{max}$, its corresponding energy, $E_{0max}$ and the second cross over energy, $E_2$ with increasing carbon deposition time (i.e. electron radiation time) are obtained (see Fig. 27 (a)-(c)). The parameters $\delta_{max}$ and $E_2$ decrease with increasing carbon layer thickness. Similar phenomena have also been observed by other authors [9]. This is because, for graphite, the SEY is two times lower than the SEY from a MLM and there is no $E_2$. In addition, the backscattering coefficient of graphite is about three times lower than that of the MLM [23]. This reduces the contribution of secondary electrons that are generated by backscattered electrons as well as the number of backscattered electrons.

However, $E_{0max}$ does not decrease monotonically. It shifts to a higher energy first then returns to a lower energy. We explain this as follows: when the carbon layer is very thin, the SE production in the carbon layer can be neglected, however, the primary electron energy of the electrons reaching the MLM decreases due to the energy loss in the carbon layer. Consequently, $E_{0max}$ increases slightly. Meanwhile, some of the SEs generated in the MLM are absorbed in the carbon layer decreasing the SEY. As the thickness of the carbon layer increases, SE production in the carbon layer becomes

significant. The total SEY is a combination of the SEY of the surface carbon layer and the electrons emitted by the underlying MLM. Due to the fact that $E_{0max}$ of bulk graphite is around 290 eV (177 eV less than that of a MLM), $E_{0max}$ reduces and then saturates at around 290 eV when the carbon layer is sufficiently thick.

The sensitivities of $\delta_{max}$, $E_{0max}$, and $E_2$ (see Table 2) were estimated by dividing the respective parameter change by the carbon thickness. The resulting limits of detection were calculated by multiplying the sensitivity and the uncertainty of the parameter. The maximum and average thickness in the measurement spot after the second cycle of carbon deposition were used. Note that the overall changes of the three parameters between after hydrogen cleaning and after the second cycle of carbon deposition were considered for the calculation of sensitivity and detection limit. The sensitivity of $\delta_{max}$, $E_{0max}$ and $E_2$ are 0.33 nm$^{-1}$, 133 eV nm$^{-1}$ and 724 eV nm$^{-1}$, respectively, for an average thickness of 1.2 nm. The calculated sensitivities, based on a model (discussed in Section 4.5.3 in detail), were also listed. It is observed that these calculated sensitivities for $\delta_{max}$ and $E_2$ are comparable to the ones calculated from the experimental data. Furthermore, $\delta_{max}$ was estimated to have the lowest detection limit of 0.02-0.1 nm, using the final maximum and average thickness over the spot. The limits of detection of $E_{0max}$ and $E_2$ are larger at 0.6 and 0.2 nm, respectively, according to the maximum thickness.

A similar SEY measurement was performed after each atomic hydrogen cleaning step. Fig. 27 (d-f) shows the variation of $\delta_{max}$, $E_{0max}$, and $E_2$ with increasing cleaning time. A roughly reverse behavior was observed for these three parameters. However, the recovery of the parameters $\delta_{max}$ and $E_2$ were faster in the beginning of the cleaning. This is due to the fact that the atomic hydrogen removes the carbon surface evenly while the deposition is spatially non-uniform, as shown in Fig. 25. This results in the exposure of larger area of clean MLM at the beginning of cleaning process. Finally, all three parameters returned to within 7% of their original values, i.e. when the MLM was clean.

After atomic hydrogen cleaning, it is observed from Fig. 26 that the SEY was not as high as before carbon deposition. The maximum temperature during several minutes of cleaning is about 50 °C and our multilayer structure is stable at that temperature [33]. Therefore, we believe that this is due to physical and/or chemical changes of the surface, which could be due to the formation of carbides and/or oxides with the original metallic capping layer. It might also be due to the hydrogen cleaning inducing surface contamination or roughening the surface [29]. Investigation of the cause of this difference is beyond the scope of this paper.
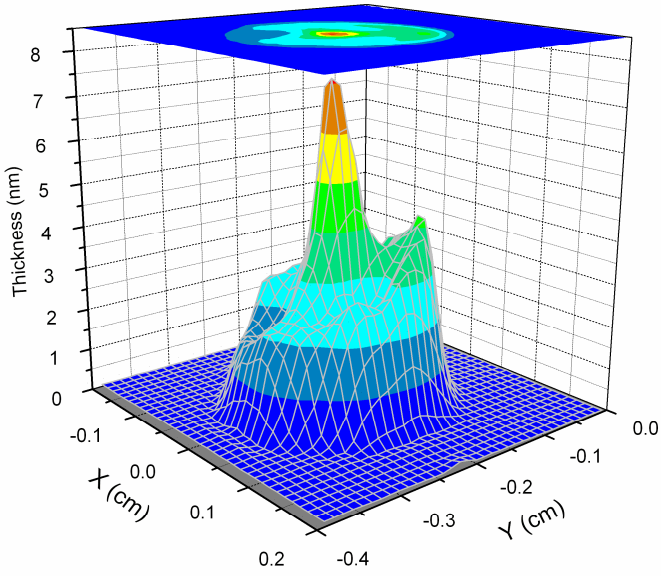
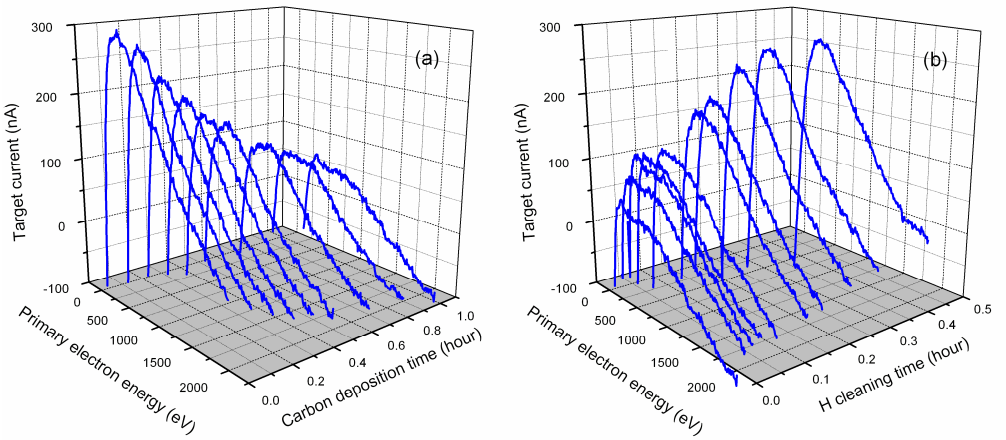*Fig. 25. Carbon thickness spatial profile after carbon deposition, measured by spectroscopic ellipsometry*



*Fig. 26. Overview of target current versus primary electron energy of carbon depositions (a) on a MLM and atomic hydrogen cleanings (b).*
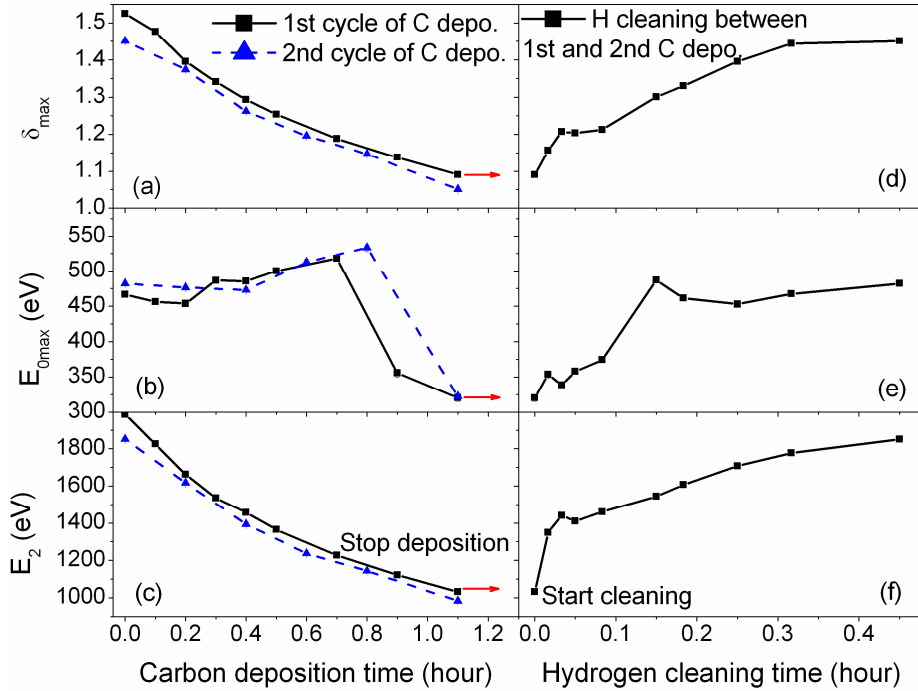
*Fig. 27. $\delta_{max}$, $E_{0max}$, $E_2$ versus carbon deposition time (a-c), and atomic hydrogen cleaning time (d-f). The squares and triangles in (a-c) correspond to the first and the second cycle of carbon deposition, respectively.*

*Table 2. Estimated sensitivity and detection limit for $\delta_{max}$, $E_{0max}$ and $E_2$*

|  | Sensitivity | | | Detection limit (nm) | |
|---|---|---|---|---|---|
| $\delta_{max}$ | 0.05 nm$^{-1}$ [a] | 0.33 nm$^{-1}$ [b] | 0.31 nm$^{-1}$ [c] | 0.1[a] | 0.02[b] |
| $E_{0max}$ | 21 eV nm$^{-1}$ [a] | 133 eV nm$^{-1}$ [b] | 10 eV nm$^{-1}$ [c] | 0.6[a] | 0.10[b] |
| $E_2$ | 113 eV nm$^{-1}$ [a] | 724 eV nm$^{-1}$ [b] | 909 eV nm$^{-1}$ [c] | 0.2[a] | 0.03[b] |

[a] based on the maximum carbon thickness 7.7 nm

[b] based on the average carbon thickness 1.2 nm

[c] based on the model in section 4.5.3

### 4.5.3    A model for extracting the thickness

To extract the thickness of the carbon layer deposited from the change of the three parameters $\delta_{\max}$, $E_{0max}$, and $E_2$ (as shown in Fig. 27), we developed a simple model based on equations (12)-(16) describing the SEY of a carbon layer on top of a MLM. Several modifications are introduced. First, we take into account the energy loss of the primary electron passing the carbon layer on its way to the MLM. A constant energy loss described by $dE/dx=-E_0/R$ [16] was used in which $E_0$ is the primary electron energy and $R$ is the range of the primary electron. Secondly, we take into account the absorption of secondary electrons, generated in the MLM, by the carbon layer. This is described by the factor $exp(-d/s)$, for which $s$ is the attenuation length of the SE and $d$ is the carbon layer thickness. Finally, we have included the generation of SE in the carbon layer itself by a linear approximation $\dfrac{d}{R}\delta(graphite)$, in which $\delta(graphite)$ is the SEY of the graphite sample. Fig. 28 shows the calculated SEY spectrum of a MLM covered by a 1 nm thin layer of uniform carbon. The SEY of a MLM is also plotted as a reference. Fig. 29 shows the calculated changes of $\delta_{\max}$, $E_{0max}$, and $E_2$ as a function of the carbon layer thickness. These three parameters will start to saturate after the carbon layer thickness becomes comparable to the attenuation length (3.91 nm) of SE in the carbon. This indicates the upper detection limit of this technique. As a comparison, the values of the three parameters and the average carbon layer thickness after the second cycle of carbon deposition are also plotted. It is observed that only $E_2$ and $\delta_{\max}$ are close to the calculated trend. However, there is a large difference for $E_{0max}$ between the calculated and experimental data. This we ascribe to the fact that the thickness of the carbon layer deposited is laterally non-uniform, with the maximum thickness 7.7 nm (see Fig. 25). In addition, the SE emission behavior difference between a bulk graphite sample and the carbon layer deposited could also contribute to the difference.
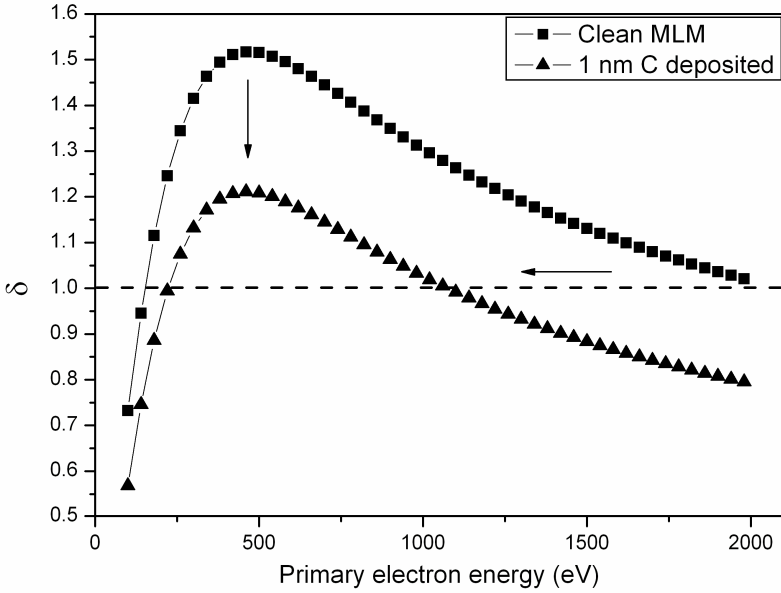
*Fig. 28. The calculated SEY spectrum of a MLM covered by 1 nm of carbon (black triangle) and the SEY of a clean MLM as a reference (black square), as resulting from our model and Cazaux's theory.*
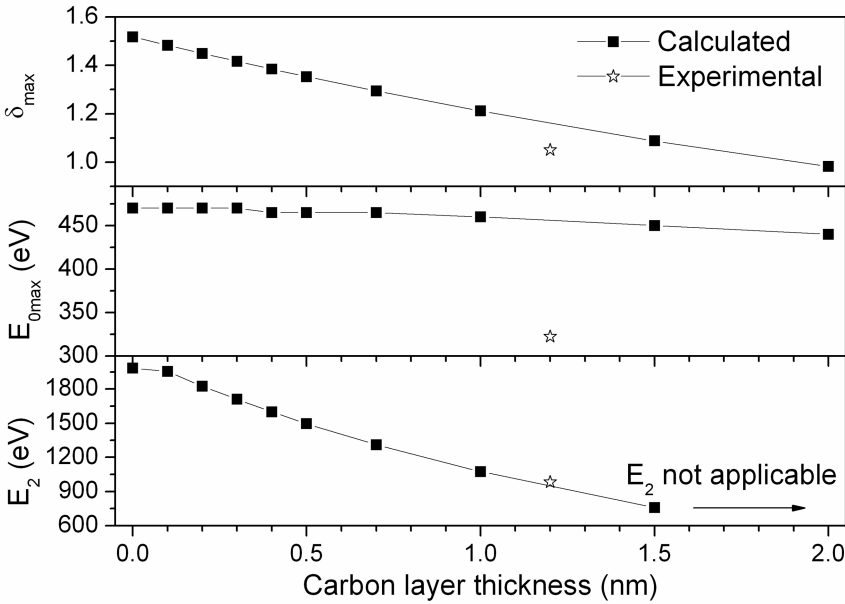


*Fig. 29. Calculated $\delta_{max}$, $E_{0max}$, $E_2$ versus carbon layer thickness (squares). The final values of the three parameters and the corresponding average carbon thickness are also plotted for* comparison (stars).

### *4.6    Conclusion*

We monitored the carbon contamination on an EUV reflecting multilayer structure by measuring the secondary electron yield *in situ* as a function of the energy of the incident primary electrons. The carbon contamination was induced by electron irradiation of the multilayer in a hydrocarbon background. For a clean multilayer, the maximum SEY is about 1.5 secondary electrons per primary electron at an energy of 467 eV. However, the SEY decreases over the whole energy range when the surface is carbon contaminated. The final carbon thickness profile was measured by spectroscopic ellipsometry. As a result of the carbon contamination, the maximum yield reduced from 1.5 to about 1.05 and its corresponding primary energy shifted from 467 eV to 322 eV when a non-uniform carbon layer with a maximum thickness of 7.7 nm in the center was deposited on the surface. We measured three parameters while monitoring the carbon deposition with time: the maximum SEY, $\delta_{max}$, its corresponding energy, $E_{0max}$, and the secondary crossover energy, $E_2$, of the SEY spectra. $\delta_{max}$ is estimated to have the lowest detection limit of between 0.1 nm and 0.02 nm, depending on the final maximum and average thickness within the SEY measurement spot.

Atomic hydrogen cleaning was used to remove the carbon contamination. The removal process was also monitored by measuring the SEY. The SEY spectrum was observed to return to approximately its original form when the MLM was fully cleaned, illustrating the suitability of the SEY measurements for both the contamination and cleaning process.

We developed a simple model to retrieve the thickness evolution during growth as well as removal of the carbon overlayer using the experimental behavior of $\delta_{max}$, $E_{0max}$, and $E_2$.

Different material and/or surface conditions have different SEY characteristics. During our experiments, the overall variation of the behavior of the SEY spectra fits well to that expected by the deposition of a pure carbon layer. This indicates that a careful analysis of the SEY spectra may also be used to reveal the constituents of a contamination layer.

### *4.7    Acknowledgements*

### *4.8    Reference*

[1]  S. Matsunari, T. Aoki, K. Murakami, Y. Gomei, S. Terashima, H. Takase, M. Tanabe, Y. Watanabe, Y. Kakutani, M. Niibe, and Y. Fukuda, Carbon deposition on multi-layer mirrors by extreme ultra violet ray irradiation, SPIE, San Jose, CA, USA, 2007 (SPIE), 6517, p. 65172X-8.

[2]  J. Hollenshead and L. Klebanoff, Modeling radiation-induced carbon contamination of extreme ultraviolet optics, Journal of Vacuum Science & Technology B 24 (2006) 64-82.

[3]  N. Koster, B. Mertens, R. Jansen, A. van de Runstraat, F. Stietz, M. Wedowski, H. Meiling, R. Klein, A. Gottwald, F. Scholze, M. Visser, R. Kurt, P. Zalm, E. Louis, and A. Yakshin, Molecular contamination mitigation in EUVL by environmental control, Microelectronic Engineering 61-2 (2002) 65-76.

[4]  T. E. Madey, N. S. Faradzhev, B. V. Yakshinskiy, and N. V. Edwards, Surface phenomena related to mirror degradation in extreme ultraviolet (EUV) lithography, Applied Surface Science 253 (2006) 1691-1708.

[5]  G. Kyriakou, D. J. Davis, R. B. Grant, D. J. Watson, A. Keen, M. S. Tikhov, and R. M. Lambert, Electron impact-assisted carbon film growth on Ru(0001): Implications for next-generation EUV lithography, Journal of Physical Chemistry C 111 (2007) 4491-4494.

[6]  J. Q. Chen, E. Louis, C. J. Lee, H. Wormeester, R. Kunze, H. Schmidt, D. Schneider, R. Moors, W. van Schaik, M. Lubomska, and F. Bijkerk, Detection and characterization of carbon contamination on EUV multilayer mirrors, Optics Express 17 (2009) 16969-16979.

[7]  J. Q. Chen, C. J. Lee, E. Louis, F. Bijkerk, R. Kunze, H. Schmidt, D. Schneider, and R. Moors, Characterization of EUV induced carbon films using laser-generated surface acoustic waves, Diamond and Related Materials 18 (2009) 768-771.

[8]  J. J. Scholtz, D. Dijkkamp, and R. W. A. Schmitz, Secondary electron emission properties, Philips Journal of Research 50 (1996) 375-389.

[9]  H. Seiler, Secondary electron emission in the scanning electron microscope, Journal of Applied Physics 54 (1983) R1-R18.

[10] N. Hilleret, C. Scheuerlein, and M. Taborelli, The secondary-electron yield of air-exposed metal surfaces, Applied Physics a-Materials Science & Processing 76 (2003) 1085-1091.

[11] D. Voreades, Secondary electron emission from thin carbon films, Surface Science 60 (1976) 325-348.

[12] V. Baglin, J. Bojko, O. Groner, B. Henrist, N. Hilleret, C. Scheuerlein, and M. Taborelli, The secondary electron yield of technical materials and its variation with surface treatments, European Particle Accelerator Conference (EPAC), Vienna, Austria, 2000, 217-221.

[13] D. C. Joy, A  database of electron-solid interactions (available at http://web.utk.edu/~srcutk/htm/interact.htm), 2008

[14] J. Cazaux, Secondary electron emission and charging mechanisms in Auger Electron Spectroscopy and related e-beam techniques, Journal of Electron Spectroscopy and Related Phenomena 176 (2010) 58-79.

[15] R. G. Lye and A. J. Dekker, Theory of Secondary Emission, Physical Review 107 (1957) 977.

[16] G. Dionne, Effects of secondary electron scattering on secondary emission yield curves, Journal of Applied Physics 44 (1973) 5361-5364.

[17] G. Dionne, Origin of secondary-electron-emission yield-curve parameters, Journal of Applied Physics 46 (1975) 3347-3351.

[18] J. Cazaux, A new model of dependence of secondary electron emission yield on primary electron energy for application to polymers, Journal of Physics D-Applied Physics 38 (2005) 2433-2441.

[19] J. Cazaux, Secondary electron emission yield: graphite and some aromatic hydrocarbons, Journal of Physics D-Applied Physics 38 (2005) 2442-2445.

[20] J. R. Young, Penetration of Electrons in Aluminum Oxide Films, Physical Review 103 (1956) 292.

[21] E. H. Victor, Fast, Accurate Secondary-Electron Yield Measurements at Low Primary Energies, Review of Scientific Instruments 44 (1973) 456-462.

[22] H. Niedrig, Electron backscattering from thin films, Journal of Applied Physics 53 (1982) R15-R49.

[23] A. M. D. Assa'd and M. M. El Gomati, Backscattering coefficients for low energy electrons, Scanning Microscopy 12 (1998) 185-192.

[24] B. Mertens, M. Weiss, H. Meiling, R. Klein, E. Louis, R. Kurt, M. Wedowski, H. Trenkler, B. Wolschrijn, R. Jansen, A. van de Runstraat, R. Moors, K. Spee, S. Ploger, and R. van de Kruijs, Progress in EUV optics lifetime expectations, Microelectronic Engineering 73-74 (2004) 16-22.

[25] Samuel Graham, Jr., A. S. Charles, W. M. Clift, E. K. Leonard, and B. Sasa, Atomic hydrogen cleaning of EUV multilayer optics, SPIE, 2003 (SPIE), 5037, p. 460-469.

[26] K. Motai, H. Oizumi, S. Miyagaki, I. Nishiyama, A. Izumi, T. Ueno, and A. Namiki, Cleaning technology for EUV multilayer mirror using atomic hydrogen generated with hot wire, Thin Solid Films 516 (2008) 839-843.

[27] E. Vietzke, V. Philipps, K. Flaskamp, P. Koidl, and C. Wild, The Reaction of Atomic-Hydrogen with a-C-H and Diamond Films, Surface & Coatings Technology 47 (1991) 156-161.

[28] E. Louis, H. J. Voorma, N. B. Koster, L. Shmaenok, F. Bijkerk, R. Schlatmann, J. Verhoeven, Y. Y. Platonov, G. E. Vandorssen, and H. A. Padmore, Enhancement of Reflectivity of Multilayer Mirrors for Soft-X-Ray Projection Lithography by Temperature Optimization and Ion-Bombardment, Microelectronic Engineering 23 (1994) 215-218.

[29] H. Bruining, Physics and applications of secondary electron emission, Pergamon Press London, 1954.

[30] H. J. Voorma, E. Louis, N. B. Koster, F. Bijkerk, and E. Spiller, Characterization of multilayers by Fourier analysis of x-ray reflectivity, Journal of Applied Physics 81 (1997) 6112-6119.

[31] I. Richterov, D. Fujita, Z. Nemecek, M. Beranek, and J. Safrankova, Secondary electron yield of glassy carbon dust grains, 17th Annual Conference of Doctoral Students - WDS 2008, Prague, 2008, Proceedings of Contributed Papers, Part II, p. 68-73.

[32] *Handbook of Chemistry and Physics 64th edition*; *Vol.*, edited by R. C. Weast (1983-1984).

[33] S. Bruijn, R. W. E. van de Kruijs, A. E. Yakshin, and F. Bijkerk, In-situ study of the diffusion-reaction mechanism in Mo/Si multilayered films, Applied Surface Science 257 (2011) 2707-2711.

## 5  Carbon induced EUV reflectance loss characterized using visible-light ellipsometry

### 5.1  Abstract

Carbon deposition on extreme ultraviolet (EUV) optics was observed due to photon induced dissociation of hydrocarbons in a EUV lithography environment. The reflectance loss of the multilayer mirror is determined by the carbon layer thickness and density. To study the influence of various forms of carbon, EUV induced carbon, hot filament, and e-beam evaporated carbon, were deposited on EUV multilayer mirrors. Spectroscopic ellipsometry was used to determine the carbon layer thickness and the optical constants ranging from ultraviolet to near infrared. The carbon density (and thus reflectance loss) was determined from the optical constants using both Bruggeman's effective medium approximation (BEMA), and the Clausius-Mosotti (CM) equation. Both approaches result in a similar EUV reflectance loss, with an accuracy of about 4%. The application of this process to ultrathin carbon films is further discussed.

### 5.2  Introduction

Extreme ultraviolet lithography (EUVL) is a next generation lithographic technique that uses 13.5 nm or Extreme UV radiation. The reflectance of each lithography optical element at this EUV wavelength is one of the most important parameters that influence the throughput of the lithographic equipment. Carbon contamination is one of the main surface contamination processes that reduces the reflectance of the Mo/Si multilayer mirrors (MLMs) used [1]. One of the challenges in developing EUVL is the development of effective and rapid cleaning techniques.

Different types of carbon contamination under photon radiation, i.e. graphite or polymer like, have been observed [1-3]. The specific type of carbon contamination expected in the EUVL environment can be influenced by several factors, including residual background gas, radiation flux, geometry of illumination, and the temperature of the optics. Determining of the type of the carbon contamination is important both for the cleaning procedure and the induced reflectance loss.

Calculations show that 2 nm of carbon in the form of graphite (density 2.25 g/cm$^3$) would reduce the relative reflectance loss of an MLM by 5%. On the other hand, as an example, as described by Hollenshead and Klebanoff [1], the projection optics of EUVL equipment should not lose more than 1.6% reflectance per optic. This means we have to deal with ultrathin carbon films of less than 10 nm in EUVL applications.

Due to a lack of space, using a reflectometer in the EUV lithography environment to measure the reflectance loss directly is very difficult. Therefore, an alternative technique for monitoring the contamination is required to enable *in situ* reflectance loss estimation. To estimate the reflectance loss of each multilayer mirror, both the carbon layer thickness and density are needed. Spectroscopic ellipsometry (SE) is one of the

best candidates for *in situ* monitoring of carbon deposition [4]. SE has a detection limit of about 0.1 nm.

The carbon densities are usually determined using electron energy loss spectroscopy (EELS) [5,6], a combination of ellipsometry with nuclear reaction analysis (NRA) [7,8], proton-enhanced cross-section scattering (PES) [9], or Rutherford backscattering (RBS) [10]. All of these techniques require substantial amounts of space within the vacuum chamber, making them undesirable for EUVL.

In this paper, we estimate the carbon density from the optical constants in the wavelength range of ultraviolet (UV) to near infrared (NIR) using two approaches: Bruggeman's effective medium approximation (BEMA) and the Clausius-Mosotti (CM) equation. We show the applicability of SE by investigating the reflectance loss of MLMs after the deposition of different kinds of carbon films. The EUV reflectance loss was estimated from the carbon density and thickness, as derived from SE measurements.

These estimates were compared with the measured EUV reflectance loss. Good agreement was obtained between the measured and the estimated reflectance loss. This work establishes spectroscopic ellipsometry as an excellent technique for *in situ* monitoring carbon contamination of MLMs in EUVL. The applicability for ultrathin carbon films, in which case the individual determination of the refractive index and the thickness is very difficult will be discussed.

### 5.3    Methodology

Briefly, the MLMs investigated consist of 50 bi-layers of Mo and Si, each about 7 nm thick, deposited on the (001) surface of a Si wafer. Each MLM has a capping layer terminating the structure. A complete description of a typical MLM structure and its properties can be found elsewhere [11].

Three types of carbon layers have been investigated. The first type, called "EUV induced C", was grown by exposing the MLM to EUV radiation in the presence of residual hydrocarbon gases. Four different thicknesses were obtained by varying the number of pulses of EUV light. The second type of carbon layer, referred to as "hot filament C", was deposited by evaporation from a graphite filament. The third type of carbon layer was deposited using physical vapor deposition (PVD) after e-beam evaporation of a graphite target. This layer is referred to as "PVD C".

The optical characterization of the EUV induced carbon and hot filament carbon was done *ex situ* using variable angle spectroscopic ellipsometry (Woollam, VASE, spectral range 245-1689 nm). The PVD carbon deposition was monitored with *in situ* ellipsometry (Woollam, M2000, incidence angle of 55° with respect to the surface normal). Standard procedures for data analysis and deducing the thickness and optical constants of the carbon films were used [12,13].

To establish the carbon density, a set of carbon films were deposited on a silicon wafer and analyzed with grazing incidence X-ray reflectivity (GIXR) [14]. An e*x situ*

reflectometer, based on $\lambda = 0.154$ nm (Cu-$K_\alpha$) was used. The critical angle for total external reflection was used to determine the total electron density, which provides the mass density. Furthermore, the thickness of the top carbon layer is determined by fitting the period of the interference pattern.

The EUV reflectance for these carbon covered MLMs was measured with a reflectometer at the radiometry laboratory of the Physikalisch-Technische Bundesanstalt (PTB) at the BESSY II electron storage ring. The estimated reflectance of a carbon covered MLM was calculated using the IMD program [15].

### 5.4    Principle of EUV reflectance loss

The refractive index (and thus the dielectric function) at EUV wavelength and soft X-rays can be described by [16]:

$$n(\lambda) = 1 - \delta + i\beta \tag{18}$$

where

$$\delta = \frac{n_a r_e \lambda^2}{2\pi} f_1^0(\lambda) \text{ and } \beta = \frac{n_a r_e \lambda^2}{2\pi} f_2^0(\lambda)$$

where $n_a$ is the atomic density, $r_e$ is the classical electron radius and $\lambda$ is the radiation wavelength. $f_1^0(\lambda)$ and $f_2^0(\lambda)$ are the atomic scattering factors as a function of wavelength. The atomic scattering factors of carbon and hydrogen from the reference [16] were used in our calculations.

Equation (18) shows that the refractive index for EUV and soft X-rays of different kinds of carbon films is determined only by the atomic density. In other words, the carbon atoms in solids react to the incident EUV radiation as if they are isolated atoms. The specific carbon bonds present (i.e. $sp^1$, $sp^2$ and $sp^3$) or the band structure of the different kinds of carbon films does not affect the absorption process of the incident radiation. Furthermore, the accuracy of equation (18) has been verified for polymer films [17].

The refractive indexes at the EUV wavelength of 13.5 nm for diamond (density 3.51 g/cm$^3$), graphite (density 2.25 g/cm$^3$) and polyethylene (density 0.90 g/cm$^3$) were computed with IMD. The geometry considered was a carbon layer on top of an MLM at an angle of incidence of 1.5° with respect to the surface normal.

The relative EUV reflectance loss, $\Delta R / R$, is

$$\Delta R / R = \frac{R - R_0}{R_0} \times 100\% \tag{19}$$

where $R_0$ is the original EUV reflectance of an MLM and $R$ is the reflectance upon carbon deposition. Fig. 30(a) shows the calculated relative EUV reflectance loss, $\Delta R / R$, as a function of carbon layer thickness for the three types of carbon films. The general trend is that the EUV reflectance decreases with increasing carbon layer thickness. The influence of the carbon density on the EUV reflectance loss is strong. For

instance, the relative reflectance loss due to a 2 nm thick layer of diamond (7.6%) is 3.8 times higher than that of the same thickness of polyethylene. The oscillations of the curves are due to the interference between the carbon surface and the interface between the carbon layer and the MLM. The oscillation amplitude is determined by the optical contrast between the carbon layer and the substrate underneath.

Fig. 30(b) shows the relative reflectance loss normalized by the carbon density. The different types of carbon films can be seen to give nearly the same reflectance loss level per unit density. This shows that the reflectance attenuation scales with the density and multiple interferences between the surface and interface have only a minor effect. Especially, for a carbon layer less than 4 nm thick, corresponding to a practical case in EUVL applications, the relative reflectance loss curve can be simplified to a linear relationship as:

$$\Delta R / R \approx k\rho d \tag{20}$$

where k is a constant equals to the slope as indicated in Fig. 30(b), $\rho$ is the average mass density and $d$ is the carbon layer thickness. The suitability of the approximation depends on the substrate. As an example, it fails for a substrate of bulk Mo and carbon layers in the same thickness range because the optical contrast leads to much stronger interference effects. For ultrathin carbon films equation (20) will be used to determine the reflectance loss, based on estimates of $\rho d$ from ellipsometer measurements and effective medium approximation (discussed below).
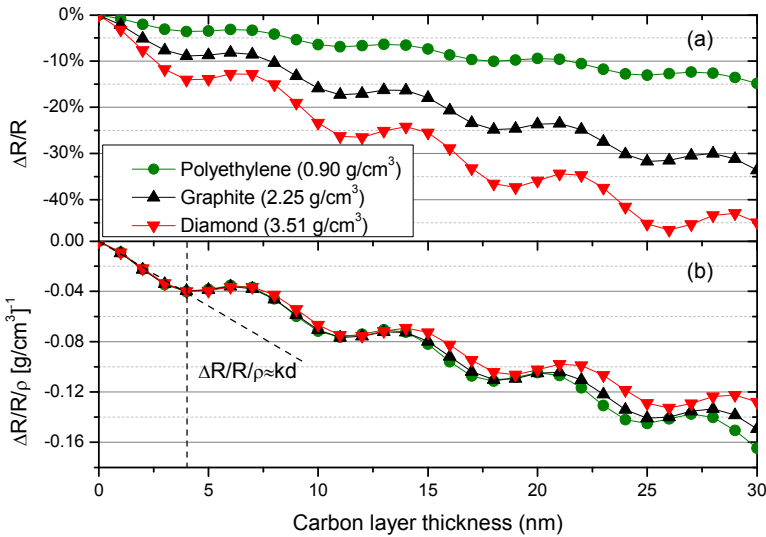


Fig. 30. Calculated relative EUV reflectance loss from an MLM (a) as a function of the carbon layer thickness for different carbon densities corresponding to different types of carbon films. Subfigure (b) shows the reflectance loss normalized by the carbon density.

### 5.5 Estimating the carbon density from the optical constants

To calculate the attenuation of the EUV reflectance upon carbon contamination of an MLM, the dielectric function of the carbon layer in the EUV wavelength range is required. A simple extrapolation of the dielectric function from the accessible region of ellipsometry is not feasible because of the substantial amount of absorption between 10 and 20 eV [6,18,19]. However, in our case, it is only necessary to know the density of carbon to calculate the change in EUV optical properties.

Estimates of carbon density, based on ellipsometric data, are complicated by the different bond structures of different carbon layers. The $sp^3$ bonds in diamond result in a large band gap between the bonding and antibonding $\sigma$ bonds, leading to absorption in the UV range. The introduction of $sp^2$ bonds, as found in graphite-like carbon, introduces the bonding and antibonding $\pi$ bands close to the Fermi energy. This results in a higher refractive index in the visible range. However, the carbon density decreases for this higher refractive material. Table 3 lists refractive indexes at a wavelength of 600 nm, and carbon density for several carbon species. These examples show that it is difficult to estimate the refractive index in the EUV region from refractive index data in the UV-NIR region.

The refractive index of carbon films, as well as their densities have been investigated by several groups [5-10,20-23]. These carbon films are diamond-like ($sp^3$ bond), graphite-like ($sp^2$ bond) or polymer-like (H-content). The refractive indexes of these films were all measured by ellipsometry. The accuracy of the carbon densities reported is about 10%.

These literature results, as well as our own measurements, are shown in Fig. 31(a), (b) and Table 3. The value of the refractive index at a wavelength of 600 nm was chosen because it is the most common wavelength for ellipsometry or reflectometry in the literature. The properties of bulk diamond, highly ordered pyrolytic graphite (HOPG) and polyethylene, $(C_2H_4)n$, are also depicted. From Fig. 31, it is observed that all the experimental values lie within the triangle defined by diamond, HOPG and $(C_2H_4)n$. The location of a particular film within this triangle characterizes it as diamond-like, graphite-like or polymer-like, as indicated in the figure. Moreover, a trend relating carbon density to the refractive index is observed.

Three methods have been proposed and used to estimate the carbon density from the optical properties in the UV-NIR range. First of all, the maximum value of the imaginary part of the dielectric function, $e2_{max}$ was used as a measure of film density [24]. However, $e2_{max}$ only provides qualitative variations of density and is not adequately accurate. The other two methods are based on Bruggeman's effective medium approximation (BEMA) and the Clausius-Mosotti (CM) equation. Below, we use these two methods to estimate the density of carbon films on MLMs.

*Table 3. The refractive index and extinction coefficient at 600 nm and the densities for four different kinds of carbon films*

| Carbon type | n | k | Density (g/cm$^3$) | Reference |
|---|---|---|---|---|
| Diamond | 2.42 | 0 | 3.515 | [25,26] |
| HOPG[1] | 3.19 | 1.80 | 2.266 | [26,27] |
| 50/50-C[2] | 2.83 | 0.85 | 2.891 | [25,26] |
| polyethylene | 1.48 | 0 | 0.92 | [5,28] |

[1] The refractive index of HOPG was measured in our experiments.

[2] 50/50-C is a defined effective medium with 50% diamond and 50% HOPG.

## 5.5.1    Effective medium approximation

The BEMA is broadly applied to estimate the relationship between the density and the refractive index for a variety of semiconductor and dielectric materials [24,29-31]. In this case, the carbon film is considered to be a porous film, consisting of voids and carbon. The carbon can be present as diamond, HOPG or $(C_2H_4)n$, reflecting the various carbon bonding geometries. We also define a synthetic material, consisting of 50% diamond and 50% HOPG (50/50-C), i.e. a combination of sp$^3$ and sp$^2$ bonding. The effective dielectric function, $\varepsilon_{eff}$ , is calculated from the BEMA equation [13]:

$$0 = f_v \frac{\varepsilon_v - \varepsilon_{eff}}{\varepsilon_v + 2\varepsilon_{eff}} + f_C \frac{\varepsilon_C - \varepsilon_{eff}}{\varepsilon_C + 2\varepsilon_{eff}} \tag{21}$$

where $f_v$ and $f_C$ denote the volume fraction of void and carbon ( $f_v + f_C = 1$) while $\varepsilon_v$ and $\varepsilon_C$ are their respective dielectric functions. The complex refractive index of the film equals $\sqrt{\varepsilon_{eff}}$ . The density is $f_C$ times the carbon density corresponding to graphite, diamond, or polyethylene.

Fig. 31 shows the calculated relationship between the complex refractive index (i.e. the real part *n* and the imaginary part *k*), and density, based on equation (21). Five compositions are displayed: "diamond+HOPG", "HOPG+void", "diamond+void", "$(C_2H_4)n$+void", and "50/50-C+void". The slope of the curve "HOPG+void" is much steeper than that of the curve "diamond+void" for both the real and imaginary part of the refractive index. Note that the result of "$(C_2H_4)n$+void", and the "50/50-C+void" are very similar for the real part of refractive index. However, extinction coefficient shows a very different behaviour, with the "$(C_2H_4)n$+void" curve close to the "diamond+void" as both are transparent at the wavelength of 600 nm.

The experimental refractive index data for carbon films fall roughly into two categories, diamond-like and graphite-like, as can be seen in Fig. 31(a). They tend to

cluster around the "50/50-C+void" that separates the two regions. However, Fig. 31(b) shows that the extinction coefficient for most of the experimental values is close to $k = 0$ instead of the "50/50-C+void" curve. This can be explained by the connectivity of the non-void regions. The absorption of HOPG is dominated by conductive electrons, thus it is instructive to examine the BEMA, as applied to a metal-dielectric composite. The conductivity of the effective medium is zero if the relative volume fraction of the metal constituent is less than 1/D, where D is the dimension [32]. This is the so-called percolation threshold. For a three-dimensional sample consisting of spherical grains, the percolation threshold is 1/3, while for two-dimensional samples it is 1/2. For a carbon film, the extinction coefficient at 600 nm results from free electron absorption and absorption due to $\pi$ electrons in the $sp^2$ bonds. An example is the extinction coefficient of graphite as shown in the reference [6]. This means, for carbon films with $sp^2$ bonded carbon volume less than the percolation threshold (1/3-1/2), the absorption due to free electrons vanishes. This results in the decrease of the extinction coefficients as shown in Fig. 31(b) as a contrast to Fig. 31(a).

For carbon films whose refractive index and density are very close to the curve "50/50-C+void", their extinction coefficients are close to $k = 0.15$ at 600 nm. Generally, we refer to this kind of carbon as amorphous carbon. Based on this, we define a boundary at $k = 0.15$ (shown in Fig. 31 (b)) to separate diamond-like and polymer-like carbon ($k < 0.15$) from graphite-like carbon ($k \geq 0.15$).

Fig. 31 shows that the BEMA can be used to establish a relation between the complex refractive index and the carbon density. It also means the carbon density can be estimated from the refractive index and extinction coefficient. The density was estimated from the BEMA using the value of the refractive index and extinction coefficient at 600 nm because this wavelength provides the minimum uncertainty range of carbon density. For a given refractive index (also extinction coefficient), the range of possible densities lies on the line of constant refractive index (also extinction coefficient) that begins at the intersection with the black "HOPG + void" curve and terminates at either the purple "diamond + void" (only for refractive index) or blue "diamond + HOPG" curves. In order to reduce the range of the density determined by refractive index, a carbon film is defined as diamond-like (or polymer-like) if its extinction coefficient is less than 0.15, and graphite-like if it is greater than 0.15. The two film types have their boundary along the "50/50-C + void" curve. Once the type of film is determined, the upper (lower) density limit for graphite-like (diamond-like or polymer-like) films is given by the intersection between the line of constant refractive index and the orange "50/50-C + void curve".
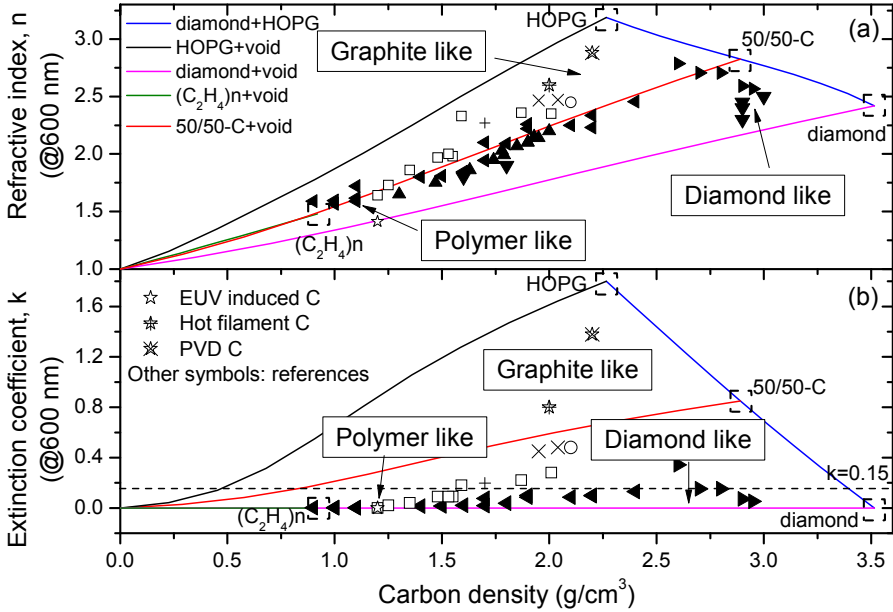
*Fig. 31. Calculated refractive index (a) and extinction coefficient (b) for a wavelength of 600 nm as a function of carbon density based on Bruggeman's effective medium approximation. The five curves correspond to the compositions of "diamond+HOPG", "HOPG+void", "diamond+void", "$(C_2H_4)n$+void" and "50/50-C+void". The experimental data in the references are also plotted with symbols as a comparison (▲[7], ▼[21], ◄[9], ►[6], □[8], ○[10], ×[20,23], +[22]). The extinction coefficient $k = 0.15$ is a defined boundary between diamond-like (or polymer-like) and graphite-like carbon.*

## 5.5.2   The Clausius-Mosotti equation

The Clausius-Mosotti (CM) formula has been used by several authors to relate the density and the dielectric function [30,31,33,34]. The Clausius-Mosotti equation is:

$$\alpha(0) = \frac{3}{4\pi N}\left(\frac{e1(0)-1}{e1(0)+2}\right) \tag{22}$$

where $\alpha(0)$ is the static polarizability (i.e. at zero photon energy) and $e1(0)$ is the real part of dielectric function at zero photon energy, and the medium is made up of N atoms (or ions) per unit volume.

The static polarizability for carbon is different for its various forms, graphite, diamond and hydrocarbon polymers (see Table 4). Hydrocarbon molecules $C_2H_2$, $C_2H_4$ and $C_2H_6$ are representative of the main constituents in polymer-like carbon films. For graphite, the polarizability is anisotropic [34], so the average polarizability is used in our calculations. Fig. 32 shows the static dielectric function $e1(0)$ as a function of the carbon density according to the CM equation (22). Diamond-like carbon lies in the

region between $\alpha(0)$ =0.815 and 1.265, and graphite-like carbon lies in the region between $\alpha(0)$=1.265 and 1.76.

The static dielectric function $e1(0)$ can not be measured directly with ellipsometry, however, it can be estimated by extrapolating from the UV-NIR, based on the parameterization of the dielectric functions of different types of carbon films [6]. The extrapolated values for the measured carbon films are shown in Fig. 32.

As the estimation of density based on the BEMA, a similar procedure was used for the method based on the CM equation. The extrapolated dielectric function, $e1$, at photon energy of zero, $e1(0)$, was obtained by extrapolating the dielectric function in the NIR-UV. The boundary $k = 0.15$ at the wavelength of 600 nm was used to determine the carbon type. Taking into account the range of the reported values of polarizabilities in the literature, as shown in Table 4, a density range was calculated based on equation (22). As shown in Fig. 32, the estimated upper and lower limits for diamond-like carbon films are determined by the curve of $\alpha(0)$ =0.815 (diamond) and 1.265 (graphite). While for graphite-like carbon films, the limits are determined by the density curves with limiting values given by $\alpha(0)$=1.265-1.76 (graphite). The HOPG density of 2.266 g/cm$^3$ was applied as the upper limit of the density of graphite-like carbon. For those carbon films with $e1(0)$ close to 2, corresponding to polymer-like films, we applied the maximum limits determined by the curve of $\alpha(0)$=0.815 (diamond) and 4.252 (C$_2$H$_4$).

*Table 4. Static polarizability of different types of carbon and hydrocarbons*

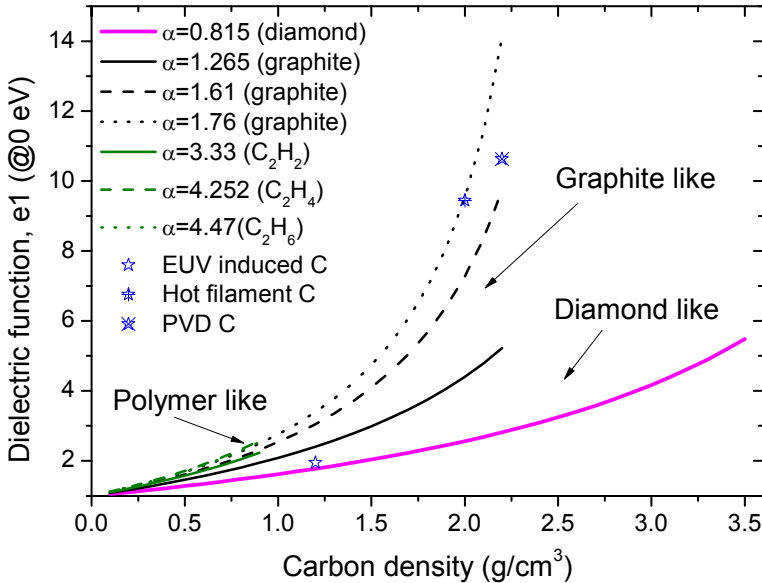| Carbon type | Static polarizability ($10^{-24}$ cm$^3$) | reference |
|:---:|:---:|:---:|
| diamond | 0.815 | [35] |
| graphite | 1.61* | [34] |
| graphite | 1.76 | [36] |
| graphite | 1.265 | [37] |
| C$_2$H$_2$ | 3.33 | [36] |
| C$_2$H$_4$ | 4.252 | [36] |
| C$_2$H$_6$ | 4.47 | [36] |

* Averaged polarizability is used.

*Fig. 32. Calculated static dielectric function, e1 (@0 eV) as a function of carbon density, according to the Clausius-Mosotti equation. The seven curves correspond to the static polarizability values of diamond, graphite and polymers listed in Table 4. Our experimental data for EUV induced C, hot filament C and PVD C are also plotted with blue starts.*

### 5.6    Estimation of EUV reflectance loss

As described in section 5.4, to estimate the EUV reflectance loss of an MLM due to carbon deposition, both the carbon layer thickness and density are required. The BEMA and CM equation were used to estimate the carbon density. As a comparison, the EUV reflectance was measured with a reflectometer and the relative reflectance loss was calculated based on equation (19).

Table 5 shows the range of estimated carbon densities calculated from the BEMA and the CM equation. The density, as measured by GIXR, is also listed as a comparison. There is a good agreement between the three measurements.

Fig. 33 shows the comparison of EUV reflectance loss measured and the estimated reflectance loss based on the densities derived from the BEMA and the CM equation for the three kinds of carbon films. The uncertainty of the measured reflectance loss was 0.6%, based on the absolute reflectance measurement error of 0.2%. On the other hand, the uncertainty of the estimated reflectance loss depends on the carbon type and the approach applied. In addition, for both approaches, the uncertainty range increases with increasing thickness.

First of all, the estimated reflectance losses of the four different EUV carbon films as calculated with both approaches agree well with the measured reflectance losses. For

the hot filament carbon films, the BEMA estimated reflectance losses agree to within uncertainties with the measured reflectance losses, while the values calculated from the CM equation are 4% higher than the measured value. However, the BEMA estimated uncertainty is 3 times larger than that of the CM equation.

For the PVD carbon films, the estimated reflectance losses based on both approaches were about 4% higher than the measured values. Overall, for both the hot filament and PVD carbon, the estimated reflectance losses are all about 4% higher than the measured values. We believe that the main reason is the overestimation of the optical constants calculated from equation (18) for graphite-like carbon. On the other hand, only for polymer films, optical constants for the EUV wavelength range calculated from equation (18) have been confirmed experimentally [17].

As shown in Fig. 33, both the BEMA and the CM equation can be used to estimate the reflectance loss due to carbon deposition with a maximum systematic offset of 4% in the loss range of up to ~30%. In addition, for EUV induced carbon, the BEMA estimated reflectance loss agrees better with the experimental data. Furthermore, the complex refractive index at 600 nm can be obtained with ellipsometry directly for the BEMA. On the other hand, for the CM equation, the dielectric function at zero photon energy must be obtained through extrapolation. In addition, the polarizability limits used in the CM equation were obtained from literature values from unmixed samples, and it is unclear if these represent the full range of possible polarizability values for mixed samples. Overall, the BEMA works slightly better and appears more reliable than the CM equation for estimation of the reflectance loss by determining the carbon density.

*Table 5. Estimation of carbon density according to the refractive index or the dielectric function based on the BEMA and the CM equation. The upper and lower limits are listed. The measured density by GIXR is also listed as a comparison.*

| Carbon type | n @600 nm | Density$^+$ (g/cm$^3$) | density$^-$ (g/cm$^3$) | e1 @0 eV | Density$^+$ (g/cm$^3$) | Density$^-$ (g/cm$^3$) | Density (g/cm$^3$) |
|---|---|---|---|---|---|---|---|
| Method | measured | BEMA | BEMA | extrapolated | CM | CM | GIXR |
| EUV C | 1.41 | 1.17 | 0.79 | 1.95 | 1.40 | 0.63 | 1.2±0.2 |
| Hot C | 2.60 | 2.53 | 1.68 | 9.44 | 2.266[1] | 1.99 | 2.0±0.1 |
| PVD C | 2.88 | 2.54[2] | 1.95 | 10.63 | 2.266[1] | 2.06 | 2.2±0.2 |

[1] The density of HOPG is applied as the upper limit of graphite like carbon.

[2] This limit is based on *k* (blue curve in Fig. 31(b)) because it is smaller than that based on *n*
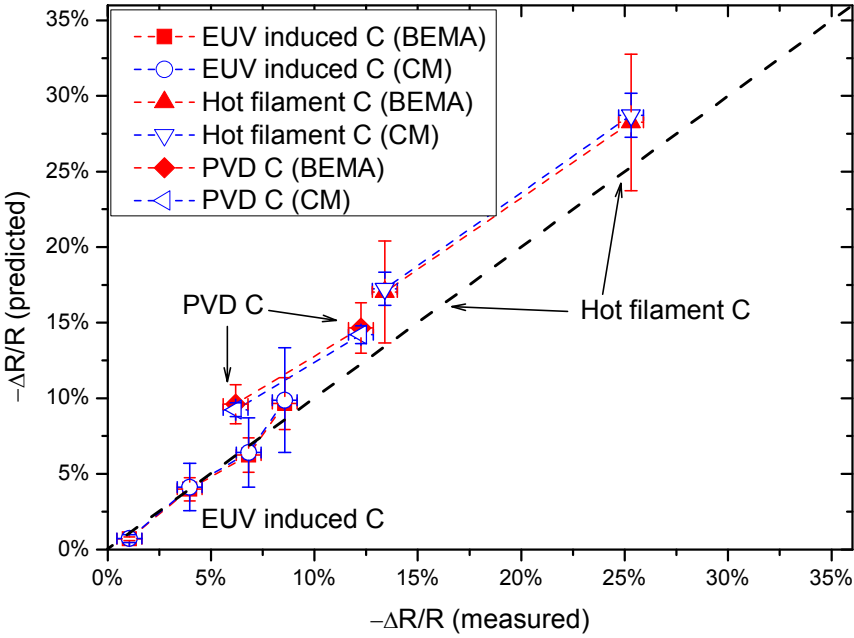
*Fig. 33. Comparison of relative EUV reflectance losses between the measured and estimated values based on Bruggeman's effective medium approximation and the Clausius-Mosotti equation with different carbon layer thicknesses including hot filament carbon, EUV induced carbon and PVD carbon.*

## 5.7    Application for ultrathin carbon films

For ultrathin films with a thickness of a few nanometers, it is very difficult to determine the refractive index and the thickness independently using spectroscopic ellipsometry. This is because, in the thin film limit, thickness and refractive index become correlated and only the product of the refractive index and thickness (i.e. $nd$ ) can be determined. For the BEMA method, Fig. 31(a) implies that a good relationship between $nd$ and the product of the density and thickness (i.e. $\rho d$ ) exists. The product of density and thickness is actually the amount carbon per surface area, the critical factor for the EUV reflectance loss as we observed that $\Delta R / R \approx k \rho d$  (see equation (20)).

In order to reduce the estimated uncertainty range of  $\rho d$ , we need to determine if a carbon film is graphite-like or diamond-like (also polymer-like). To achieve this, the change of the two ellipsometric angles (i.e. $\Psi$ and $\Delta$) as carbon is deposited has to be used. Fig. 34 shows the trajectory of $\Psi$ and $\Delta$ for a wavelength of 600 nm and an angle of incidence of 70° with respect to the surface normal. Each point is from a different MLM that has had a thicker layer of carbon deposited on it. As shown in Fig. 34, EUV induced and hot filament carbon display very different trajectories. This is because EUV

induced carbon is polymer-like while hot filament carbon is graphite-like. In addition, a calculated trajectory for a carbon film with a complex refractive index of 2.455+0.13i [9] is shown as a rough boundary between graphite-like and diamond-like (also polymer-like) (as shown in Fig. 31). This example shows that the trajectory of the two ellipsometry angles can be used to determine the type of carbon film, which, in turn allows the density and reflectance loss of the carbon film to be accurately estimated.
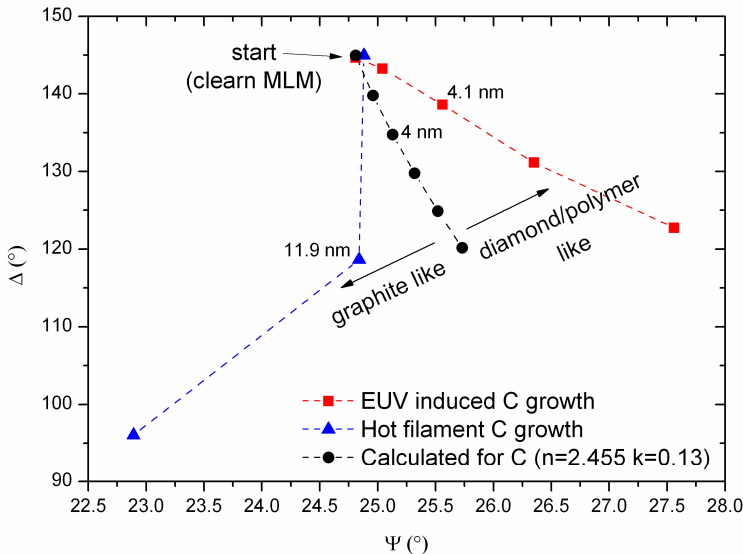


*Fig. 34. The trajectory of the ellipsometric angles, Ψ and Δ at a wavelength of 600 nm, when a carbon layer is deposited on a multilayer mirror. The squares and triangles correspond to the deposition of EUV induced carbon and hot filament carbon respectively. Another trajectory for carbon deposition with a complex refractive index of 2.455+0.13i was calculated and plotted as a rough boundary between graphite-like and diamond-like (also polymer-like carbon).*

## 5.8   Conclusion

The EUV reflectance loss of a multilayer mirror due to carbon deposition is mainly determined by the carbon layer thickness and the type of carbon deposited since the latter causes changes in refractive index (or dielectric function). In the EUV wavelength range, the refractive index of a carbon film is mainly determined by its atomic density. In this paper, spectroscopic ellipsometry has been used to determine the thickness and the refractive index for EUV induced carbon, hot filament carbon and PVD carbon by e-beam evaporation on top of multilayer mirrors.

In order to estimate the carbon density from the refractive index in the wavelength range from ultraviolet to near infrared, two different approaches were analyzed. The first approach was based on Bruggeman's effective medium approximation (BEMA).

We observed that the experimental carbon densities as well as their refractive indexes published are well described by the BEMA.

The second approach was based on the Clausius-Mosotti (CM) equation, which was used to derive the density of carbon films from an extrapolated dielectric function.

The EUV reflectance losses due to carbon depositions were measured with a reflectometer and compared to the estimated losses, based on the two approaches. Good agreement was obtained, with error estimates being at most 4% in the reflectance loss range from 0% up to ~30%. This means that we could estimate the EUV reflectance loss accurately using spectroscopic ellipsometry.

For ultrathin carbon films with a thickness of a few nanometers, we can determine the type of carbon by the trajectory of the two ellipsometry angles. Since determination of the refractive index and thickness independently is very difficult, we determined the product of the refractive index and thickness (i.e. $nd$ ). Furthermore, using the BEMA, we show that the product of the density and thickness (i.e. $\rho d$ ) can be estimated from the parameter $nd$ . Finally we show that a simplified relationship between the reflectance loss and the product of density and thickness (i.e. $\Delta R / R \approx k \rho d$ ) can be used to estimate the reflectance loss due to carbon deposition.

### *5.9    Acknowledgements*

### *5.10   References*

[1]  J. Hollenshead and L. Klebanoff, Modeling radiation-induced carbon contamination of extreme ultraviolet optics, Journal of Vacuum Science & Technology B 24 (2006) 64-82.

[2]   K.-J. Boller, R.-P. Haelbich, H. Hogrefe, W. Jark, and C. Kunz, Investigation of carbon contamination of mirror surfaces exposed to synchrotron radiation, Nuclear Instruments and Methods in Physics Research 208 (1983) 273-279.

[3]   J. Q. Chen, C. J. Lee, E. Louis, F. Bijkerk, R. Kunze, H. Schmidt, D. Schneider, and R. Moors, Characterization of EUV induced carbon films using laser-generated surface acoustic waves, Diamond and Related Materials 18 (2009) 768-771.

[4]   J. Q. Chen, E. Louis, C. J. Lee, H. Wormeester, R. Kunze, H. Schmidt, D. Schneider, R. Moors, W. van Schaik, M. Lubomska, and F. Bijkerk, Detection and characterization of carbon contamination on EUV multilayer mirrors, Optics Express 17 (2009) 16969-16979.

[5]   J. Robertson, Diamond-like amorphous carbon, Materials Science & Engineering R-Reports 37 (2002) 129-281.

[6]   S. Waidmann, M. Knupfer, J. Fink, B. Kleinsorge, and J. Robertson, Electronic structure studies of undoped and nitrogen-doped tetrahedral amorphous carbon using high-resolution electron energy-loss spectroscopy, Journal of Applied Physics 89 (2001) 3783-3792.

[7]   P. Koidl, C. Wild, B. Dischler, J. Wagner, and M. Ramsteiner, Plasma deposition, properties and structure of amorphous hydrogenated carbon films, 1989, 52, p. 41-70.

[8]   C. Godet, N. M. J. Conway, J. E. Bouree, K. Bouamra, A. Grosman, and C. Ortega, Structural and electronic properties of electron cyclotron resonance plasma deposited hydrogenated amorphous carbon and carbon nitride films, Journal of Applied Physics 91 (2002) 4154-4162.

[9]   T. Schwarz-Selinger, A. von Keudell, and W. Jacob, Plasma chemical vapor deposition of hydrocarbon films: The influence of hydrocarbon source gas on the film properties, Journal of Applied Physics 86 (1999) 3988-3996.

[10]  S. V. Singh, M. Creatore, R. Groenen, K. Van Hege, and M. C. M. van de Sanden, A hard graphitelike hydrogenated amorphous carbon grown at high deposition rate (> 15 nm/s), Applied Physics Letters 92 (2008) -.

[11]  E. Louis, H. J. Voorma, N. B. Koster, L. Shmaenok, F. Bijkerk, R. Schlatmann, J. Verhoeven, Y. Y. Platonov, G. E. Vandorssen, and H. A. Padmore, Enhancement of Reflectivity of Multilayer Mirrors for Soft-X-Ray Projection Lithography by Temperature Optimization and Ion-Bombardment, Microelectronic Engineering 23 (1994) 215-218.

[12]  J. W. Weber, T. A. R. Hansen, M. C. M. v. d. Sanden, and R. Engeln, B-spline parametrization of the dielectric function applied to spectroscopic ellipsometry on amorphous carbon, Journal of Applied Physics 106 (2009) 123503.

[13]  *Handbook of ellipsometry*; *Vol.*, edited by H. G. Tompkins and E. A. Irene (William Andrew, 2005).

[14]  A. C. Ferrari, A. Libassi, B. K. Tanner, V. Stolojan, J. Yuan, L. M. Brown, S. E. Rodil, B. Kleinsorge, and J. Robertson, Density, sp(3) fraction, and cross-sectional

structure of amorphous carbon films determined by x-ray reflectivity and electron energy-loss spectroscopy, Physical Review B 62 (2000) 11089-11103.

[15] D. L. Windt, IMD - Software for modeling the optical properties of multilayer films, Computers in Physics 12 (1998) 360-370.

[16] D. Attwood, Soft X-Rays and Extreme Ultraviolet Radiation: Principles and Applications, 1999.

[17] Y. J. Kwark, J. P. Bravo-Vasquez, M. Chandhok, H. D. Cao, H. Deng, E. Gullikson, and C. K. Ober, Absorbance measurement of polymers at extreme ultraviolet wavelength: Correlation between experimental and theoretical calculations, Journal of Vacuum Science & Technology B 24 (2006) 1822-1826.

[18] D. Franta, D. Necas, L. Zajickova, and V. Bursikova, Limitations and possible improvements of DLC dielectric response model based on parameterization of density of states, Diamond and Related Materials 18 (2009) 413-418.

[19] D. Franta, D. Necas, L. Zajickova, V. Bursikova, and C. Cobet, Band structure of diamond-like carbon films assessed from optical measurements in wide spectral range, Diamond and Related Materials 19 (2010) 114-122.

[20] T. Zaharia, R. Groenen, P. Persoone, and M. C. M. van de Sanden, Graphite-like hydrogenated amorphous carbon for tribological applications grown by a remote plasma, M2i conference 2009, 2009.

[21] M. Chhowalla, J. Robertson, C. W. Chen, S. R. P. Silva, C. A. Davis, G. A. J. Amaratunga, and W. I. Milne, Influence of ion energy and substrate temperature on the optical and electronic properties of tetrahedral amorphous carbon (ta-C) films, Journal of Applied Physics 81 (1997) 139-145.

[22] J. W. Weber, Thesis, Eindhoven University of Technology, 2009.

[23] S. V. Singh, T. Zaharia, M. Creatore, R. Groenen, K. V. Hege, and M. C. M. v. d. Sanden, Hard graphitelike hydrogenated amorphous carbon grown at high rates by a remote plasma, Journal of Applied Physics 107 (2010) 013305.

[24] T. Haage, U. I. Schmidt, H. Fath, P. Hess, B. Schroder, and H. Oechsner, Density of Glow-Discharge Amorphous-Silicon Films Determined by Spectroscopic Ellipsometry, Journal of Applied Physics 76 (1994) 4894-4896.

[25] *Handbook of optical constants of solids*; *Vol.*, edited by E. D. Palik (Academic press, 1985).

[26] D. C. Ingram, J. A. Woollam, and G. Buabbud, Mass Density and Hydrogen Concentration in Diamond-Like Carbon-Films - Proton Recoil, Rutherford Backscattering and Ellipsometric Analysis, Thin Solid Films 137 (1986) 225-230.

[27] http://www.nanophoenix.com/index1.html, Graphite / HOPG 2010

[28] *Handbook of Optical Constants of Solids II*; *Vol.*, edited by E. D. Palik (Academic press, 1991).

[29] J. R. Blanco, P. J. Mcmarr, J. E. Yehoda, K. Vedam, and R. Messier, Density of Amorphous-Germanium Films by Spectroscopic Ellipsometry, Journal of Vacuum Science & Technology a-Vacuum Surfaces and Films 4 (1986) 577-582.

[30] O. Buiu, W. Davey, Y. Lu, I. Z. Mitrovic, and S. Hall, Ellipsometric analysis of mixed metal oxides thin films, Thin Solid Films 517 (2008) 453-455.

[31] W. Davey, O. Buiu, M. Werner, I. Z. Mitrovic, S. Hall, and P. Chalker, Estimate of dielectric density using spectroscopic ellipsometry, Microelectronic Engineering 86 (2009) 1905-1907.

[32] D. Stroud, The effective medium approximations: Some recent developments, Superlattices and Microstructures 23 (1998) 567-573.

[33] K. Sangwal and W. Kucharczyk, Relationship between Density and Refractive-Index of Inorganic Solids, Journal of Physics D-Applied Physics 20 (1987) 522-525.

[34] D. Nicholson, Graphite Polarizability, Surface Science 181 (1987) L189-L192.

[35] J. C. Phillips, Dielectric Definition of Electronegativity, Physical Review Letters 20 (1968) 550.

[36] *CRC Handbook of Chemistry and Physics Vol.*, edited by D. R. Lide (2009-2010).

[37] F. Torrens, Molecular polarizability of Sc and C (Fullerene and Graphite) clusters, Molecules 6 (2001) 496-509.

## 6 *In situ* ellipsometry study of atomic hydrogen etching of EUV induced carbon layers

### 6.1 Abstract

Atomic hydrogen based etching is generally considered an efficient method for the removal of carbon films resulting from photo-induced hydrocarbon dissociation, like in EUV photolithography environments. The etch rate of atomic hydrogen for three different kinds of carbon films was determined, namely for EUV induced carbon, hot filament evaporated carbon and e-beam evaporated carbon. The etching process was monitored *in situ* by spectroscopic ellipsometry. The etch rate was found to depend on the type of carbon (polymer or graphite like), on the layer thickness, and on the temperature. The EUV induced carbon shows the highest etch rate, with a value of ~ 0.2 nm/min at a sample temperature of 60° C. The more graphite like carbon layers showed an etch rate that was about 10 times lower at this temperature. An activation energy of 0.45 eV was found for etching of the EUV induced carbon layer.

### 6.2 Introduction

Extreme ultraviolet lithography (EUVL) is a next generation photolithographic technique that uses extreme ultraviolet radiation (13.5 nm) for imaging at ultra high resolution. Reflective, Mo/Si multilayer coated mirrors (MLMs) are a key component in this technology. The contamination of the surface of these mirrors by EUV induced carbon deposition would reduce the mirror reflectivity and thus forms one of the main threats for their application [1-5]. One of the challenges in developing EUVL equipment is the development of effective and rapid cleaning techniques that can restore the EUV optical properties. Several methods for the removal of carbon contamination have been proposed, including atomic hydrogen ($H^0$) cleaning [6-13], EUV radiation assisted molecular oxygen cleaning [14,15], ozone cleaning [16], and radio frequency discharge cleaning using oxygen or hydrogen plasmas [17]. Among these methods, $H^0$ cleaning is considered to be most attractive since it can both volatilize carbon and reduce or eliminate the risks of oxidation of the optics associated with cleaning with ions [8]. In case of oxide formation on top surface layers [18], $H^0$ cleaning can also reduce the surface oxide of the optics to restore its reflectivity [7,12].

The chemical erosion yield due to atomic hydrogen of an amorphous hydrogenated carbon film is about two orders of magnitude larger than that of bulk graphite [19,20]. However, to our knowledge, for both polymeric and graphitic films, the temperature dependence of the etch rate is unknown. Also a variation of the etch rate with film thickness has not been investigated so far. Both graphite and polymer like carbon contamination have been observed on optics under high energy photon radiation [11-13]. In this paper we will present a study of the etch rate for different types of

carbon films. For this purpose, three different types of carbon containing layers were produced, i.e. deposition via EUV induced photo-dissociation of hydrocarbons, deposition by a hot filament and by physical vapor deposition (PVD carbon) using e-beam evaporation. Both temperature and thickness dependence of these layers for the atomic hydrogen etching rate were investigated.

Previously published etch studies report on the abundance of the etch products (i.e. $CH_3$, $CH_4$, and heavier hydrocarbons) [19,20]. In our experiments, the etch rate was monitored *in situ* by measuring the carbon film thickness with spectroscopic ellipsometry, which is appropriate for *in situ* monitoring of carbon contamination layers on multilayer mirrors [21]. It allows to investigate the condition of the top surface of an EUV mirror and from that predict the reduced EUV reflectivity as a result of carbon contamination [22]. In the study of the etching behaviour, spectroscopic ellipsometry combines an adequate time resolution of a few seconds with the ability to accurately measure the film thickness at various temperatures, thus enabling to determine the etch rate in real time.

## 6.3    *Experimental*

### 6.3.1    Spectroscopic ellipsometry

Ellipsometry measures the change in polarization state of a light beam reflected from the surface of a sample. This change in polarization is expressed by the two ellipsometric angles, i.e. psi ($\Psi$) and delta ($\Delta$), that are related to the ratio of two Fresnel reflection coefficients $r_p$ and $r_s$ for *p*- and *s*- polarized light, respectively.

$$\frac{r_p}{r_s} = \tan(\Psi)e^{i\Delta} \tag{23}$$

A spectroscopic ellipsometer (Woollam, M-2000, spectral range 245-1689 nm) was installed on our deposition and cleaning chamber for *in situ* monitoring of the cleaning process. The incidence angle was 76.4° with respect to the surface normal. The measured spectra were analyzed and a thickness of the remained layer was determined. Standard procedures for data analysis and thickness determination were used [23-25].

### 6.3.2    Carbon layer deposition and characterization

In our etch studies Si (001) wafers with native oxide were used as substrates instead of MLM. These are standard for ellipsometry calibration and the data interpretation is simpler than on a MLM. Three types of carbon films were deposited. The first type, "EUV induced C", was grown by exposing the wafer to EUV radiation in the presence of residual hydrocarbons in the vacuum. The second type of carbon, referred to as "hot filament C", was deposited by evaporation from a graphite filament. The third type of

carbon layer was deposited using physical vapor deposition (PVD) by e-beam evaporation of a graphite target. This layer is referred to as "PVD C".

Prior to the etch studies, X-ray photoelectron spectroscopy (XPS) was used to analyze the carbon hybridization ratio $sp^3/sp^2$, which, in combination with the density of the layers, reflects the polymer - graphite fraction [26-28]. Grazing incidence X-ray reflectivity (GIXR) measurements using Cu-$K_\alpha$ radiation and modeling with the software package IMD [29] provided the carbon density and confirmed the thickness determined by ellipsometry. Furthermore, spectroscopic ellipsometry provided the optical constants (n + ik). Laser-generated surface acoustic waves (LG-SAWs) were used to investigate the Young's modulus [30].

Table 6 shows the properties determined by the aforementioned methods of the three different types of carbon films. EUV induced carbon is polymeric with a major $sp^3$ hybridization (C-H bonds). It is transparent in the wavelength range of visible light with a refractive index of 1.4 and it has the lowest density (about 1.2 g/cm$^3$). On the other hand, hot filament carbon and PVD carbon are both graphite like carbon with an $sp^3/sp^2$ ratio of 0.7 and 0.5, respectively. Their densities are similar: 2.0 and 2.2 g/cm$^3$, respectively. The optical constants of each carbon film are consistent with their bond structure and density. The optical constants of the PVD C are thickness dependent (discussed in section 6.4.3) and the thickness of the PVD film in Table 6 is 2.8 nm.

*Table 6. Properties of EUV induced carbon, hot filament carbon and PVD carbon*

| Parameter | EUV induced C | Hot filament C | PVD C |
|---|---|---|---|
| n+ik (600 nm) | 1.4+0i | 2.6+0.8i | 2.7+1.2i |
| $sp^3/sp^2$ | 10.2 | 0.7 | 0.5 |
| Density (g/cm$^3$) | 1.2±0.2 | 2.0±0.1 | 2.2±0.2 |
| Hydrogenated | yes | no | No |
| Carbon type | Polymer like | Graphite like | Graphite like |

## 6.3.3 Atomic hydrogen cleaning

The mechanism of chemical erosion due to thermal hydrogen atoms has been reviewed in literature [19]. Hydrogen atoms impact and react with the carbon material forming volatile hydrocarbons such as CH$_3$, CH$_4$, and a number of heavier species [19]. A simple hot wire thermal hydrogen cracker as described in [6,8,10] was installed on our chamber to supply the H$^0$ for exposure. Fig. 35 shows the schematic configuration of the cleaning chamber. The etching by exposure to H$^0$ was started by switching a current through a tungsten filament, heating the wire to about 2000° C. At this temperature hydrogen molecules are thermally dissociated to hydrogen atoms. The filament is placed 5 cm in front of the sample and a shield was placed between the filament and the sample

to avoid tungsten contamination directly from the filament and to reduce the thermal load to the sample. In order to achieve a stable and sufficiently high $H^0$ flux, the hydrogen pressure during exposure is fixed at 0.2 mbar.

The sample temperature was measured by a Pt-100 temperature sensor installed on the sample surface. There were two different ways to investigate the temperature dependence. For EUV induced carbon, the etch rate is so high that determination of the etch rate while increasing the temperature in a controlled step-like way was not possible. Therefore the sample temperature was not controlled and the etch rate was determined while the heat from the filament induced a sample temperature increase to 70° C. For the hot filament carbon, the sample temperature was varied and stabilized by varying the duty cycle of a heater fixed behind the sample holder, enabling to measure the etch rate with high accuracy in discrete steps. This also increased the temperature range that we investigated. For the PVD carbon layers, the sample temperature was controlled at 75° C to investigate the thickness dependence. The temperature dependence was investigated like in the case of the EUV induced carbon.
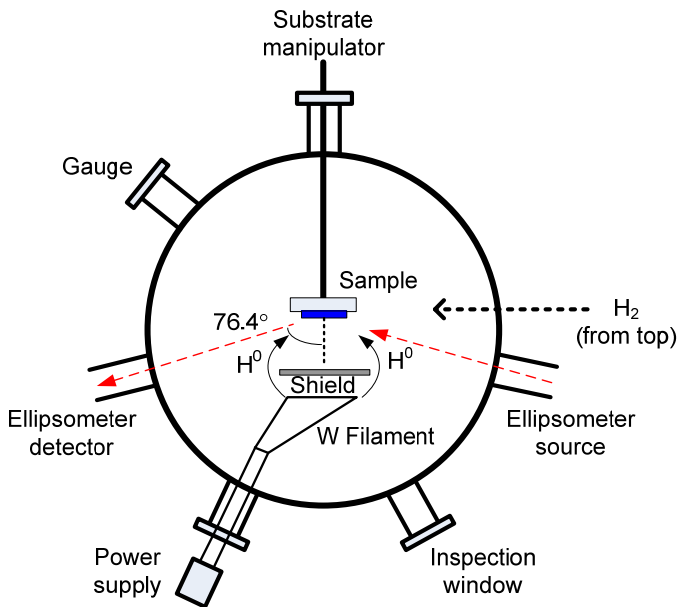


*Fig. 35. System configuration of atomic hydrogen cleaning*

## 6.4    Results and discussion

### 6.4.1    *In situ* monitoring of carbon cleaning

Fig. 36 (a) shows the sample temperature variation while etching the EUV induced carbon film. The sample temperature increases as a consequence of radiation from the

W wire. The time evolution of the thickness of this layer and its time derivative representing the etch rate is shown in Fig. 36 (b). Four exposure cycles were made to avoid a too high thermal load and to check the reproducibility of the etch rate at various temperatures. This also allows to determine whether the etch rate is temperature dependent (discussed in section 6.4.2).

Fig. 36 (b) shows a strong variation of the etch rate just after the first $H^0$ exposure was started. This can be explained by the fact that the surface of the film is covered by a thin layer of storage related hydrocarbons which might be relative easy to etch. After full removal of this layer, the etch rate decreases because of the lower etch rate of EUV induced carbon, followed by a monotonic increase due to the sample temperature increase (discussed in section 6.4.2). When the filament current is switched off, the $H^0$ flux vanishes and the thickness remains constant. After 110 to 120 minutes, at the end of the fourth cleaning cycle, the etch rate decreases even though the sample temperature still increases (see Fig. 36 (b)). A possible explanation is that because the remaining carbon film is only about 2 nm thick, the amount of carbon left for interaction with $H^0$ decreases. Possibly the carbon film in this stage is no longer a closed layer. A steadily increase of the already clean area would result in a decrease in the amount of carbon on the surface, i.e. a decrease in the monitored film thickness. The red dashed line is a guide to the eye of this approximately linear decrease in this regime. The 0.5 nm leftover after 140 minutes can be attributed to the inaccuracy of the model (e.g. the thickness of $SiO_2$) or a 0.5 nm layer of silicon carbide formed at the interface between the carbon and the native oxide of the silicon wafer [31,32]. This layer is more resistant to etching and is left behind on the substrate surface [31].

Fig. 37 (a) and (b) show the variation in thickness for a hot filament deposited carbon film. Both show the second etch cycle only, which removes the anomaly during the etching of the storage related contamination layer. The figure shows the outcome of two experiments: etching at varying temperature (a) like in the case of EUV induced carbon and etching at a constant temperature of 75° C (b), the former because without temperature stabilization, an inhibition of the etch rate is observed as a result of a too low etch rate for a sample temperature below 50° C. The very small increase in thickness shown in Fig. 37 (a) might be related to a slight variation in the optical constants at this temperature, but might also indicate an accumulation of hydrocarbons prior to the actual removal [19]. Fig. 37 (b) shows that small changes of the temperature as observed during the temperature stabilization after the filament is switched on, already leads to a very noticeable change in etch rate. After temperature stabilization, a linear decrease in thickness is observed.
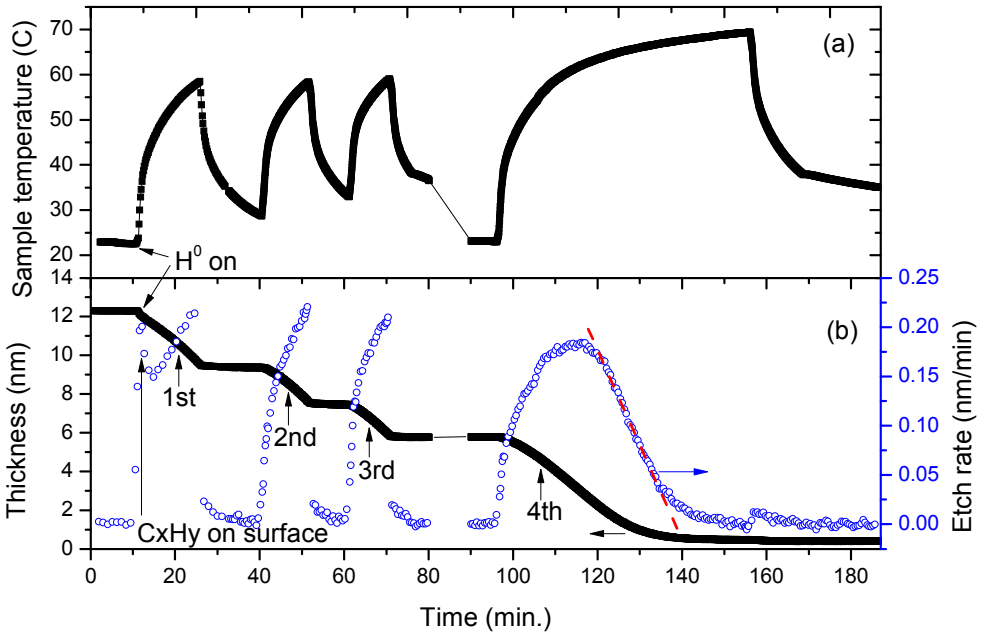
*Fig. 36. Sample temperature (a), thickness and etch rate (b) versus time during four times of $H^0$ cleaning of the EUV induced carbon film. The dashed line is a guide to the eye for a linear etch rate decrease.*
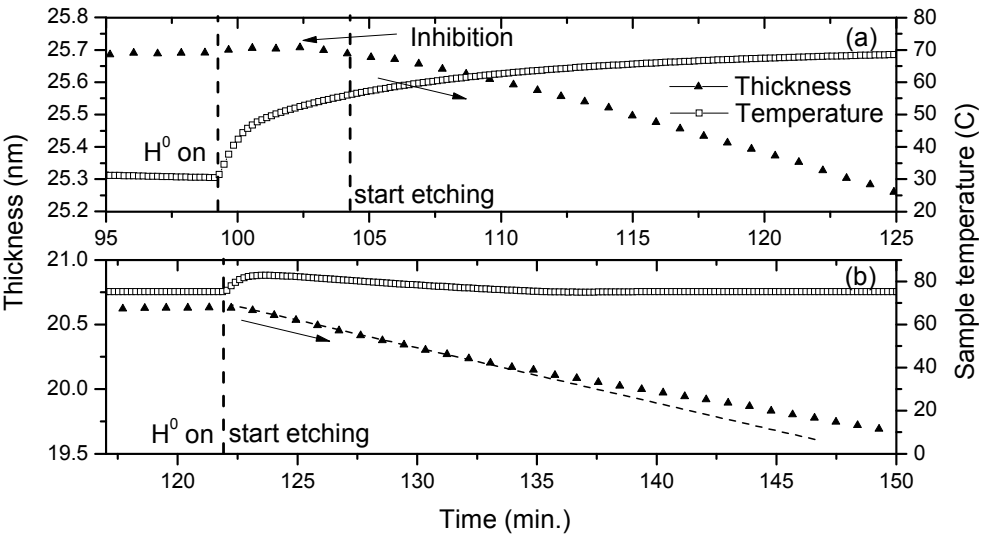


*Fig. 37. Thickness and sample temperature versus time during etching of hot filament carbon with temperature not controlled (a) and controlled (b).*

## 6.4.2 Temperature and carbon type dependence

The temperature during the EUV induced carbon etching increased from room temperature to about 60° C, see Fig. 36 (a). The etch rate versus the inverse temperature is plotted in an Arrhenius plot as depicted in Fig. 38. It shows that the etch rates of the first exposure for EUV induced carbon are slightly higher than that of the other three exposures. This difference for the first exposure is related to the removal of the top 3 nm (Fig. 36 (b)). This could be due to a slightly lower density of the top few nanometers which is in line with the increase of the carbon concentration with depth reported in [33].

The temperature dependence of etching of the PVD carbon film is investigated like in the case of the EUV induced carbon and is plotted in Fig. 38 as well. There were four exposures but the etch rates of the first one, especially in the lower temperature range, is much lower than the other three exposures. It is because for the first exposure the hydrogenation process prior to etching is dominant and not yet initiated as for the subsequent exposures (this process will be discussed in section 6.4.3). The etch rate decreases from the second to the fourth exposure while the thickness decreases. This indicates the etch rate might depend on thickness, a phenomenon which will be discussed in section 6.4.3.

In the case of hot filament carbon films, we used the sample heater to vary the temperature during etching from 65 to 100° C with 5° C intervals. At each temperature, the etch rate was monitored during 20 minutes. The error in the determined etch rate in Fig. 38 is caused by hydrogen pressure variation during the 20 minutes of exposure.

The etch rate is proportional to the reaction rate $k$ of the entire series of chemical reactions and physical processes between the atomic hydrogen and the carbon films. For a simple first order etch process, the Arrhenius equation describes the temperature dependence:

$$k = A \exp\left( \frac{-E_a}{k_B T} \right) \tag{24}$$

where $k_B$ is Boltzmann's constant, $A$ is a pre-exponential factor, $T$ is the substrate temperature, and $E_a$ is the activation energy of that reaction that determines the temperature dependence. Fig. 38 shows that for both EUV induced carbon and hot filament carbon the data is well described by equation (24). The deviation in the low temperature regime for EUV induced carbon is attributed to the large uncertainty in the determination of the etch rate. However, for the PVD carbon there are slightly higher deviations between the Arrhenius fit and the etch rate curves over the entire temperature range: the observed etch rate at 70° C is lower than the extrapolated value if based on the fit in the range below 65° C (not shown in the figure). One possible explanation is that the etch rate decreases with decreasing thickness (discussed in section 6.4.3) and therefore deviates from Arrhenius behavior.

Both the pre-exponential factor $A$ and the activation energy can be obtained by fitting equation (24) to the experimental data. The results, given in Table 7, indicate that

the pre-exponential factor for the case of EUV induced carbon is about three to four orders larger than in the case of hot filament carbon and also significantly larger than for PVD carbon, which means that the corresponding reaction processes are different. Samm [19] describes that the erosion of carbon must be preceded by a hydrogenation process. The high concentration of hydrocarbon in EUV induced carbon would dramatically reduces such a hydrogenation time required prior to erosion while for hot filament and PVD carbon both hydrogenation and erosion have to take place. Thus, the pre-exponential factor is higher for EUV induced carbon implying that it is etched faster.

Also, this factor can be influenced by the incident hydrogen flux. The same hydrogen fluxes applied for both cases might be adequate for etching the EUV induced carbon but they are too limited for the hot filament carbon. However, we do not expect that this effect can explain the 10 times difference in etch rates (see Table 7).

Although the hot filament carbon and PVD carbon films both contain non-hydrogenated carbon with a similar density (see Table 6) the etch rate of PVD carbon (see Fig. 39, discussed in section 6.4.3) is about twice that of hot filament carbon, at the same sample temperature of 75° C. This etch rate difference can be explained by the fact that the ratio of $sp^3/sp^2$ of PVD carbon is 0.5 which is slightly lower than that of hot filament carbon (0.7). The bonding ratio difference also means that the PVD carbon is more graphite like. In extreme cases for non-hydrogenated carbon films, the etch rate of pure graphite ($sp^2$ bond) is about 10 times higher than that of diamond ($sp^3$ bond) [20]. Thus, a higher etch rate is expected for a PVD carbon film with a lower ratio of $sp^3/sp^2$ (more graphite like), in agreement with our findings.

The difference in activation energy, with values of 0.26 eV, 0.40 eV and 0.45 eV for cleaning of hot filament carbon, PVD carbon and EUV induced carbon respectively, implies that there are different temperature dependences, so probably different chemical processes involved. This could be due to the fact that hot filament carbon consists of nanosized graphite fragments with a relatively high amount of dangling bonds, which could lower the activation energy for subsequent hydrogenation and erosion. A similar difference was observed between graphite and diamond by Vietzke et al. [20]. Note that the magnitude of the measured etch rates cannot be compared directly to the literature values, in which the chemical erosion yield per incident H is used [19], while we use the unit of nm/min. In addition, the cleaning conditions might be also different (e.g. $H^0$ flux).
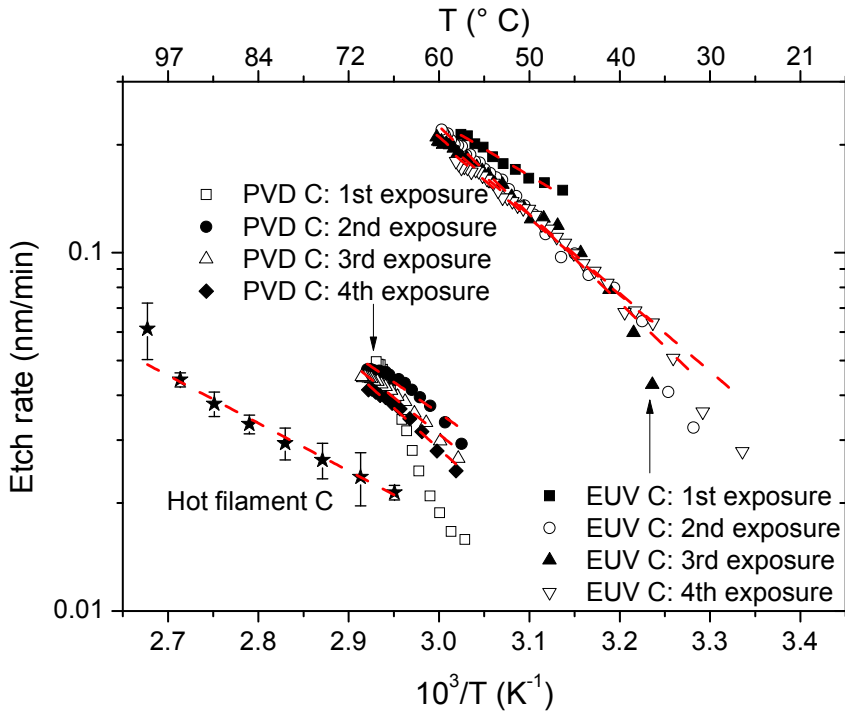
*Fig. 38. Arrhenius plot of the temperature dependence of the etch rate during four successive cleaning cycles of EUV induced carbon, four successive cleaning cycles of PVD carbon and one cycle of hot filament carbon. Except for the first exposure of the PVD C, all curves are fitted with the Arrhenius equation (dashed line).*

*Table 7. Etching behaviors of EUV induced carbon, hot filament carbon and PVD carbon*

| Parameter | EUV induced C | Hot filament C | PVD C |
|---|---|---|---|
| Etch rate (nm/min) | 0.2 (60° C) | 0.02 (60° C) 0.03 (75° C) | 0.06 (75° C) |
| Activation energy (eV) | 0.45±0.03 | 0.26±0.01 | 0.40±0.05 |
| Pre-exponential factor (nm/min) | $5 \times 10^5 - 5 \times 10^6$ | 180±79 | $6 \times 10^3 - 2 \times 10^5$ |
| Thickness dependence | No (11-5 nm) | No (20-17 nm) | yes (< 7 nm) |

### 6.4.3    Thickness dependence

The hydrogen etching of a PVD deposited carbon film is shown in Fig. 39. The sample temperature was kept at a constant temperature of 75° C, except for a short period after the start of the H-exposure, as shown in Fig. 39 (a). Fig. 39 (b) displays the carbon film thickness and the etch rate, calculated from the time derivative of the thickness. Similar to the EUV induced carbon film, initially a large etch rate is observed, tentatively attributed to the removal of storage related carbon contamination. After this initial stage, the etch rate reduces to around 0.05 nm/min at 105 minutes. From that point onwards a slight increase of the etch rate is observed. As discussed in section 6.4.2, according to Samm [19] a $CH_3$ erosion precursor is required for cleaning, and this increase could be associated to the formation of that precursor (PVD-carbon contains no hydrogen). After a certain time, assuming at about 120 minutes, an equilibrium should be reached in the precursor-driven etching and the etch rate should become constant. However, the etch rate decreases again (120 – 150 min.) which indicates that a different phenomenon could influence the etch rate as well, for instance the density of the material.

To illustrate such an effect, Fig. 40 shows a decrease of the etch rates with decreasing thickness of the PVD carbon films at both 68° C and 75° C. The etch rates of sample 1 in Fig. 40 are from Fig. 39 (b), between 125 and 150 minutes. We refer to this part of the process as the thickness dependence range. The etch rates of sample 2 in Fig. 40 is from the same data as used in Fig. 38. The change in etch rate can be attributed to a variation in carbon morphology (e.g. density and bonding structure) with thickness. The presence of this morphology variation has been observed from the *in situ* spectroscopic ellipsometry and quartz microbalance monitoring during the PVD deposition. Both techniques resulted in a very similar thickness development (not shown). The optical constants obtained from ellipsometry during the layer growth are evaluated in Fig. 41 for sample 1. A substantial variation with thickness of especially the extinction coefficient ($k$) is observed. The increase of both refractive index ($n$) and extinction coefficient ($k$) indicates an increase of the density and the amount of $sp^2$ bonds in the carbon film during deposition in the thickness range of 1.1 to 3.6 nm. This would explain the observed decrease of the etch rate during the cleaning process as the layer becomes thinner.

At the end of the cleaning process, as shown in Fig. 39(b) at around 160 minutes, there is a local maximum of the etch rate. This maximum is suggested to be caused by hydrocarbons at the interface between the PVD layer and the natural oxide of the silicon wafer. This interfacial layer would then be related to the atmospheric conditions during storage of the wafer. We did not observe this phenomenon at the end of the cleaning process for the EUV induced carbon layer, probably because the etch rate of EUV induced carbon is considerably higher, masking such effect.

For the EUV induced carbon, the similar etch rates of the last three exposures shown in Fig. 38 indicate that there is no thickness dependence in the thickness ranging

from 11 to 5 nm. Also for the hot filament carbon film we did not observe a thickness dependence for etching in the thickness ranging from 20 to 17 nm.
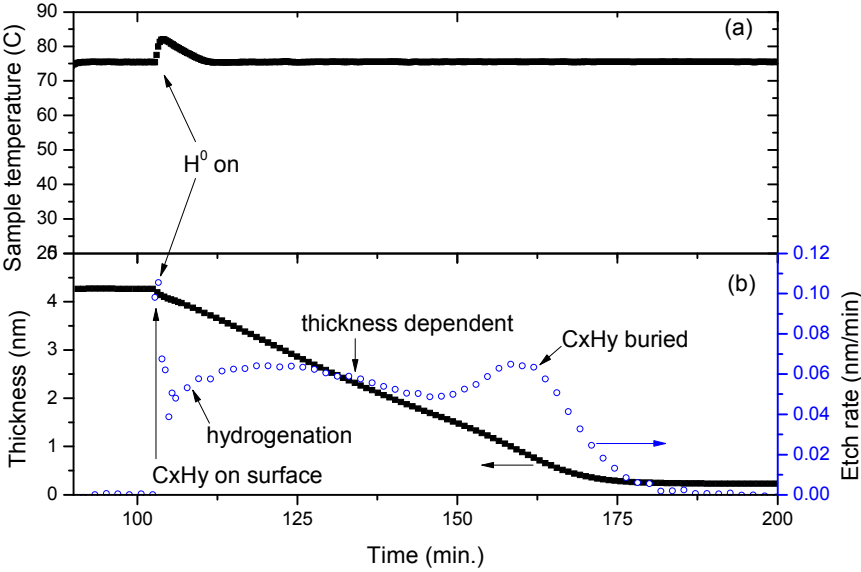


*Fig. 39. H$^0$ cleaning of a 4.3 nm thick PVD carbon film: sample temperature during cleaning (a), thickness and etch rate (b)*
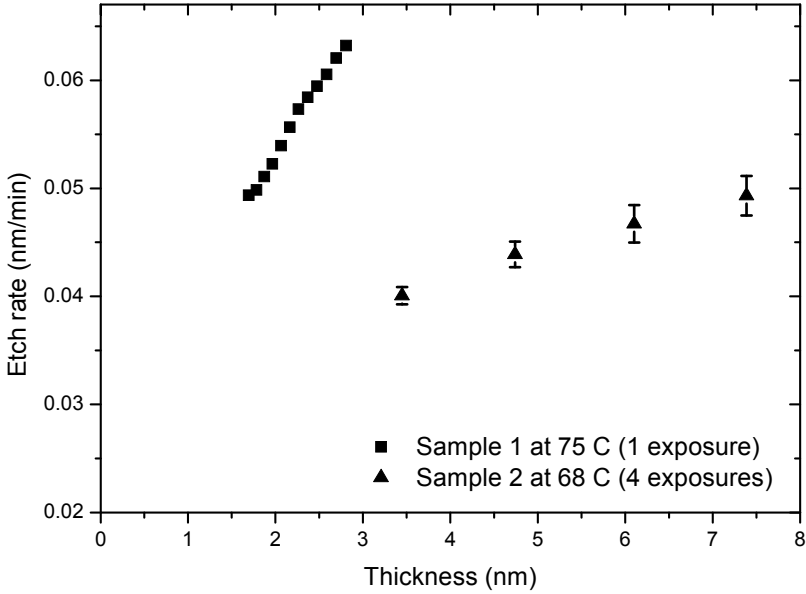
*Fig. 40. Etch rate versus film thickness for PVD carbon sample 1 (at 75° C) and sample 2 (at 68° C)*
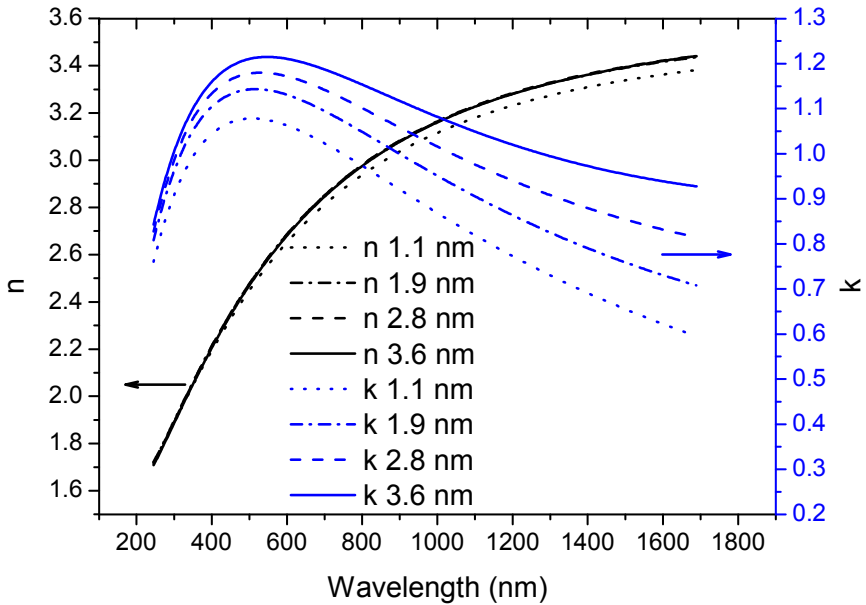


*Fig. 41. Optical constants measured at four increasing thicknesses during the deposition of a thin evaporated carbon film.*

### *6.5    Conclusions*

Atomic hydrogen exposure is confirmed to be an efficient method for removing carbon contamination. We studied the etching of three types of carbon films, namely those deposited by EUV radiation, by hot filament deposition and by PVD deposition. The *in situ* monitoring of the etch process with spectroscopic ellipsometry shows that the etch rates of these carbon types are very different. The high etch rate of the EUV induced carbon, namely 0.2 nm/min at a sample temperature of 60° C, is related to the large hydrogen content of this carbon type. The other, non hydrogenated carbon layers etch much slower because the hydrogenation process still has to precede the actual C-removal.

The etch rate of all three types of carbon is strongly temperature dependent. Analysis of the Arrhenius plot provides an activation energy of 0.45 eV and 0.26 eV, for EUV induced and hot filament carbon, respectively, indicating a significant difference in the chemical and physical process of etching these types of carbon. No film thickness dependence of the etch rate was found for these films. In contrast, the PVD deposited carbon film shows a thickness dependence of the etch rate. This is related to carbon density and bonding structure variation during growth of this film.

This work shows that ellipsometry is a valuable technique to characterize carbon contamination layers, to *in situ* monitor the cleaning process, and to determine the etch rate. Furthermore its suitability to be applied *in situ* provides the possibility for end-point detection of atomic hydrogen cleaning in several practical applications.

### *6.6    Acknowledgements*

### *6.7    References*

[1]  K.-J. Boller, R.-P. Haelbich, H. Hogrefe, W. Jark, and C. Kunz, Investigation of carbon contamination of mirror surfaces exposed to synchrotron radiation, Nuclear Instruments and Methods in Physics Research 208 (1983) 273-279.

[2]  H. Meiling, B. Mertens, F. Stietz, M. Wedowski, R. Klein, R. Kurt, E. Louis, and A. E. Yakshin, Prevention of MoSi multilayer reflection loss in EUVL tools, 2001 (SPIE), 4506, p. 93-104.

[3]  J. Hollenshead and L. Klebanoff, Modeling radiation-induced carbon contamination of extreme ultraviolet optics, Journal of Vacuum Science & Technology B 24 (2006) 64-82.

[4]  S. Matsunari, T. Aoki, K. Murakami, Y. Gomei, S. Terashima, H. Takase, M. Tanabe, Y. Watanabe, Y. Kakutani, M. Niibe, and Y. Fukuda, Carbon deposition on multi-layer mirrors by extreme ultra violet ray irradiation, SPIE, San Jose, CA, USA, 2007 (SPIE), 6517, p. 65172X-8.

[5]  N. Koster, B. Mertens, R. Jansen, A. van de Runstraat, F. Stietz, M. Wedowski, H. Meiling, R. Klein, A. Gottwald, F. Scholze, M. Visser, R. Kurt, P. Zalm, E. Louis, and A. Yakshin, Molecular contamination mitigation in EUVL by environmental control, Microelectronic Engineering 61-2 (2002) 65-76.

[6]  K. Motai, H. Oizumi, S. Miyagaki, I. Nishiyama, A. Izumi, T. Ueno, and A. Namiki, Cleaning technology for EUV multilayer mirror using atomic hydrogen generated with hot wire, Thin Solid Films 516 (2008) 839-843.

[7]  H. Oizumi, A. Izumi, K. Motai, I. Nishiyama, and A. Namiki, Atomic hydrogen cleaning of surface ru oxide formed by extreme ultraviolet irradiation of Ru-capped multilayer mirrors in H2O ambience, Japanese Journal of Applied Physics Part 2-Letters & Express Letters 46 (2007) L633-L635.

[8]  J. Samuel Graham, A. S. Charles, W. M. Clift, E. K. Leonard, and B. Sasa, Atomic hydrogen cleaning of EUV multilayer optics, 2003 (SPIE), 5037, p. 460-469.

[9]  T. Tsarfati, E. Zoethout, R. W. E. van de Kruijs, and F. Bijkerk, Atomic O and H exposure of C-covered and oxidized d-metal surfaces, Surface Science 603 (2009) 2594-2599.

[10] J. Q. Chen, E. Louis, J. Verhoeven, R. Harmsen, C. J. Lee, M. Lubomska, M. van Kampen, W. van Schaik, and F. Bijkerk, Secondary electron yield measurements of carbon covered multilayer optics, Applied Surface Science 257 (2010) 354-361.

[11] H. Oizumi, H. Yamanashi, I. Nishiyama, K. Hashimoto, S. Ohsono, A. Masuda, A. Izumi, and H. Matsumura, Contamination removal from EUV multilayer using atomic hydrogen generated by heated catalyzer, 2005 (SPIE), 5751, p. 1147-1154.

[12] I. Nishiyama, H. Oizumi, K. Motai, A. Izumi, T. Ueno, H. Akiyama, and A. Namiki, Reduction of oxide layer on Ru surface by atomic-hydrogen treatment, 2005 (AVS), 23, p. 3129-3131.

[13] D. J. W. Klunder, M. M. J. W. v. Herpen, V. Y. Banine, and K. Gielissen, Debris mitigation and cleaning strategies for Sn-based sources for EUV lithography, 2005 (SPIE), 5751, p. 943-951.

[14] B. Mertens, B. Wolschrijn, R. Jansen, N. Koster, M. Weiss, M. Wedowski, R. Klein, T. Bock, and R. Thornagel, EUV time-resolved studies on carbon growth and cleaning, 2003 (SPIE), 5037, p. 95-102.

[15] M. Malinowski, P. Grunow, C. Steinhaus, W. M. Clift, and L. Klebanoff, Use of molecular oxygen to reduce EUV-induced carbon contamination of optics, 2001 (SPIE), 4343, p. 347-356.

[16] S. Oestreich, R. Klein, F. Scholze, J. Jonkers, E. Louis, A. E. Yakshin, P. C. Goerts, G. Ulm, M. Haidl, and F. Bijkerk, Multilayer reflectance during exposure to EUV radiation, 2000 (SPIE), 4146, p. 64-71.

[17] G. Samuel, S. Charles, C. Miles, and K. Leonard, Radio-frequency discharge cleaning of silicon-capped Mo/Si multilayer extreme ultraviolet optics, Journal of Vacuum Science & Technology B: Microelectronics and Nanometer Structures 20 (2002) 2393-2400.

[18] T. Tsarfati, E. Zoethout, R. van de Kruijs, and F. Bijkerk, Growth and sacrificial oxidation of transition metal nanolayers, Surface Science 603 (2009) 1041-1045.

[19] U. Samm, Physical processes of the interaction of fusion plasmas with solids, Plasma Physics and Controlled Fusion 38 (1996)

[20] E. Vietzke, V. Philipps, K. Flaskamp, P. Koidl, and C. Wild, The Reaction of Atomic-Hydrogen with a-C-H and Diamond Films, Surface & Coatings Technology 47 (1991) 156-161.

[21] J. Q. Chen, E. Louis, C. J. Lee, H. Wormeester, R. Kunze, H. Schmidt, D. Schneider, R. Moors, W. van Schaik, M. Lubomska, and F. Bijkerk, Detection and characterization of carbon contamination on EUV multilayer mirrors, Optics Express 17 (2009) 16969-16979.

[22] J. Chen, E. Louis, H. Wormeester, R. Harmsen, R. van de Kruijs, C. J. Lee, W. van Schaik, and F. Bijkerk, Carbon induced EUV reflectance loss characterized using visible-light ellipsometry, Measurement Science and Technology submitted

[23] J. W. Weber, T. A. R. Hansen, M. C. M. v. d. Sanden, and R. Engeln, B-spline parametrization of the dielectric function applied to spectroscopic ellipsometry on amorphous carbon, Journal of Applied Physics 106 (2009) 123503.

[24] *Handbook of ellipsometry*; *Vol.*, edited by H. G. Tompkins and E. A. Irene (William Andrew Publishing/Noyes, 2005).

[25] J. W. Weber, Thesis, Eindhoven University of Technology, 2009.

[26] J. Diaz, G. Paolicelli, S. Ferrer, and F. Comin, Separation of the sp(3) and sp(2) components in the C1s photoemission spectra of amorphous carbon films, Physical Review B 54 (1996) 8064-8069.

[27] N. Paik, Raman and XPS studies of DLC films prepared by a magnetron sputter-type negative ion source, Surface and Coatings Technology 200 (2005) 2170-2174.

[28] P. Merel, M. Tabbal, M. Chaker, S. Moisa, and J. Margot, Direct evaluation of the sp(3) content in diamond-like-carbon films by XPS, Applied Surface Science 136 (1998) 105-110.

[29] D. L. Windt, IMD - Software for modeling the optical properties of multilayer films, Computers in Physics 12 (1998) 360-370.

[30] J. Q. Chen, C. J. Lee, E. Louis, F. Bijkerk, R. Kunze, H. Schmidt, D. Schneider, and R. Moors, Characterization of EUV induced carbon films using laser-generated surface acoustic waves, Diamond and Related Materials 18 (2009) 768-771.

[31] R. W. Collins, Insitu Ellipsometry as a Diagnostic of Thin-Film Growth - Studies of Amorphous-Carbon, Journal of Vacuum Science & Technology a-Vacuum Surfaces and Films 7 (1989) 1378-1385.

[32] T. Tsarfati, E. Zoethout, R. van de Kruijs, and F. Bijkerk, In-depth agglomeration of d-metals at Si-on-Mo interfaces, Journal of Applied Physics 105 (2009) 5.

[33] I. Nishiyama, Update on SFET Optics Contamination Learning (http://ieuvi.org/TWG/ConOptics/IEUVI_ContamOptics01.htm), IEUVI, Optics Contamination and Lifetime TWG Meetings, San Joes, USA, 2009.

## 7 Valorization and outlook

Extreme ultraviolet lithography (EUVL) is a next generation photolithography technique that uses 13.5 nm radiation [1]. A critical issue of EUV optics is radiation induced surface contamination because it can reduce the throughput of the EUVL equipment [2,3]. Although remedies are being developed, including options for *in situ* cleaning procedures of the optics [4,5], information on the degree of contamination and the composition of the contaminant is mandatory.

The research described in this thesis was conducted by support of the Materials innovation institute (M2i) and our industrial partner ASML. M2i is a public-private partnership between the Dutch government, industry and academia [6]. Each of them contributes about one-third to the M2i program aiming at the development of new materials for sustainable economic growth. ASML is the world's leading provider of lithography systems for the semiconductor industry [7] and is at the forefront of the development of EUVL. The first EUVL machines have been shipped to customers and equipments for high volume manufacturing are planned for 2012 [7].

We aimed at the development of the physics and methodology of monitoring surface contamination of EUV optics during the lithography process. The goal was to be able to determine contaminants at concentration levels to be expected in EUV lithographic machines operating at high-volume production. Such detection levels were still beyond the state-of-the-art and the particular physics of the contamination formation was only partly understood.

An in-depth study on the various candidate techniques for contamination monitoring has been carried out and the main results are presented in this thesis. We built a functional experimental model with the desired sensitivity and analysis power, suitable to detect surface oxidation and carbon layers of typically a fraction of a nanometer, under the boundary condition of potential applicability in EUVL exposure machines. In the following sections we will discuss some prospective valorizations based on the research results achieved in this thesis.

### 7.1 *Contamination monitoring*

In the EUVL equipment, the need for having an *in situ* monitoring method is evident, taken into consideration the required production throughput in relation to the down time of the instrumentation required for cleaning.

As described in chapter 3 and chapter 6, spectroscopic ellipsometry (SE) is a non-contact, non-destructive technique. It was proven that SE is very sensitive for measuring carbon layers, even in the presence of the highly heterogeneous structure of the multilayer. The detection limit of SE is better than 0.1 nm which is sufficient for EUV optics contamination monitoring [8]. In addition, all the components of SE can remain outside the vacuum, meaning that only line-of-sight optical access is required.

Different types of carbon contamination under photon irradiation, i.e. graphite or polymer like, have been observed. As described in chapter 5 spectroscopic ellipsometry can be used to determine the type of carbon contamination based on the carbon film's extinction coefficient or the trajectory of the two ellipsometric angles. Determining the type of carbon contamination is important for prediction of the resultant reflectance loss as well as for the contamination cleaning. Furthermore, spectroscopic ellipsometry can be used to discriminate carbon growth from surface oxidation. This is not described in detail since it is industrially confidential at the moment.

*Ex situ* spectroscopic ellipsometry is being used by our industrial partner ASML for investigating optics contamination including EUV or e-beam carbon growth and oxidization of EUV optics. The knowledge gained within this thesis work on how to analyze the ellipsometric data has been valorized to the benefit of ASML.

### 7.2    Predicting EUV reflectance loss

The effect of carbon contamination on the reflectance of each optic in EUVL equipment is one of the most important parameters that influence the throughput of such a system. *In situ* cleaning is suggested to maintain or recover the reflectance of the multilayer optic. The carbon layer thickness and/or the reflectance loss of each optic can be used as a trigger signal required to start and stop the cleaning process. In chapter 5 of this thesis we describe a methodology to predict the EUV reflectance loss due to carbon deposition based on visible-light ellipsometry measurements. This enables real time determination of the EUV reflectance of optics and is therefore a key component of the cleaning strategy.

Furthermore, the method described in chapter 5 can also be applied for contamination monitoring on synchrotron beam line optics.

### 7.3    Carbon contamination cleaning

As introduced in chapter 6, in literature several methods have been suggested and tested to remove carbon contamination and oxidation on EUV optics. We investigated atomic hydrogen cleaning of several types of carbon such as EUV induced carbon which is polymer like and evaporated carbon which is graphite like.

We found that the etch rate during atomic hydrogen exposure depends on temperature, type of carbon and on layer thickness. Furthermore, the temperature dependence is type of carbon dependent. EUV induced carbon has the highest etching rate and the highest temperature dependence.

All these findings can be used to optimize the type and extent of the cleaning process in EUVL equipments. For example, cleaning time and/or intensity should be customized for different optics if their carbon contaminations have different properties

(i.e. more polymer like or graphite like). The temperature of the optic should also be taken into account since the cleaning rate is temperature dependent.


### *7.4     Outlook*

Based on the results presented in this thesis we suggest the use of spectroscopic ellipsometry for *in situ* monitoring of optics contamination in EUVL machines. However, line-of-sight access to the optical surface, which is required for a general ellipsometry configuration, can be difficult and for some optics even impossible. In those cases, we suggest to focus the research on fiber-networked ellipsometry using polarization preserving fiber optics. A pilot study on the applicability of such systems has been carried out at Twente University where the concept has been verified experimentally for carbon deposited EUV optics [9]. Further investigations, especially on data analysis and the use of multiple wavelengths, are suggested to be carried out.

Optics contamination can be non-uniformly distributed across the optical surface since the contamination rate depends on the local illumination conditions (e.g. intensity and presence of adsorbates). General ellipsometry traditionally measures at a fixed spot on a sample and mapping is usually achieved by translating the sample stage. However, translating the optic in an accurately aligned optical system is not possible. In order to monitor the distribution of the optics contamination, imaging ellipsometry is suggested to be investigated for *in situ* mapping [10,11]. Another way to achieve mapping of the distribution could be to install an array of fibers looking at different positions of an optical element and use multiplexing techniques to probe them sequentially thus providing localized information on the state of contamination.

Spectroscopic ellipsometry enables tracking of monolayer growth and discrimination between carbon growth and surface oxidation. Considering these capabilities, we suggest using spectroscopic ellipsometry to further study the contamination mechanisms under EUV illumination. Application of ellipsometry on the EUV test chamber in the FOM laboratory at ASML Research is planned within the CP3E project [12].

Finally, in chapter 4 we demonstrated monitoring of the growth and removal of carbon contamination on EUV multilayers by measuring the secondary electron yield (SEY) as a function of primary electron energy. Different material and/or surface conditions have different secondary electron yield characteristics. We suggest doing experimental investigations on revealing the major components of a contamination layer by analysis of the variation of the SEY spectra.

## *7.5    References*

[1]    *EUV Lithography*; *Vol. PM178*, edited by V. Bakshi (SPIE, 2008).

[2]    J. Hollenshead and L. Klebanoff, Modeling radiation-induced carbon contamination of extreme ultraviolet optics, Journal of Vacuum Science & Technology B 24 (2006) 64-82.

[3]    N. Koster, B. Mertens, R. Jansen, A. van de Runstraat, F. Stietz, M. Wedowski, H. Meiling, R. Klein, A. Gottwald, F. Scholze, M. Visser, R. Kurt, P. Zalm, E. Louis, and A. Yakshin, Molecular contamination mitigation in EUVL by environmental control, Microelectronic Engineering 61-2 (2002) 65-76.

[4]    K. Motai, H. Oizumi, S. Miyagaki, I. Nishiyama, A. Izumi, T. Ueno, and A. Namiki, Cleaning technology for EUV multilayer mirror using atomic hydrogen generated with hot wire, Thin Solid Films 516 (2008) 839-843.

[5]    S. Graham, C. Steinhaus, M. Clift, L. Klebanoff, and S. Bajt, Atomic hydrogen cleaning of EUV multilayer optics, 2003 (SPIE), 5037, p. 460-469.

[6]    http://www.m2i.nl/

[7]    http://www.asml.com

[8]    http://www.sematech.org/meetings/archives/litho/7741/index.htm

[9]    F. Liu, C. J. Lee, J. Chen, E. Louis, and F. Bijkerk, Fiber-based ellipsometry for in situ monitoring (submitted for a presentation at the Conference on Lasers and Electro-Optics), 2011.

[10]   U. Wurstbauer, C. Roling, U. Wurstbauer, W. Wegscheider, M. Vaupel, P. H. Thiesen, and D. Weiss, Imaging ellipsometry of graphene, Applied Physics Letters 97 (2010) 231901.

[11]   R. Garg, N. Faradzhev, S. Hill, L. Richter, P. S. Shaw, R. Vest, and T. B. Lucatorto, A simple null-field ellipsometric imaging system (NEIS) for in-situ monitoring of EUV-induced deposition on EUV optics, 2010 (SPIE), 7636, p. 76361Z.

[12]   http://www.rijnhuizen.nl/en/node/2601.

## Summary

Extreme ultraviolet lithography (EUVL) is a next generation photolithographic technique that uses 13.5 nm or Extreme UV radiation and multilayer coated reflective optics. The reflectance of these optical elements can be strongly reduced when, as a consequence of exposing the optics to EUV photons, a contamination layer is built up on the mirrors. Since this will reduce the throughput of EUV lithography machines, contamination monitoring is considered to be necessary. Direct observation of the EUV reflectance of the mirrors is hardly possible since the required accuracy can only be achieved in very sophisticated lab reflectometers.

This thesis describes experimental research on the topic of EUV induced contamination and its monitoring using alternative, *in situ* techniques. Occasional techniques for such a task have been mentioned, but no real investigations were carried out. This thesis reviews the suggested and new techniques and describes experimental work on the three most promising: laser-generated surface acoustic waves (LG-SAWs), secondary electron yield (SEY), and spectroscopic ellipsometry (SE). The goal was not only to develop an appropriate monitoring method, but also to get insight in the material properties, both mechanical and optical, of the contamination layer in order to predict the EUV reflectance loss and the possibilities to clean the optics.

Firstly, we investigated the mechanical properties of the EUV induced carbon contamination by LG-SAW. They were inferred from Young's modulus (<100 GPa) that showed that the carbon layer, when induced by EUV illumination in EUVL machine vacuum conditions, is mechanically soft and polymeric in nature with a high percentage of hydrogen. Furthermore, LG-SAW is shown to be very sensitive for measuring carbon layers, even in the presence of the highly heterogeneous structure of the multilayer. LG-SAW was found to have an estimated detection limit of 1.2 nm of carbon.

Secondary electron emission is a phenomenon in which low-energy, secondary electrons escape from a solid surface under bombardment with high-energy primary electrons. We determined the secondary electron yield as a function of primary electron energy during the build-up as well as during the removal of the carbon contamination on EUV multilayers. The maximum yield, and the corresponding primary electron energy, reduced when the surface was covered by a carbon layer, making the technique generally appropriate for optics contamination monitoring. The limit of detection was estimated to be below 0.1 nm.

Spectroscopic ellipsometry, based on the material dependent change of the polarization of light when reflected from a surface, was used to determine the carbon layer thickness and the optical constants ranging from ultraviolet to near infrared. SE was shown to be able to resolve the presence of a hydrogenated, polymeric like carbon layer on the optics. Since SE has a detection limit of 0.1 nm and since it is a non-contact technique with minimal space needed in the vacuum chamber, it is considered as the best candidate for contamination monitoring in this application. Furthermore, by

modeling the optical constants using Bruggeman's effective medium approximation (BEMA) and the Clausius-Mosotti (CM) equation, we were able to accurately estimate the EUV reflectance loss as a function of the thickness of the contamination layer. This is the second reason for us to classify SE as the most appropriate technique.

Atomic hydrogen cleaning is considered as one of the most efficient methods for cleaning carbon contamination in the EUV lithography environment, and we have explored this cleaning process by monitoring it with *in situ* ellipsometry. The etch rate of atomic hydrogen cleaning for three different kinds of carbon films was investigated. We found that the etch rate depends on the carbon type (polymer- or graphite-like), layer thickness and temperature. The polymer-like EUV induced carbon shows the highest etch rate, while the more graphite-like carbon layers showed an etch rate that was an order of magnitude smaller. This suggests to further study the nature of the EUV induced contamination process in order to fully control the contamination and its cleaning process.

## Samenvatting

Extreem ultraviolette lithografie (EUVL) is een fotolithografische techniek die gebruikmaakt van licht met een golflengte van 13,5 nm, ook bekend als extreem ultraviolet licht (EUV). Het is de techniek die gebruikt gaat worden in de volgende generatie lithografiemachines om patronen af te beelden, een essentiële stap in de productie van computerchips. Vanwege de hoge absorptie van EUV licht wordt gebruik gemaakt van reflecterende optische componenten, elk voorzien van een multilaag als hoge-reflectiecoating.

De reflectie van deze optische elementen wordt sterk verminderd wanneer, als gevolg van blootstelling van de optiek aan EUV fotonen, een vervuilende laag, meestal bestaand uit koolstof, wordt opgebouwd op de spiegels. Omdat dit de transmissie van EUV-lithografische systemen zal verminderen, is het noodzakelijk de mate van vervuiling voortdurend te bepalen. Een directe reflectiemeting van de spiegels is eigenlijk niet mogelijk omdat de vereiste nauwkeurigheid alleen kan worden bereikt in zeer geavanceerde reflectometers in specialistische laboratoria.

Dit proefschrift beschrijft experimenteel onderzoek naar EUV-geïnduceerde verontreiniging van spiegeloppervlakken en het monitoren daarvan met behulp van verscheidene *in-situ* technieken. Bij diverse gelegenheden zijn hiervoor monitortechnieken voorgesteld maar nooit echt goed onderzocht. Dit proefschrift bespreekt zowel de voorgestelde als nieuwe technieken en beschrijft experimenteel werk aan de drie meest veelbelovende, te weten: akoestische oppervlaktegolven die met een laserpuls worden opgewekt (laser-generated surface acoustic waves, kortweg LG-SAW), emissie van secundaire elektronen (Secondary Electron Yield, SEY) en spectroscopische ellipsometrie (SE). Het doel was niet alleen een geschikte meetmethode te ontwikkelen, maar ook inzicht te krijgen in zowel de mechanische als optische materiaaleigenschappen van de vervuiling om zo het EUV reflectieverlies en de mogelijkheden om de optiek weer schoon te maken te kunnen voorspellen.

We zijn begonnen met onderzoek te doen naar de mechanische eigenschappen van de EUV-geïnduceerde koolstofvervuiling met behulp van LG-SAW. Deze eigenschappen konden worden afgeleid aan de hand van de Young's modulus (<100 GPa). Hieruit bleek dat de koolstoflaag, wanneer die is ontstaan als gevolg van blootstelling van de spiegels aan EUV licht in een voor EUVL machines kenmerkend vacuüm, mechanisch zacht en polymeer is, met een hoog waterstof gehalte. Bovendien blijkt LG-SAW een zeer gevoelige techniek te zijn voor het meten van koolstoflagen, zelfs wanneer deze zich op de zeer heterogene multilaagstructuur bevinden. Er werd een detectielimiet waargenomen van 1,2 nm voor het meten van een koolstoflaag.

Secundaire elektronenemissie is een verschijnsel waarbij laagenergetische secundaire elektronen ontsnappen uit een vaste stof onder bombardement met hoog-energetische primaire elektronen. We bepaalden de opbrengst van secundaire elektronen als functie van de primaire elektronenenergie zowel tijdens de aangroei als tijdens het

verwijderen van de koolstofvervuiling op EUV multilagen. De maximale opbrengst en de bijbehorende primaire elektronenenergie verminderen wanneer het oppervlak wordt bedekt met een laag koolstof, waardoor de techniek algemeen geschikt is voor het monitoren van vervuiling van optische componenten in een vacuüm. De detectiegrens is minder dan 0,1 nm.

Spectroscopische ellipsometrie is gebaseerd op de materiaalafhankelijke verandering van de polarisatie van licht wanneer het reflecteert aan een oppervlak. We hebben de techniek gebruikt om de koolstoflaagdikte en de optische constanten, variërend van ultraviolet tot het nabije infrarode deel van het spectrum, te bepalen. De techniek bleek in staat om de aanwezigheid van waterstofrijk polymeerachtig koolstof op de optiek aan te tonen en heeft een detectielimiet van 0,1 nm. Omdat het een non-contacttechniek is die slechts een minimale ruimte nodig heeft in de vacuümkamer, wordt deze beschouwd als de beste kandidaat voor het monitoren van verontreiniging van spiegels. Bovendien, door het modelleren van de optische constanten met behulp van de door Bruggeman ontwikkelde 'effective medium approximation' (BEMA) en de Clausius-Mosotti (CM) vergelijking, waren we in staat om het EUV reflectieverlies nauwkeurig in te schatten als functie van de dikte van de vervuilingslaag. Dit is voor ons de tweede reden om spectroscopische ellipsometrie aan te merken als de meest geschikte techniek.

Het verwijderen van koolstofvervuiling m.b.v. atomair waterstof wordt beschouwd als een van de meest efficiënte methodes voor het reinigen van optische elementen in EUV lithografiesystemen en we hebben dit proces onderzocht met behulp van *in situ* ellipsometry. Op deze manier hebben we de etssnelheid van atomair waterstofreiniging bepaald voor drie verschillende soorten koolstof films en vonden dat de snelheid afhangt van het koolstoftype (polymeer of grafietachtig), de laagdikte en de temperatuur. Het polymeerachtige EUV-geïnduceerde koolstof etst het snelst, terwijl de etssnelheid van de meer grafietachtige koolstoflaagjes een grootteorde lager was. Dit suggereert de noodzaak tot verdere studie naar de aard van het EUV-geïnduceerde verontreinigingproces om tot een volledige controle van zowel de verontreiniging, als van het weer verwijderen ervan te komen.

## Acknowledgements

The last four and a half years have been very memorable for me, but they have not always been easy. Therefore, at the end of this thesis I want to thank many people inside and outside of FOM-Rijnhuizen for their invaluable help. Without them I do not think I could have finished this thesis.

First of all, I would like to thank my promoter Fred Bijkerk who gave me the opportunity to start my PhD research in the nanolayer Surface and Interface (nSI) department. He corrected all my papers and gave valuable comments. He always supported me for doing experiments and writing papers. I would also like to thank my daily supervisor Eric Louis, leader of the Advanced Applications of XUV Optics group (AXO), for all the discussions about how to interpret my experimental results, how to write it down and how to make well structured presentations. Also, he gave me great support when I had problems related to my family's stay in the Netherlands.

I would like to thank all my colleagues in the nSI department. I have received such useful comments from them on my papers during group meetings. Discussions with Robbert, Erwin, Rob, Malcom, Alexey, Michael, Tim, Jeroen and Aart were always very helpful, and so was the technical support from our technicians. In particular, I want to acknowledge Rob, Kees and Arend-Jan for their skilful help for my experiments. For the XPS experiments and analysis I would like to thank Erwin for his guidance.

I would also like to thank my co-authors for their contribution. I gratefully acknowledge Herbert Wormeester at the University of Twente for the ellipsometry experiments (chapter 3). This was also of great value for my experiments later at Rijnhuizen. In addition, he helped me in the modeling of optical constants in our paper on EUV reflectance loss (chapter 5) and atomic hydrogen cleaning (chapter 6). I would like to thank Chris Lee for his valuable comments on almost all the chapters in this thesis. He also showed me how to improve the data analysis. Both of them helped me enormously. Their help was not limited to the papers they are co-authoring. I would also like to thank Jan Verhoeven at Leiden University for his tremendous contributions for the secondary electron yield paper (chapter 4). I want to thank Reinhard Kunze and Hagen Schmidt at the Leibniz Institute for Solid State and Materials Research and Dieter Schneider at the Fraunhofer-Institutes for Material and Beam Technology, for their help in the experiments and analysis of the laser-generated surface acoustic waves.

Our industrial partner ASML has been always supportive, not only by clearing our papers for publication, but also by making the experiments in their EUV lab possible. I would like to thank Willem van Schaik, Maarten van Kampen, Monika Lubomska, Roel Moors, Mandeep Singh, Luc Stevens, and Max Siem at ASML for their support during my research. I would like to thank Feng Liu and Chris Lee for carrying out the experiments of fiber-based ellipsometry. This work can greatly improve the industrial applicability of ellipsometry.

*Jueguan Chen*

**Curriculum Vitae**

Juequan Chen (陈珏铨) was born on October 17, 1979 in Zhejiang Province, China. In 2002, he received a Bachelor of physics from Sichuan Normal University. In 2005, he obtained a Master of physics from the Institute of Plasma Physics, Chinese Academy of Sciences. The research was about neutron diagnostics and neutron behavior studies on HT-7 superconducting Tokamak. In December of 2006, he moved to the Netherlands and started his PhD research at the FOM-Institute for Plasma Physics Rijnhuizen in Nieuwegein under supervision of prof. dr. F. Bijkerk and E. Louis. The topic was on characterization of EUV optics contamination. The research has been presented in several scientific papers and in this thesis.